A HIGH RESOLUTION MULTINUCLEAR MAGNETIC RESONANCE STUDY OF CERAMIC PHASES

Mark Edmund Smith

A thesis submitted to the University of Warwick for admission to the degree of Doctor of Philosophy.

Department of Physics

October 1987

This thesis is dedicated to my family

for being there.

List of Contents

List of Tables

List of Figures

Acknowledgements

I would like to thank the SERC for providing the financial assistance, and the Department of Physics for providing the facilities that made this work possible. A number of samples were kindly given to me, namely $Y_3Al_5O_{12}$ (Johnson-Matthey Chemicals), a single crystal of $YAlO_3$ (Dr. S. Abell, University of Birmingham), α',β'-and β''-sialons and the non-stoichiometric spinels (Professor M.H. Lewis), and $Y_2Si_2O_7$ and Y_2SiAlO_5N (Dr. G. Long-Ward). I also thank Professor M.H. Lewis for allowing me to use the high temperature sintering facilities of his Ceramics group.

The NMR Coffee Club provided an enjoyable distraction at 11.00a.m. each day for which I would like to thank all its members. I am extremely grateful to ATR, KJB, AJL, IEF and MGM whose friendship has supported me over the last 3 years.

Many people aided this study but I would like to express my gratitude to a few people in particular, without whom this work would have been much more difficult. The good overall technical support is acknowledged, but the contribution of Barrie Sheffield and Keith Briggs was particularly invaluable, as was the assistance of Hayley Gilder who diligently typed this thesis. Professor M.H. Lewis and Dr. G. Long-Ward could always spare time to listen and guide me through the mysterious (to me) and complex subject of high temperature ceramics. Dr. Ian Farnan was always happy to discuss topics in NMR and made many useful suggestions. By far my greatest debt is to my supervisor Dr. Ray Dupree whose excellent guidance, interest and inspiration made this study such a rewarding experience.

Declaration

The work for this thesis was carried out in the Department of Physics of the University of Warwick from October 1984 to September 1987. It is the result of my own independent research except where specifically referenced in the text and has not previously been submitted for any other degree.

Some parts of this thesis have been published or accepted for publication as follows:

(1) "A Study of the Vacancy Distribution in Non-Stoichiometric Spinels by Magic-Angle Spinning NMR"
R. Dupree, M.H. Lewis and M.E. Smith (Phil. Mag. A. 53, 1986, L(17-20)].

(2) "Signal-to-Noise Optimisation of Pulsed NMR on Samples with Long Spin-Lattice Relaxation Times."
R. Dupree and M.E. Smith (J. Magn. Reson. To be published 1987).

(3] "High Resolution Silicon-29 NMR in the Y-Si-O-N System."
R. Dupree, M.H. Lewis and M.E. Smith (J. Am. Chem. Soc. To be published).

(4] "Structural Characterisation of Ceramic Phases with High Resolution Aluminium-27 NMR" R. Dupree, M.H. Lewis and M.E. Smith (J.App. Cryst. To be published].

It is anticipated that other parts of this thesis will be submitted for publication in the future.

Mark E. Smith.

Mark E. Smith.

Abstract

The applicability of magic angle spinning (MAS) NMR to the study of crystalline ceramic phases is investigated. Aluminium-27 and silicon-29 chemical shifts from the crystalline phases of the (Sc,Y,La)-Si-Al-O-N systems are reported. The chemical shift information differentiates between distinct local environments so that the structures of phases containing elements of similar scattering factor can be refined. The utility of MAS-NMR in phase characterisation of complex mixtures is demonstrated by comparing MAS NMR results with X-ray diffraction of different phase preparations. This shows that a much more complete description of the phase distribution is obtained by using a combination of these techniques. The results of preliminary investigations of the usefulness of other less commonly studied nuclei (^{14}N, ^{25}Mg, ^{45}Sc and ^{139}La) for multinuclear NMR studies of ceramics are given.

The $Si(O,N)_4$ tetrahedra in oxynitride ceramics allow ^{29}Si chemical shifts to be given for the complete range of SiO_xN_{4-x} ($0 \leq x \leq 4$) units. The expected paramagnetic shift with increasing nitrogen content is observed and, although there is extensive overlap of the shift ranges from different units, MAS-NMR spectra allow different atomic arrangements to be distinguished (e.g. in $Y_4Si_2O_7N_2$ and $Y_2Si_3O_3N_4$). The problems associated with long spin-lattice relaxation times ($\sim$ a few hours), encountered for ^{29}Si in some of these materials are discussed, together with a calculation of signal-to-noise optimisation. A more efficient spectral accumulation procedure for such samples is suggested.

The ^{27}Al chemical shift ranges for different structural units (e.g. AlN_4, AlO_4, AlO_6) in ceramics are investigated which allows the aluminium distribution in these materials to be refined. This is shown in the case of some non-stoichiometric spinels ($MgO.xAl_2O_3$) and β'-sialon. In NMR spectroscopy of quadrupolar nuclei ($I \geq 1$), and in particular ^{27}Al ($I=5/2$), extensive broadening of the NMR signal occurs at some sites due to the quadrupolar interaction. Its effect on the quantitative nature of ^{27}Al NMR spectroscopy is discussed.

CHAPTER 1 INTRODUCTION

1.1 High Resolution NMR in the Solid-State

Nuclear magnetic resonance (NMR) is the spectroscopy of the nuclear Zeeman energy levels in a magnetic field and was first observed in bulk matter by Purcell et al[1] and Bloch et al[2] in 1945. NMR is a low energy (low frequency) spectroscopy ($^{\sim}0.1 Jmol^{-1}$) resulting in a very low probability for spontaneous emission. The nuclear spins occupy the Zeeman energy levels according to a Boltzmann distribution with the nuclear spins in thermal equilibrium with the lattice (i.e. the surroundings), producing a small population difference between the levels ($^{\sim}1$ in 10^{+5} for silicon-29 in a magnetic field of 8.45T), so that nuclear paramagnetism is weak and sensitivity low. Despite this NMR has become an important spectroscopic technique having a number of different aspects (e.g. high resolution, relaxation), with high resolution studies emphasised here.

One of the most important discoveries, soon after the NMR phenomenon itself, was that the NMR frequency of a given nuclide in different environments varies slightly. This was first measured in metals in 1949[3], where the effect is larger, with the observation of this effect in other materials following in 1950[4,5]. In 1951 a study of some alcohols measured the different proton resonance frequencies of the different functional groups within the same molecule[6]. The observation of this frequency difference in non-metals (termed the chemical shift) was initially limited to the liquid-state, where rapid isotropic tumbling of the molecules averages the anisotropic interactions present to give narrow NMR spectral lines producing sufficient resolution of different environments. NMR became an important identification technique in the solution-state, particularly for organic chemists as it could distinguish different

local structural units of protons and carbon-13 in molecules.

Extension to the solid-state was slow since the relatively static nature of the structure results in the anisotropic interactions (e.g. dipolar, chemical shift anisotropy and quadrupolar (Sec. 2.1)) broadening the NMR spectral lines, masking the small differences in the isotropic chemical shift. It was suggested that this broadening could be reduced by physically imposing motion on the solid and this was demonstrated in 1958[7]. Figure 1.1 shows the time-domain signal (Sec. 3.1) from sodium-23 in NaCl in solution (c) and solid, both static (a) and spinning (b) with the narrowing produced by spinning immediately obvious from the extension of the time-domain signal. This rotation technique appears to have been regarded as a curiosity for about 15 years since in many of the organic materials of interest the linewidths encountered could not be effectively narrowed by simply spinning the sample. High resolution solid-state NMR of carbon-13 was given new impetus by the combination in a single experiment of three existing techniques, cross-polarisation[8], decoupling[9] and magic angle spinning[10] by Schaefer and Stejskal[11]. The reduction in linewidth by this technique (which can be two orders of magnitude in some crystalline materials) produces high resolution solid-state spectra with different environments being distinguishable within the spectral dispersion and residual linewidths.

Performing experiments in the solid-state has obvious attractions as many molecules change structure in the transformation from solid to solution and many simply do not dissolve. As high resolution solid-state NMR became more widespread the range of nuclei studied expanded from ^{1}H and ^{13}C to others, including sodium-23, aluminium-27 and silicon-29. There are many materials containing these nuclei where other structure-determination techniques (e.g. diffraction) can only provide limited information. This is typified

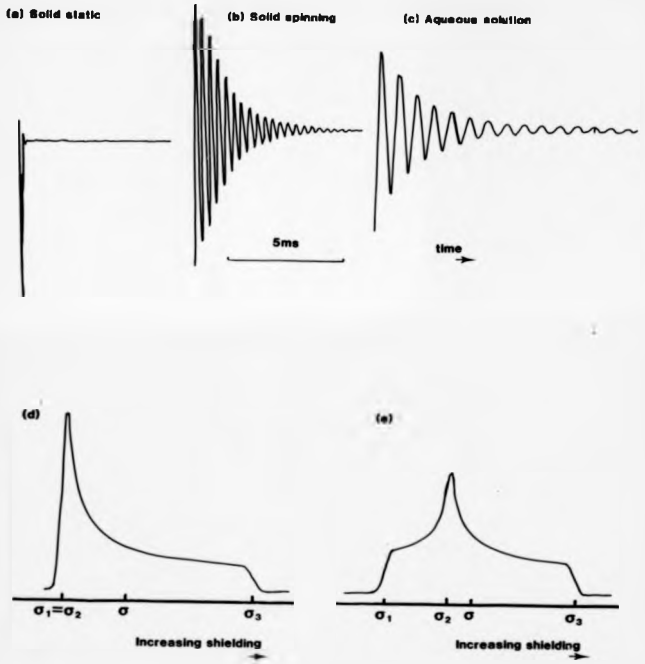

Figure 1.1 ^{23}Na(95.3MHz) time-domain signal for NaCl from (a) solid static,(b) solid spinning and (c) aqueous solution on the same timescale.The frequency difference between (b) and (c) is due to the chemical shift solid – solution.Static powder patterns for chemical shift anisotropy with (d) axial symmetry and (e) no symmetry restriction.

by zeolites where Si/Al ordering is difficult to detect by diffraction due to silicon and aluminium having similar scattering factors, yet NMR readily distinguishes the different environments[12]. Glasses and other disordered materials are also difficult to analyse by conventional diffraction techniques due to the lack of long-range order, but this has much less effect on the NMR spectrum which depends only on the local, short-range order. NMR is also essentially a quantitative technique with the signal intensity being proportional to the number of nuclei in a particular environment in the sample, giving additional advantage over the traditional infra-red and X-ray fluorescence coordination determination techniques. High resolution solid-state NMR is now becoming an important technique in the investigation of mineral, glass and ceramic systems providing useful structural information.

1.2 Nuclear Shielding

The applied magnetic field (B_o) interacts with the electronic charge of the structure which modifies the magnetic field at the nucleus (B_{loc}). The change of magnetic field is expressed in terms of the shielding (σ) of the nucleus as

$$B_{loc} = (1 - \sigma)\, B_o \qquad [1.1]$$

The shielding constant is identified with an energy term which is bilinear in the magnetic field (B) and the magnetic moment (μ).

$$\sigma(\mu,B) = \frac{\partial^2 E}{\partial \mu \partial B} \qquad [1.2]$$

The change in the magnetic field at the nucleus, when the applied magnetic field is fixed, causes the actual resonance frequency of a particular nucleus to vary and this change is termed the chemical shift (δ_i). The zero of the chemical shift scale for each nucleus is

defined as some arbitrary reference compound relative to which other materials are measured.

$$\delta_i = \frac{\nu_i - \nu_{ref}}{\nu_o} = \sigma_{ref} - \sigma_i \qquad [1.3]$$

For a particular nucleus those nuclei in the least shielded environment resonate at the highest frequency and by convention have the most positive chemical shifts. Theoretical calculation of the nuclear shielding is complex and has only been satisfactorily performed for a few cases of simple, isolated molecules. Generally, the shielding is divided into two distinct contributions, a diamagnetic term (σ_d) and a paramagnetic term (σ_p). A brief discussion of the physical basis of these shielding terms will be given rather than a detailed discussion of their theoretical derivation for which the reader is referred to the literature[13,14].

The diamagnetic term arises from the applied magnetic field inducing circulation of the electronic charge surrounding the nucleus which sets up a magnetic field that opposes B_o in accordance with Lenz's Law. For a spherical charge distribution the diamagnetic term has been calculated in Lamb's formula [Eq.1.4][15]

$$\sigma_d = \frac{\mu_o e^2}{3m_e} \int_o^\infty r\rho_e dr \qquad [1.4]$$

where ρ_e is the electronic charge density, r the electronic charge-nucleus distance and m_e is the electron mass.

The magnetic field also modifies the ground-state electronic wavefunction by mixing in some excited states. This induces a magnetic moment which reinforces the applied field, hence is termed the paramagnetic contribution. The paramagnetic term is strongly dependent on the local symmetry of the electronic charge about the nucleus, being zero for a spherically symmetric distribution. Some simplified expressions for this shielding term have been

derived[13,14] [Eq.1.5] by considering only electrons centred on the nucleus of interest and making certain assumptions such as the average energy approximation[15].

$$\sigma_p = \frac{-\mu_o e^2 \hbar^2}{6\pi m_e^2 \Delta E} [\langle r^{-3} \rangle_p P_u + \langle r^{-3} \rangle_d D_u] \qquad [1.5]$$

where

ΔE - average excitation energy.

$\langle r^{-3} \rangle_{p,d}$ - average of the inverse-cube of the p,d electron-nucleus distance.

P_u, D_u - p,d-electron imbalance derived from the LCAO-MO coefficients.

Calculation of σ_p is difficult since it requires extensive knowledge of the excited states of the system which are usually ill-defined. The net shielding is the sum of two large terms (σ_d, σ_p) of opposite signs with the resultant often subject to large errors. In elements other than the lightest (e.g. ^1H) variations in the shielding are considered to be due to changes in the paramagnetic term. Rather than calculation of the absolute shielding these expressions may be used to explain trends in the chemical shift of related compounds. Reforming Equation 1.5 in terms of physical bonding parameters, including bond polarity (α_p) and the cation-anion bond overlap integral (I_o)[16], σ_p may be written as (p-electrons only)[17]

$$\sigma_p = \frac{-\mu_o e^2 \hbar^2}{\pi m_e^2 \Delta E} \langle r^{-3} \rangle_p [u_i^2(1-u_i^2)] \qquad [1.6]$$

where

$$u_1^2 = \tfrac{1}{4}\left[\frac{1-I_n(1-\alpha_p^2)^{\frac{1}{2}}}{1-I_n^2} \pm \frac{\alpha_p}{(1+\beta_p^2)^{\frac{1}{2}}}\right] \qquad [1.7]$$

$\pm$ - anion/cation

The chemical shift is determined by both the anion-cation bond overlap and the covalency of the bond. In a series of compounds either of these effects can be dominant and this has been demonstrated for sulphides with post-transition metal sulphides depending on the bond polarity while alkaline-earth sulphides depend on the overlap integral[18]. For silicates (and in particular ^{29}Si in SiO_2) the chemical shift is often correlated to secα (α,Si-O-Si bond angle) which has the physical basis that the bond overlap population has been shown to vary linearly with secα over the range $130^\circ<\alpha<180^\circ$[19]. In amorphous materials the increased range of environments compared with crystalline materials (i.e. a range of α) produces a spread of chemical shifts and leads to the increased linewidths.

Although the above has regarded a nucleus in a given environment as having a particular value for σ, it is in reality a second-rank tensor quantity, reflecting the three-dimensional nature of the electronic distribution about the nucleus. As the chemical shift is determined by the bonding to the nucleus each crystallographically distinct site will be characterised by a second-rank shielding tensor. In a powder the local orientation of the principal axes of the tensor cannot be determined from the NMR spectrum alone but the three principal components ($\sigma_1,\sigma_2,\sigma_3$) can. For cubic local symmetry a single isotropic value σ ($=(\sigma_1+\sigma_2+\sigma_3)/3$) is obtained while for lower symmetries characteristic powder patterns are observed (Fig. 1.1 (d), (e)). In characterising a resonance the

isotropic shift is the single most important feature but the anisotropy $\Delta(=\sigma_3-\sigma_1)$ and the asymmetry $\eta(=(\sigma_2-\sigma_1)/(\sigma_3-\sigma))$ also provide information about the nature and the variation of the bonding. This is typified by the anisotropies of differently hybridised carbon-13 species, increasing markedly as the disparity of the bonds increases (i.e. sp^3, Δ~10ppm; sp^2, Δ~150ppm; sp, Δ~200ppm)[15]. The chemical shift information is present in both static and spinning spectra (Sec. 2.3).

1.3 **A Multinuclear Approach**

Modern high frequency, broadband spectrometers allow ready observation of the different nuclei in a material, thereby more fully constraining structural studies. The hundred or so NMR-active isotopes may be conveniently divided into four categories.

(i) Abundant spin-$\frac{1}{2}$ e.g. ^{1}H, ^{19}F.

(ii) Dilute spin-$\frac{1}{2}$ e.g. ^{13}C, ^{29}Si.

(iii) Integer-spin quadrupolar nuclei e.g. ^{2}D, ^{14}N.

(iv) Non-integer spin quadrupolar nuclei e.g. ^{23}Na, ^{27}Al.

For high resolution solid-state studies each group has its own particular difficulties associated with observing the NMR signal. The abundant spin-$\frac{1}{2}$ nuclei give intense signals but are usually strongly dipolar-coupled (Sec. 2.1), so achieving the narrowing required to produce high resolution spectra can be difficult. Dilute spin-$\frac{1}{2}$ do not have strong dipolar-coupling problems, except for when abundant spins are also present in the system, but the signal is usually weak and the spin-lattice relaxation process can be slow. Quadrupolar nuclei possess a quadrupole moment (eQ) which interacts with the electric field gradient (efg, $\partial^2V/\partial z^2=eq$) at the nucleus and can cause considerable broadening of the resonance line. The size of this interaction results in transitions which are first-order quadrupolar broadened being unobservable in solids in all but the most symmetric

materials (Sec. 2.4). Hence solid-state NMR of integer-spin quadrupolar nuclei is likely to be extremely difficult as all the transitions are first-order quadrupolar broadened. Non-integer spin nuclei possess a central transition ($\frac{1}{2} \leftrightarrow -\frac{1}{2}$) which is only affected by the quadrupolar interaction taken to second-order. Useful high resolution spectra can usually be obtained for these nuclei although the peak-position becomes noticeably field-dependent and, due to incomplete excitation of the transition, spectral intensity is lost once the efg becomes sufficiently large (Sec. 2.4).

Concentrating on nuclei which could be of use for NMR experiments on the ceramics of this study, a direct comparison of their sensitivity is useful. Comparing nuclei under similar conditions (e.g. B_0), for samples of similar atomic concentration, a measure of the intensity of the signal is given by the receptivity (R_x)[15]

$$R_x = |\gamma_x^3 C_x I_x (I_x+1)| \qquad [1.8]$$

where

γ_x - gyromagnetic ratio

C_x - natural abundance.

I_x - nuclear spin.

For spin-$\frac{1}{2}$ nuclei R_x gives a direct measure of the observability of a particular nucleus. For quadrupolar nuclei further considerations are necessary, in particular the linewidth factor which depends on the quadrupole moment and nuclear spin and gives a comparison of linewidths produced when different nuclei are in sites with the same efg. For non-integer spin quadrupolar nuclei it is the second-order quadrupolar linewidth of the ($\frac{1}{2} \leftrightarrow -\frac{1}{2}$) transition that is important. At fixed magnetic field the second-order quadrupolar

linewidth is also inversely proportional to the resonance frequency. Polarisation of the inner, core electrons occurs which magnifies the efg and rises rapidly for large Z (atomic number) nuclei (this is called Sternheimer antishielding[20]). There is also the more subjective consideration of the likelihood of a particular nucleus existing in a symmetric environment.

Isotope	Nuclear Spin	Linewidth factor $\frac{L}{m^4} \times 10^{59}$	Operating frequency at B_0=8.45T	Receptivity relative to ^{29}Si at natural abundance
^{14}N	1	—*	26.0	2.7
^{15}N	1/2	—	36.5	0.01
^{17}O	5/2	0.027	48.8	0.03
^{25}Mg	5/2	1.9	22.0	0.73
^{27}Al	5/2	0.9	93.8	569
^{29}Si	1/2	—	71.5	1
^{45}Sc	7/2	1.6	87.5	813
^{89}Y	1/2	—	17.6	0.32
^{139}La	7/2	1.6	50.9	157

$$L = \frac{Q^2}{I^2(2I-1)^2} \times (I(I+1)-3/4)$$ (See Eq. 2.20 second-order quadrupole broadening].

* - all transitions first-order quadrupole broadened

Table 1.1 A comparison of the observability of the nuclei of interest in the oxynitride ceramics of this study.

Of these nuclei the most commonly studied by solid-state NMR are ^{29}Si and ^{27}Al. The interest in these nuclei is a result of their relative ease of observation combined with the range of interesting materials that they occur in. In the seven years since the first high resolution solid-state ^{29}Si spectra from inorganic solids were

obtained[21] the number of studies have rapidly increased. There is a wide range of technologically and geochemically important materials including zeolites[12,22], cements[23], minerals[24] and glasses[25] (e.g. alkali silicates[26,27] and lead silicates[28]) which are based on SiO_4 tetrahedra and are difficult to study using other techniques (e.g. XRD). Structural changes within these materials have been observed by MAS-NMR with changing composition and heat treatment which were previously undetected. This is most elegantly demonstrated by Si/Al ordering in aluminosilicates, with the quantitative aspect of NMR allowing accurate determination of the atomic distributions[23,29].

AlO_4 and AlO_6 coordinations are readily distinguished by ^{27}Al MAS-NMR from their differing chemical shift ranges which was first demonstrated 6 years ago[30]. The range of materials that have been studied by ^{27}Al MAS-NMR is very similar to that by ^{29}Si MAS-NMR, including zeolites[12,31], cements[32], minerals[33], glasses[34] and amorphous aluminas[35]. The quadrupole interaction can provide structural information but it also complicates interpretation of the NMR spectra (Sec. 2.4, 5.2).

High resolution solid-state NMR of the other nuclei in Table 1.1 is far less common. Nitrogen occurs in only a limited number of common inorganic materials and the study of ^{14}N is probably limited to only the most symmetric environments as all the transitions are first-order quadrupole broadened. The low receptivity of ^{15}N results in expensive enrichment being required to allow high resolution NMR study. ^{17}O also requires enrichment but the wide variety of materials containing oxygen make it an attractive nucleus, with materials studied so far including the simple oxides[36], zeolites[37] and minerals[38]. ^{17}O NMR has emphasised how a multinuclear approach greatly enhances the structural characterisation of a material, being exemplified by fosterite (Mg_2SiO_4) with the ^{29}Si MAS-NMR spectrum

showing one resonance and ^{17}O NMR gives three inequivalent oxygen sites. To date interest in the other nuclei ^{25}Mg, ^{45}Sc, ^{89}Y and ^{139}La in the solid-state has been very limited. For ^{25}Mg the relatively low frequency and low receptivity can explain this, whilst for the Group 3B metals the range of interesting materials was relatively limited. These nuclei could provide valuable information for characterising the ceramics of this study.

1.4 Oxynitride Materials

There has been extensive investigation by ^{29}Si MAS-NMR of the large variety of crystalline and glassy materials based on differing arrangements of SiO_4 tetrahedra. The number of possible arrangements is greatly increased when oxygen/nitrogen substitution is allowed to give the complete range of tetrahedral units $SiO_xN_{4-x}(0\leq x\leq 4)$. The study of oxynitrides allows different crystal chemistry with some novel crystal structures to be explored. However, the number of known oxynitrides is small with only one, sinoite found in meteorites of the condrite group, occurring naturally. Single crystal determinations of oxynitride structures have been carried out on a very limited range of materials, so frequently only isotypism to known silicate structures has been shown, with few details about the position of nitrogen in the structures[39].

Interest in oxynitride materials has increased because of the range of technologically important silicon nitride based ceramics that have been developed[40,41,42]. The base compounds silicon nitride and silicon oxynitride have structures made up of fully connected frameworks of SiN_4 and $SiON_3$ tetrahedra respectively. Silicon nitride's high temperature utility is based on its properties of strength, hardness, wear-resistance, high temperature stability, oxidation resistance and low coefficient of thermal expansion which

have resulted in a number of applications including cutting tools, ceramic turbine blades and other high temperature engine components[42]. These properties are only achieved in fully dense specimens and fabrication of such material in the required shapes has proved difficult since the strongly covalent Si-N bond means that self-diffusivity is low and when temperatures are reached where the atoms begin to diffuse the nitride decomposes by volatilisation of nitrogen[42]. Techniques such as hot-pressing have been developed, but to improve densification "fluxing agents" are often used including CaO, MgO, Group 3B oxides (especially yttrium) and rare-earth oxides. The Si_3N_4 powder particles usually have a surface oxidation layer of SiO_2 which reacts with the metal oxide and a little of the Si_3N_4 to give an oxynitride liquid at high temperatures (~1700°C). This liquid allows mass transport and densification by liquid phase sintering at lower temperatures than the pure nitride. Quaternary silicon metal oxynitrides and other phases (Fig. 1.2) form from the liquid in this system which degrade the properties of the Si_3N_4 to some extent.

Alternative control of the phases which form has been developed through the concept of ceramic alloying[43], improving the properties of the ceramic formed. The first ceramic alloy was based on Al^{3+} substitution for Si^{4+} in Si_3N_4 with charge compensation by simultaneous substitution of N^{3-} by O^{2-} [Eq. 1.9], to form the β'-sialon solid solution (sialon is an acronym for materials from Si-Al-O-N and related systems). Other solid-solutions exist including the polytypoids, α'-sialons and O'-sialons (Fig. 1.2) which are predominantly based on arrangements of $(Si, Al)(O,N)_4$ tetrahedra.

$$Si^{4+} + N^{3-} \rightarrow Al^{3+} + O^{2-} \qquad [1.9]$$

The crystalline phases of the system M-Si-Al-O-N (where M is a Group 3B metal) together with the Si-Al-O-N ceramics provide the oxynitride phases of this study. Solid solutions exist (e.g.

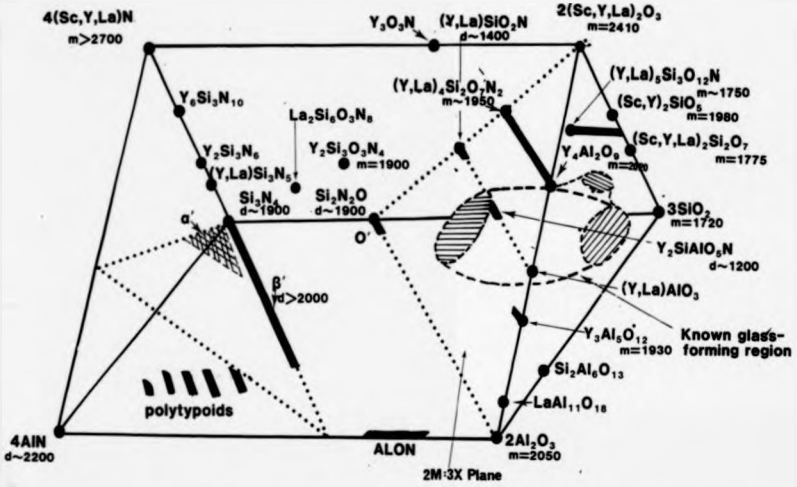

Figure 1.2 Janecke prism showing the phases of the (Sc,Y,La)-Si-Al-O-N system(correct charge equivalence shown for corner members only).Decomposition(d) and melting(m) temperatures in °C for the yttrium compounds.

$Y_4Si_2O_7N_2$ + $Y_4Al_2O_9$) which allow (Si,N)/(Al,O) substitution to be investigated. There are examples of materials which are isostructural with minerals, such as akermanite ($Ca_2MgSi_2O_7$) and M-melilite ($Y_2Si_3O_3N_4$) which are related by the complex substitution

$$2Ca^{2+} + Mg^{2+} + 4O^{2-} \rightarrow 2Y^{3+} + Si^{4+} + 4N^{3-} \qquad [1.10]$$

Materials also exist which have no natural analogue (e.g. $La_2Si_6O_3N_8$) presenting new, largely undefined crystal structures. The range of cations allows the cation influence on the silicon's chemical shift in $Si(O,N)_4$ tetrahedra to be examined, although the ideal experiment of taking one structure with all its possible yttrium/rare-earth substitutions is ruled out because most rare-earth ions have an electronic paramagnetic moment which complicates interpretation.

The phase relationships of the yttrium system are best known[44] while lanthanum has received much less attention[45] and scandium is not believed to form any oxynitrides[46]. Recently both lanthanum[47] and yttrium[44] have been shown to form ternary silicon nitrides (i.e. equivalent to silicates but in a pure nitrogen system), so that SiN_4 networks exist with some "non-bridging" character (i.e. $N^- \dashrightarrow$(La,Y)), allowing a variety of new nitride crystal structures to be examined.

As these structures have elements of similar scattering factors (e.g. Si, Al and O,N), X-ray diffraction has difficulty in distinguishing different atomic distributions within these materials. Neutron diffraction alleviates the problem for oxygen and nitrogen as they have markedly different neutron scattering lengths and a study of some yttrium silicon oxynitrides has identified different SiO_xN_{4-x} ($0 \leq x \leq 4$) units[48]. The sensitivity of the NMR chemical shift to changes in a nucleus's local environment make NMR an ideal probe of

these structures. Previous high resolution NMR of oxynitride ceramics has been limited, with the first two brief reports in 1984 demonstrating the technique's ability to distinguish different local environments for aluminium and silicon in polytypoids[49,50] and sialon X-phase[50] ($Si_3Al_6O_{12}N_2$). This was followed in 1985 by a more complete study of the ^{29}Si resonance in the base compounds silicon nitride and silicon oxynitride, together with the derived β'-sialons[51]. The SiN_4 and SiO_3N resonances could clearly be resolved, both showing a positive shift from the normal range of ^{29}Si in silicates (Sec. 4.1). Additionally the ^{29}Si resonance from the β'-sialons showed no noticeable change in the isotropic shift position, which is close to silicon nitride, at any level of oxygen substitution. A preliminary report of the ^{29}Si resonance from Y-Si-Al-O-N glasses appeared in 1986[52]. The different SiO_xN_{4-x} units could not be completely resolved but shifts for the units present were given from Gaussian fits to the broad glass lines. Recently the ^{29}Si chemical shifts from the base compounds (e.g. Si_3N_4) have been remeasured[53], agreeing with the original work[51]. This latest work has extended the NMR by observing ^{15}N in enriched Si_3N_4 and Si_2N_2O and showed nitrogen was similarly coordinated in an Mg-Si-Al-O-N glass.

References: Chapter 1

1. Purcell, E.M., Torrey, H.C. and Pound, R.V., Phys. Rev. 69, 1946, 37-38.
2. Bloch, F., Hansen, W.W. and Packard, M.E., Phys. Rev. 69, 1946, 127.
3. Knight, W.D., Phys. Rev. 76, 1949, 1259-1260.
4. Proctor, W.G. and Yu, F.C., Phys. Rev. 77, 1950, 717.
5. Dickinson, W.C., Phys. Rev. 77, 1950, 736-737.
6. Arnold, J.T., Dharmatti, S.S. and Packard, M.E., J. Chem. Phys. 19, 1951, 507.
7. Andrew, E.R., Bradbury, A. and Eades, R.G., Nature, 182, 1958, 1659.
8. Pines, A., Gibby, M.G. and Waugh, J.S., J. Chem. Phys. 59, 1973, 569-590.
9. Mehring, M., Pines, A., Rhim, W.K. and Waugh, J.S., J. Chem. Phys. 54, 1971, 3234-3240.
10. Andrew, E.R., Inter. Rev. Phys. Chem. 1, 1981, 195-224.
11. Schaefer, J. and Stejskal, E.O., J. Am. Chem. Soc. 98, 1976, 1031-1032.
12. Klinowski, J., Prog. NMR Spec. 16, 1984, 237-309.
13. Ramsey, N.F., Phys. Rev. 78, 1950, 699-703.
14. Jameson, C.J. and Gutowsky, H.S., J. Chem. Phys. 40, 1964, 1714-1724.
15. Harris, R.K., "NMR Spectroscopy". Pitman 1984.
16. Harrison, W.A., "Electronic Structure and the Properties of Solids", Freeman 1980.
17. Becker, E.D., J. Chem. Phys. 68, 1978, 3785-3793.
18. Eckert, H. and Yesinowski, J.P., J. Am. Chem. Soc. 108, 1986, 2140-2146.
19. Newton, M.D. and Gibbs, G.V., Phys. Chem. Minerals 6, 1980, 221-246.
20. Sternheimer, R., Phys. Rev. 84, 1951, 244-253.
21. Lippmaa, E., Magi, M., Samoson, A., Engelhardt, G., and Grimmer, A.-R., J. Am. Chem. Soc. 102, 1980, 4889-4893.
22. Klinowski, J., Ramdas, S., Thomas, J.M., Fyfe, C.A. and Hartman, J.S., J. Chem. Soc. Faraday Trans. II, 78, 1982, 1025-1050.
23. Barnes, S.R., Clague, A.D.H., Clayden, N.J., Dobson, C.M., Hayes, C.J., Groves, G.W. and Rodger, S.A., J. Mater. Sci. Lett. 4, 1985, 1293-1295.
24. Kirkpatrick, R.J., Smith, K.A., Schramm, S., Turner, G. and Yang, W.H., Ann. Rev. Earth Planet. Sci., 13, 1985, 29-47.
25. Kirkpatrick, R.J., Dunn, T., Schramm, S. Smith, K.A., Oestrike, R. and Turner, G., in "Structure and Bonding in Non-crystalline Solids", Ed. Walrafen, G.E. and Revesz, A.G., Planum Press 1986.
26. Dupree, R., Holland, D., McMillan, P.W. and Pettifer, R.F., J. Non-Cryst. Solids, 68, 1984, 399-410.
27. Dupree, R., Holland, D. and Williams, D.S., J. Non-Cryst. solids, 81, 1986, 185-200.
28. Dupree, R., Ford, N. and Holland, D., Phys. Chem. Glasses, 28, 1987, 78-84.
29. Fyfe, C.A., Gobbi, G.C. and Putnis, A., J. Am. Chem. Soc. 108, 1986, 3218-3223.

30. Muller, D., Gessner, W., Behrens, H.J and Scheler, G., Chem. Phys. Lett., 79, 1981, 59-62.
31. Fyfe, C.A., Gobbi, G.C., Klinowski, J., Thomas, J.M. and Ramdas, S., Nature, 296, 1982, 530-533.
32. Muller, D., Bettel, A., Gessner, W. and Scheler, G., J. Magn. Reson. 57, 1984, 152-156.
33. Kinsey, R.A., Kirkpatrick, R.J., Hower, J., Smith, K.A. and Oldfield, E., Am. Miner. 70, 1985, 537-548.
34. Muller, D., Berger, G., Grunze, I., Ladwig, G., Hallas, E. and Haubenreisser, U., Phys. Chem. Glasses, 24, 1983, 37-42.
35. Dupree, R., Farnan, I., Forty, A.J., El-Mashri, S. and Bottyan, L., J. de Phys. C8, 1985, 113-119.
36. Turner, G., Chung, S.E. and Oldfield, E., J. Magn. Reson. 64, 1985, 316-324.
37. Timken, H.C., Janes, N., Turner, G.L., Lambert, S.L., Welsh, L.B. and Oldfield, E., J. Am. Chem. Soc. 108, 1986, 2236-2241.
38. Schramm, S. and Oldfield, E., J. Am. Chem. Soc., 106, 1984, 2502-2506.
39. Lang, J. in "Progresss in Nitrogen Ceramics", Ed. Riley, F.L., Pub. Martinus, Nijhoff, 1983, 23-43.
40. Jack, K.H. and Wilson, W.I., Nature, 238, 1972, 28.
41. Lewis, M.H., Bhatti, A.R., Lumby, R.J. and North, B., J. Mater. Sci. 15, 1980, 103-113.
42. Jack, K.H., in "Non-Oxide, Technical and Engineering Ceramics", Ed. Hampshire, S., Elsevier Applied Science, 1986 1-30.
43. Jack, K.H., J. Mater. Sci., 11, 1976, 1135-1158.
44. Thompson, D.P. in "Tailoring Multiphase and Composite Ceramics", Ed. Tressler, Messing, Pantano and Newnham, Plenum 1986, 79-91.
45. Mitomo, M., Izumi, F., Horiuchi, S. and Matsui, Y., J. Mater. Sci., 17, 1982, 2359-2364.
46. Morgan, P.E.D., Lange, F.F., Clarke, D.R. and Davis, B.I., Comm. Am. Ceram. Soc. 1981, C(77-78).
47. Inoue, Z., Mitomo, M. and Nobou, I.I., J. Mater. Sci. 15, 1980, 2915-2920.
48. Roult, R., Bacher, P., Liebaut, G., Marchand, R., Goursat, P. and Laurent, Y., Acta. Cryst. A(40) (Supp), 1984, C226.
49. Butler, N.D., Dupree, R. and Lewis, M.H., J. Mater. Sci. Lett. 3, 1984, 469-470.
50. Klinowski, J., Thomas, J.M., Thompson, D.P., Korgul, P., Jack, K.H., Fyfe, C.A. and Gobbi, G.C., Polyhedron, 11, 1984, 1267-1269.
51. Dupree, R., Lewis, M.H., Leng-Ward, G. and Williams, D.S., J. Mater. Sci. Lett. 4, 1984, 561-564.
52. Aujla, R.S., Leng-Ward, G., Lewis, M.H., Seymour, E.F.W., Styles, G.A. and West, G.W., Phil. Mag. 54, 1986, L(51-56).
53. Turner, G.L., Kirkpatrick, R.J., Risbud, S.H. and Oldfield, E., Am. Ceram. Soc. Bull, 66, 1987, 656-663.

CHAPTER 2 THEORETICAL BACKGROUND

2.1 Nuclear Spin Hamiltonian

A nucleus may experience a number of interactions which depend on the orientation of the nuclear spin and are summarised by the Hamiltonian, $\mathcal{H}_{TOT}$ [Eq. 2.1]. The physical basis and the effect on the NMR spectrum of each term will briefly be considered with further details found in the books by Abragam[1] and Slichter[2]. Standard nomenclature will be used throughout.

$$\mathcal{H}_{TOT} = \mathcal{H}_Z + \mathcal{H}_{RF} + \mathcal{H}_D + \mathcal{H}_{CS} + \mathcal{H}_Q + \ldots\ldots \qquad [2.1]$$

The basis of the NMR experiment is the production and detection of transitions between the non-degenerate nuclear energy levels created by the Zeeman interaction of the nuclear magnetic dipole moment, $\underline{\mu}$ ($=\gamma\hbar\underline{I}$, where I is the nuclear spin and γ is the gyromagnetic ratio of the nucleus) with the applied magnetic field, B_0 (which defines the z-direction in space) [Eq. 2.2]. In the high field limit the Zeeman term is dominant and the effects of the other Hamiltonians are regarded as perturbations of the Zeeman levels.

$$\mathcal{H}_Z = -\underline{\mu}.\underline{B}_0 = -\gamma\hbar B_0 m_Z = -\hbar\omega_0 m_Z \qquad [2.2]$$

Where m_Z is the z-component of $I(-I \leq m_Z \leq I)$ and ω_0 is the Larmor frequency.

The Hamiltonian $\mathcal{H}_{RF}$ represents a radiofrequency (RF,M) magnetic field, B_1, applied orthogonal to B_0 and is similar in form to the Zeeman interaction [Eq. 2.3]. From the properties of the raising (I_+) and lowering (I_-) operators states with $\Delta m_Z = \pm 1$ are connected and B_1 induces transitions between the Zeeman levels, but only when its frequency is close to the Larmor frequency. The energy absorbed from the RF-field produces a transverse magnetisation which is detected by

the receiver coil, whose axis is usually orthogonal to B_0, producing the NMR signal.

$$H_{RF} = \frac{-\gamma \hat{B} B_1}{2} (I_+ e^{-i\omega t} + I_- e^{i\omega t}) \qquad [2.3]$$

The applied magnetic fields are experimentally imposed "external" Hamiltonians, while the remaining "internal" terms, the dipolar (H_D), chemical shielding (H_{CS}) and quadrupolar (H_Q) Hamiltonians provide valuable information about the nuclei's local environment via their influence on the Zeeman energy levels. To describe these second-rank internal tensor interactions a common formalism has been developed[3,4] [Eq. 2.4] Rotations are most conveniently handled by using irreducible spherical tensor operators R_{lm} and T_{lm}[3,4]

$$H = C \sum_{l} \sum_{m=-l}^{l} (-1)^m R_{l-m} T_{lm} \qquad [2.4]$$

R_{lm} represents the interaction tensor between two vectors, one of which is always the nuclear spin. The two vectors have been written as a dyadic product which corresponds to T_{lm} [4] and C is an appropriate combination of constants. All second-rank Cartesian tensors may be decomposed into a sum of three spherical tensor operator terms, $R^{(0)}$ a scalar, $R^{(1)}$ an antisymmetric, first-rank spherical traceless tensor and $R^{(2)}$ a traceless, symmetric second-rank spherical tensor. In a first-order approximation only the secular (energy conserving, m=0) terms are considered [Eq. 2.5].

$$H_0 = R_{00} T_{00} + R_{10} T_{10} + R_{20} T_{20} \qquad [2.5]$$

The effects of any antisymmetric components, R_{10}, have been shown to affect the spectra to second-order only[4] and may be neglected. The Cartesian tensor $\underline{R}$ may be expressed in its principal axis system (PAS) so that only the diagonal elements P_1, P_2 and P_3 are

non-zero. It is usual to characterise the interaction in terms of an isotropic value $P_i = \frac{1}{3}(P_1 + P_2 + P_3)$, an anisotropy, $\delta = P_3 - P_i$ and an asymmetry $\eta = \frac{P_2 - P_1}{P_3 - P_i}$ which are related to the only non-zero spherical tensor operator elements in the PAS T_{00}, T_{20} and $T_{2\pm2}$ [Eq. 2.6]

$$T_{00} = P_i \qquad [2.6(a)]$$

$$T_{20} = \frac{\sqrt{3}}{\sqrt{2}}\,\delta \qquad [2.6(b)]$$

$$T_{2\pm2} = \frac{1}{2}\,\eta\,\delta \qquad [2.6(c)]$$

The tensor components in the laboratory frame [Eq. 2.5] can be related to the PAS [Eq. 2.6] by a Wigner rotation matrix[5] with Euler angles (ϕ,θ,ψ) which bring the laboratory frame into coincidence with the PAS [Eq. 2.7]

$$R_{2m} = \sum_{m'} D^{(2)}_{m'm}(\phi,\theta,\psi)\, T_{2m'} \qquad [2.7]$$

This gives the general secular form of the second-rank nuclear spin tensor interaction [Eq. 2.8] with the appropriate parameters for each interaction given in Table 2.1

$$H = P_i\, T_{00}\, C + \frac{\sqrt{1}\,C}{2\sqrt{2}}\, T_{20}\,[(3\cos^2\theta - 1)\delta + \eta\delta\sin^2\theta\cos 2\phi]. \qquad [2.8]$$

Parameter	Interaction		
	Dipolar $\mathcal{H}_D$	Chemical Shielding $\mathcal{H}_{CS}$	Quadrupolar $\mathcal{H}_Q$
C	$-\frac{\mu_0}{4\pi}\frac{\hbar^2\gamma^i\gamma^j}{r_{ij}^3}$	$\gamma\hbar$	$\frac{eQ}{2I(2I-1)}$
T_{00}	0	σ_i	0
δ	1	$\sigma_z-\sigma_i$	$\nu_{zz}(=eq)$
η	0	$\frac{\sigma_x-\sigma_y}{\sigma_z-\sigma_i}$	$\frac{\nu_{xx}-\nu_{yy}}{\nu_{zz}}$
T_{00}	$\underline{I}^i\cdot\underline{I}^j$	$I_z B_0$	$(I)^2$
T_{20}	$\frac{1}{\sqrt{6}}(3I_z^iI_z^j-\underline{I}^i\cdot\underline{I}^j)$	$\frac{\sqrt{2}}{\sqrt{3}}I_zB_0$	$\frac{1}{\sqrt{6}}(3I_z^2-\underline{I}\cdot\underline{I})$

Table 2.1 Interaction tensor parameters for the internal NMR Hamiltonians.

The nuclear dipolar Hamiltonian has the same form as the interaction between two classical magnetic dipoles. It is a traceless ($T_{00}=0$) tensor interaction and is also axially symmetric ($\eta=0$), as it depends only on the disposition of the internuclear vector relative to the applied magnetic field, and has a simple $3\cos^2\theta-1$ angular variation. The chemical shielding tensor $\underline{\sigma}$, due to the electron induced modifications of the magnetic field at the nucleus (Sec. 1.2), has no restrictions on any of its components. The nuclear quadrupole moment (eQ) due to a non-spherical nuclear electric charge distribution which interacts with local electric field gradients (eq) depends upon the nuclear spin orientation. The quadrupole interaction forms a traceless (Laplace's theorem), symmetric second-rank tensor.

From equation 2.8 all these interactions have similar angular dependencies which in powders, where all θ and ϕ values are present,

leads to a broadening of the NMR spectral line. The nuclei in this study are magnetically dilute making the dipolar interaction relatively small resulting in a dipolar linewidth ($\Delta\nu$) of a few kilohertz. The chemical shift anisotropy is usually the dominant broadening mechanism for dilute spin-$\frac{1}{2}$ nuclei and can be as large as ~140ppm for ^{29}Si in crystalline silicates. Quadrupolar broadening depends on the symmetry of the local electric charge surrounding the nucleus, with the quadrupole interaction (e^2qQ/h) varying from 0 to ~10^3 MHz. Quadrupole effects can profoundly influence NMR spectra and will be discussed in Section 2.4. Other interactions such as J-coupling[6] may be present but are usually negligible for the materials of this study.

2.2 High Resolution NMR Spectra

NMR spectral lines of most liquids are much narrower ($\Delta\nu$~Hz) than those of powders due to the random molecular tumbling which averages the angular anisotropic dependencies [Eq. 2.8] to zero, leaving only the isotropic part. By externally imposing a time-dependence on the interactions in powders removal of the anisotropic parts of the internal Hamiltonians occurs in a similar but not identical manner, causing significant narrowing of the NMR spectral lines of powders. The time dependence may be imposed by rapid physical rotation of the whole sample in a rotor (Fig 3.1). The rotor axes may be brought into coincidence with the principal axes of a particular crystallite by a set of rotations described by the Euler angles (ϕ,θ,ψ), while the laboratory frame can be rotated into the rotor frame by a similar set of angles ($0,\beta,\omega_r t$)(Fig 2.1). Wigner rotation matrices are used to make the double angular transformation of the interaction tensors from the PAS to the laboratory frame, yielding the time-dependant laboratory Hamiltonian H(t). Limiting the

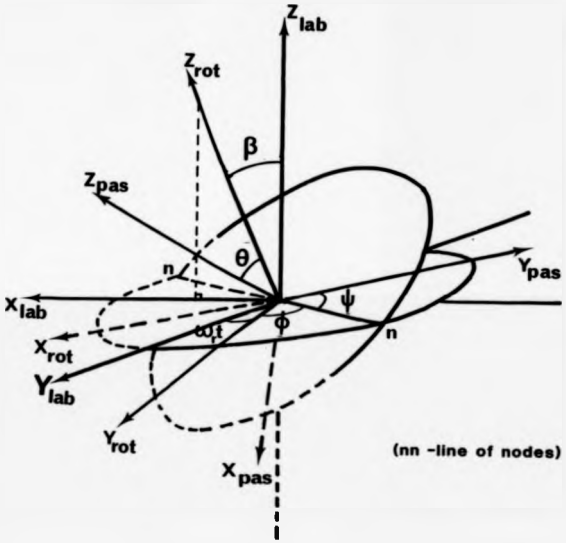

Figure 2.1 Relative orientations of laboratory axes(lab),rotor axes(rot) and principal axes(pas) of a crystallite together with the Euler angles which rotate the laboratory axes to the rotor axes $(0,\beta,\omega_r t)$ and the rotor axes to the principal axes (ϕ,θ,ψ)

expression to secular terms in the laboratory frame gives

$$\overset{Lab}{H(t)} = C\Gamma_{00}\, T_{00} + C\, T_{20} \sum_{m} D^{(2)}_{m0}(0,\beta,\omega_r t) \sum_{m'} D^{(2)}_{m'm}(\phi,\theta,\psi)\Gamma_{2m'} \qquad [2.9]$$

The time-dependent laboratory Hamiltonian can be decomposed [Eq. 2.10] into a static part [Eq. 2.11] and a time-dependent part [Eq. 2.12]

$$H(t) = \bar{H} + H^{*}(t) \qquad [2.10]$$

where

$$\bar{H} = C\Gamma_{00}\Gamma_{00} + \frac{\sqrt{3}}{2\sqrt{2}}\, C\Gamma_{20}\, \frac{3\cos^2\beta-1}{2}\, [(3\cos^2\theta-1)\delta + \eta\delta\sin^2\theta\cos 2\psi] \qquad [2.11]$$

and

$$H^{*}(t) = \frac{\sqrt{3}}{\sqrt{2}}\, C\, T_{20}\, \delta\, (C_1\cos\omega_r t + S_1\sin\omega_r t + C_2\cos 2\omega_r t + S_2\sin 2\omega_r t) \qquad [2.12]$$

(For the definition of C_1, S_1, C_2 and S_2 see Appendix A).

Rapid sample spinning will average the time-dependent term H^{*} to zero leaving $\bar{H}$. Although in a powder the values of θ and ψ take on different values for each crystallite, which is the source of the linebroadening, all crystallites now have a common narrowing factor of $(3\cos^2\beta-1)$. By the choice of $\beta = 54^{\circ}\,44'\,8''$, the so-called magic angle, the Hamiltonian is again reduced to its isotropic part, identical to that of a liquid. This approach works generally for all second-rank tensor interactions provided the restriction to secular terms and rapid enough sample spinning are fulfilled, the latter condition is discussed in section 2.3.

For completeness it should be noted that although the averaging of the anisotropic interactions has been exclusively discussed here in terms of making the spatial geometrical factors time-dependent an alternative approach exists via the manipulation of the spin coordinates. A time-dependence may be imposed upon these coordinates

by the use of an appropriate multiple pulse sequence which can also lead to efficient narrowing[3,4,7].

2.3 NMR in Rotating Solids

The criteria for rapid sample spinning to remove the anisotropic part of the interaction will now be examined. A causality argument would imply that an interaction which produces a spectral width ~$\Delta\nu$ causes the transverse magnetisation to decay in the time domain over a period ~$(1/\Delta\nu)$, hence for any imposed modulation to influence this interaction the modulation should vary over a much shorter time-scale than this, which requires it to have a frequency $\nu_r > \Delta\nu$. For MAS where maximum spinning speeds of ~10kHz are possible this would appear to severely limit the applicability of this technique since NMR linewidths very much greater than this are frequently encountered. However, a distinction has to be drawn between the different types of interaction termed homogeneous and inhomogeneous. A spectral line is considered homogeneous when all nuclei contribute to all parts of the line so that the intrinsic linewidth associated with each spin is the same as the total linewidth. This is typified by a strongly dipolar coupled group of like-spins where spin-diffusion[1] effectively couples together all the spins. An inhomogeneous spectral line is made up of distinct contributions from individual spins which merge into a composite line. A powder with isolated spins consists of differently orientated crystallites which contribute to separate parts of the line and the intrinsic width associated with each spin is considerably narrower than the total linewidth. To cause effective narrowing the spinning rate has to be faster than the intrinsic linewidth associated with each individual spin. A more rigorous distinction between these two interactions is

given by average Hamiltonian theory, depending on the commutation or not of their Hamiltonians at different times[8]. For inhomogeneous interactions these terms commute meaning precise averaging can occur when the rate of rotation is small compared to the total spectral range $\Delta\nu$. An alternative view of MAS-averaging is for it to be effective the spin should not change its state during the rotation period.

Following an RF-pulse the transverse magnetisation decays rapidly ($\sim 1/\Delta\nu$) as it would for a stationary sample, as the spins lose phase coherence, but after one rotation period in a slowly rotating sample ($\nu_r < \Delta\nu$) the system has returned to its initial state [Eq 2.12] which will be shown to result in the formation of a rotational spin-echo. This is true for any inhomogeneous interaction which includes chemical shielding, first-order quadrupole and dipolar coupling between unlike spins. Taking chemical shielding as an example (following closely the approach of Maricq and Waugh[8]) in a powder sample where there is one distinct site, the differently orientated crystallites correspond to individual spin packets i (i.e. intrinsic contributions). In an MAS-NMR experiment after a time t each spin packet initially aligned along the x-axis has precessed to an azimuthal angle $\phi_i(t)$ [Eq 2.13]

$$\phi_i(t) = \int_0^t \omega_i(t')dt' = \omega_0\sigma t + \omega_0\delta \int_0^t \overset{*}{H}_i(t')dt' \qquad [2.13]$$

The time-domain signal $g_E(t)$ is then

$$g_E(t) = \sum_i \exp\,(i\phi_i(t)) = \exp(i\omega_0\sigma t) \sum_i \exp(i\omega_0\delta \int_0^t \overset{*}{H}_i(t')dt') \quad [2.14]$$

As $\overset{*}{H}_i(t)$ is a purely oscillatory function [Eq 2.12] its integral [Eqs 2.13, 2.14,] vanishes at $t = 2\pi P/\omega_r$ (P = integer). The range of powder particle orientations mean that the initial

macroscopic transverse magnetisation decays rapidly as the spin packets lose phase coherence but as the integral ($\int \vec{H}_1(t)\,dt$) is zero after a complete rotation the spin packets have regained their original coherence forming a rotational spin-echo. The prefactor in Eq. 2.14 represents a common, much slower precession of the azimuthal direction between the echoes so that the time-domain signal is a train of equally spaced, identically shaped rotational spin-echoes, $g_E(t)$, whose amplitude follow an isotropic variation (Fig. 2.2(a)], $g_I(t)$. The overall time-domain signal may be expressed as

$$g(t) = g_I(t)\ [\ \sum_{p=-\infty}^{\infty} \delta(t - p\,\frac{2\pi}{\omega_r}) * g_E(t)] \qquad [2.15]$$

(* means convolution)

The echo-train greatly prolongs the existence of the transverse magnetisation in the time-domain giving rise to the narrow isotropic part of the spectrum. The frequency spectrum is obtained by Fourier transforming Eq. 2.15 to give Eq. 2.16.

$$G(\omega) = [G_I(\omega) * \delta(\omega - P\omega_r)] \times G_E(\omega) \qquad [2.16]$$

Where $G_{I,E}(\omega)$ are the individual Fourier transforms of $g_{I,E}(t)$.

The spectrum consists of a series of replicas of the isotropic lineshape separated by the spinning speed (Fig. 2.2(b)] with their intensity envelope following the Fourier transform of the individual rotational echoes from which information about the anisotropic part of the interaction may be deduced. In the limit $\omega_r \to 0$ this envelope, $G_E(\omega)$, follows the static powder pattern, but at non-zero ω_r $G_E(\omega)$ becomes complicated as a result of the rotation of the sample through a finite angle during the lifetime of the echo. The echo shape $g_E(t)$ and hence the sideband envelope may be calculated explicitly, thus the tensor elements may be deduced by techniques including moment

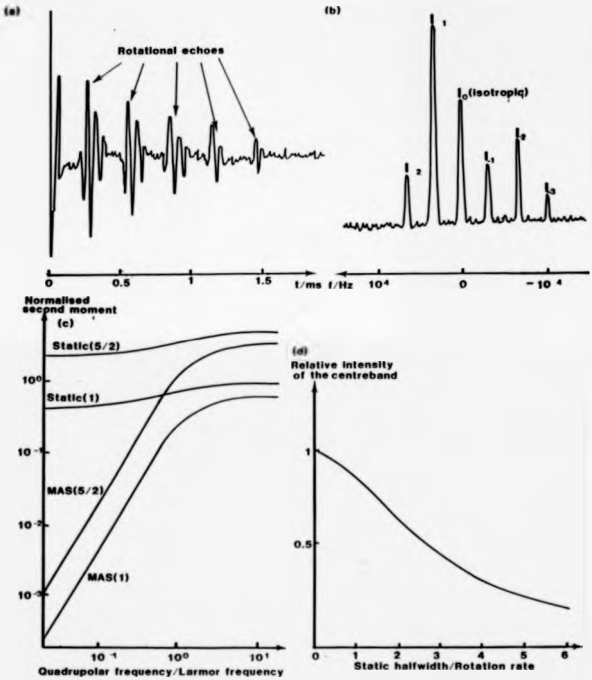

Figure2.2 (a)Time domain signal of ^{119}Sn ($\nu_0 \approx 134$MHz) in SnO_2 showing the rotational echoes and its Fourier transform (b) showing the spinning sidebands(‡) in the frequency domain. (c)The second moment of spin-1/2 nucleus spectra, dipolar coupled to a quadrupolar nucleus as a function of the ratio(quadrupolar Zeeman) for I=1.5,2(after (11)). (d)The change of intensity with spinning speed of the centreband of an MAS spectrum of a heteronuclear dipolar coupled system(after (12)).

analysis[8], Herzfeld and Berger graphical analysis[9] and spectral simulation[10].

The above analysis applies equally to any inhomogeneous interaction. If more than one inhomogeneous interaction exists the total interaction is just the sum of individual interactions provided that the relative orientations of the PAS's of each tensor are taken into account. If any of the interactions are homogeneous the overall interaction becomes homogeneous[8].

To obtain high resolution spectra from inhomogeneous interactions the spinning speed needs only to ensure that the separation of the sidebands exceeds any residual linebroadening. Sources of residual broadening include inhomogeneity of the magnetic field, magic angle setting/stability and sample perfection. In perfectly crystalline materials there are distinct values characterising the interaction tensors at particular sites, whereas for imperfect materials there will be a range of environments due to some "disorder" of which amorphous materials are extreme examples. Hence it is strictly incorrect to assign a single isotropic value to such materials since there is a range of such values with the nominal "isotropic" position usually quoted being an average. If a dipolar coupling exists between the resonant nucleus and a quadrupolar nucleus, which has a large quadrupole interaction in addition to its Zeeman interaction, the quadrupolar nuclei's spin is quantised by both. Linebroadening can then occur as the dipolar Hamiltonian no longer has a simple $3\cos^2\theta-1$ variation, so that MAS can only partially average the interaction (Fig 2.2(c))[11]

Although high resolution spectra are possible at spinning speeds less than the linewidth it is still desirable to spin as fast as possible since there are $\sim\Delta\nu/\nu_r$ spinning sidebands, and if each

makes an independent contribution to the noise the voltage signal-to-noise is degraded by $(\Delta\nu/\nu_r)^{\frac{1}{2}}$ compared to the case of a purely isotropic spectrum, when the sideband intensity is deposited in the centreband. The gain of intensity of the centreband with increasing speed is illustrated for the heteronuclear dipolar interaction (Fig 2.2(d)].

2.4 The Nuclear Quadrupole Interaction and Sample Spinning

For quadrupole nuclei there are a number of features which complicate the NMR spectrum. The full quadrupole Hamiltonian (η=0 for simplicity) in the laboratory frame with an angle θ between the Z-axis of the PAS and B_o is[1,13]

$$\mathcal{H}_Q = \frac{hC_q}{8I(2I-1)}\{(3\cos^2\theta-1)(3I_z^2-a) + 3\sin\theta\cos\theta(I_z(I_+ + I_-) + (I_+ + I_-)I_z + \frac{3}{2}\sin^2\theta(I_+^2 + I_-^2)\} \qquad [2.17]$$

Where $C_q = \frac{e^2qQ}{h}$ and $a = I(I+1)$.

If the applied magnetic field is large compared with the quadrupole interaction, the quadrupole interaction may be regarded as a perturbation, with the total energy of the m^{th} level given by standard perturbation theory[1,13] [Eqs. 2.18(a)-(e)].

$$E_m = E_m^{(0)} + E_m^{(1)} + E_m^{(2)} + \ldots\ldots \qquad [2.18(a)]$$

$$= \langle m|\mathcal{H}_Z|m\rangle + \langle m|\mathcal{H}_Q|m\rangle + \sum_{m\neq m'} \frac{\langle m'|\mathcal{H}_Q|m\rangle\langle m|\mathcal{H}_Q|m'\rangle}{E_m^{(0)} - E_{m'}^{(0)}} \qquad [2.18(b)]$$

Where

$$E_m^{(0)} = -h\nu_o m \qquad [2.18(c)]$$

$$E_m^{(1)} = \frac{3hC_q}{8I(2I-1)}(3\cos^2\theta-1)(m^2-a/3) \qquad [2.18(d)]$$

$$E_m^{(2)} = \frac{-9}{128}\frac{hC_q}{\nu_o}^2\frac{m}{I^2(2I-1)^2}(\sin^2 2\theta(8m^2-4a+1)+\sin^4\theta(-2m^2+2a-1)) \qquad [2.18(e)]$$

The conventional first-order approximation considers only $E_m^{(1)}$ which leads to a splitting of the unperturbed Larmor frequency into 2I components (Fig 2.3(a),(b)) of intensity $|\langle m-1|I_x|m\rangle|^2$ $(\frac{1}{2}I(I+1)-m(m-1)]$ at frequencies $\nu_m^{(1)}$ [Eq 2.19].

$$\nu_m^{(1)} = \frac{-3C_Q}{4I(2I-1)}(3\cos^2\theta-1)(m-\tfrac{1}{2}) \qquad [2.19]$$

This first-order perturbation can cause the satellite transitions to be shifted by $\nu_Q(=3e^2qQ/2I(2I-1)h)$, which can be up to ~MHz away from the Larmor frequency. Fortunately for half-integer spin quadrupolar nuclei it is clear [Eq 2.19] that the central transition ($\frac{1}{2}\leftrightarrow-\frac{1}{2}$) experiences no first-order broadening, hence second-order effects become significant [Eq 2.20].

$$\nu_{\frac{1}{2}}^{(2)} = \frac{-9C_Q^2}{64\nu_0 I^2(2I-1)^2}(a-3/4)(1-\cos^2\theta)(9\cos^2\theta-1) \qquad [2.20]$$

The static powder NMR lineshapes for first-order perturbed (Fig. 2.3(b)] and second-order perturbed central transition (Fig 2.3(c)] may be calculated by integrating equations 2.19, 2.20 over all possible angles. The central transition is a factor ~$3C_Q/(2I(2I-1)\nu_0)$ narrower than the first-order quadrupole spectrum. For a given quadrupole coupling strength (C_Q) and field (B_0) narrower spectra are obtained from nuclei with higher Larmor frequencies and larger spins.

To produce high resolution spectra from first-order quadrupole perturbed transitions would require extremely accurate setting of the magic angle coupled with impratically fast spinning speeds. This combined with the more complex angular variation of the second-order perturbation were the initial causes of pessimism with which the production of high resolution spectra of quadrupole nuclei were regarded. Calculations of the central lineshape under MAS conditions[14,15] show that although the second-order term does not

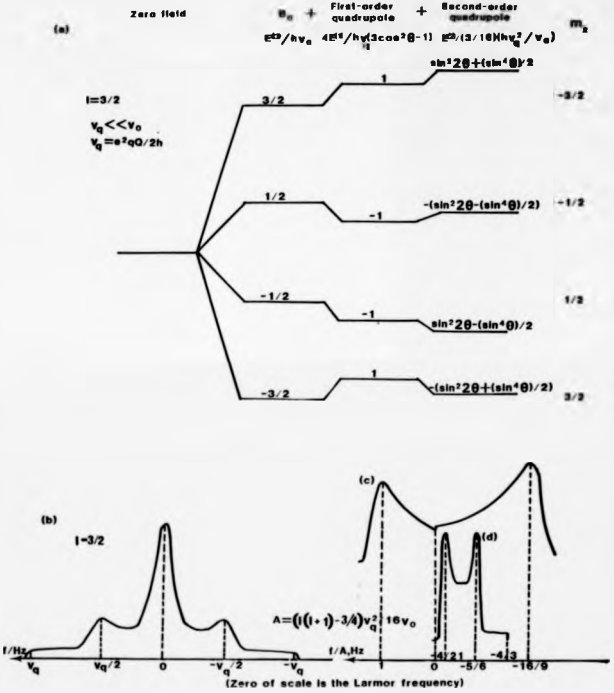

Figure2.2 (a)Energy level diagram of a spin-3/2 nucleus showing the quadrupole perturbations of the Zeeman energy levels with the resulting (b)first-order NMR powder pattern of all the transitions and the second-order spectra of the central transition(1/2,-1/2) for both (c)static and (d)MAS cases.(η=0)

reduce to zero, significant narrowing ~4(Fig 2.4(a)) occurs, hence it is possible to produce high resolution spectra from the central transition if C_q is not too large. The central transition still has a characteristic lineshape (Fig 2.3(d)), so provided other broadening mechanisms do not wash out the structure, the quadrupolar coupling strength and asymmetry parameter may be deduced. If the second-order quadrupolar interaction is dominant it has been shown that its angular dependence [Eq 2.20] is most efficiently narrowed by spinning at angles other than the magic angle and this is termed variable angle sample spinning[14,16].

To examine the second-order perturbation of all the transitions in more detail standard second-order perturbation theory cannot be employed when the first-order interaction is effectively averaged to zero by MAS[14,17]. Taking the results directly from the literature[17] the frequency of the (m↔m-1) transition due to second-order quadrupole effects is

$$\nu_m^{(2)} = \frac{3C_q^2}{32\nu_0 I^2(2I-1)^2}\{(1+\frac{\eta^2}{3})(2a-14m(m-1)-5) - \frac{2}{9}(B^2+C^2+2D^2+2F^2)(6a-34m(m-1)-13] \quad [2.21]$$

(For the definitions of the angular functions B,C,D and F see Appendix A).

Averaging Eq. 2.21 over all crystallite orientations yields the powder MAS spectrum. There is a quadrupolar induced shift of the centre of gravity of these powder patterns away from the unperturbed Larmor frequency[18] [Eq 2.22].

$$\nu_{m,cg}^{(2)} = \frac{3}{40}\frac{C_q^2}{\nu_0}\frac{a-9m(m-1)-3}{I^2(2I-1)^2}(1+\frac{\eta^2}{3}) \quad [2.22]$$

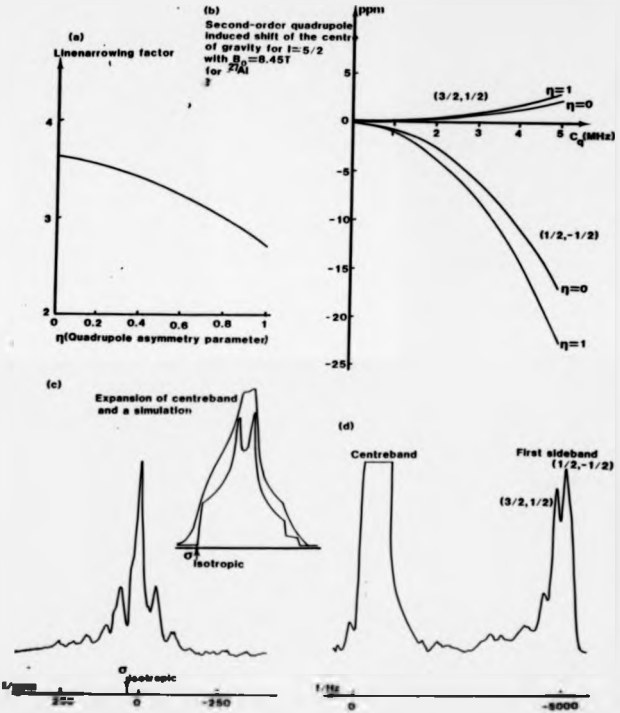

Figure 2.4 (a)MAS narrowing factor as a function of η for a second-order quadrupole broadened central transition (, after [14]). (b)Quadrupole induced shift of the centre of gravity away from the isotropic shift position. (c) Demonstration of (b) ,Al-27 in andalusite(Al_2SiO_5)AlO_6 unit with C_q=6.9MHz,η=0.69. (d)Mn-55(89MHz) spinning spectrum(ν_r=4.6kHz),of $KMnO_4$ showing the different second-order quadrupolar shifts of the transitions.

This shift can have a profound effect on the peak position (Fig 2.4(b), Table 2.2) as is illustrated for the aluminium-27 resonance in andalusite (Fig 2.4(c)). There is both octahedral (C_q=15MHz, η=0.1) and pentacoordinate (C_q=5.9MHz, η=0.7)[19] aluminium present but the large C_q value for the octahedral site broadens even the central transition beyond detection. The centre of gravity of the AlO_5 peak is shifted by ~ -35ppm (at B_o=8.45T) from the isotropic chemical shift which makes it appear to be in an octahedral resonance position at ~4ppm. It has been suggested that when C_q is unknown it is more accurate to obtain the chemical shift from the centre of gravity of the higher order transitions[18]. These transitions are characterised by the quadrupole shift of the centre of gravity, the linewidth and amplitude. The amplitude of the first sidebands have been calculated[18] since they are the most readily observed features of these higher transitions as their central part is obscured by the prominent $(\frac{1}{2},-\frac{1}{2})$ transition. The shape of the rotational sidebands will depend on K[Eq. 2.23], a measure of the first-order broadening of the transition relative to the spinning speed.

$$K = \frac{3(2m-1)C_q}{4I(2I-1)\nu_r} \qquad [2.23]$$

Exact evaluation of the lineshape is not possible although numerical calculations analogous to Herzfeld and Berger give the relative intensity of the sidebands[18]. The amplitude of the sidebands is a product of the inherent quantum intensity, the lineshape and the inverse of the overall linewidth (Table 2.2). Table 2.2 clearly shows that there is sufficient amplitude to make this technique useful for the (1/2, 1/2) transition of I=5/2 (see Fig 2.4 (d) for this transition in ^{55}Mn in $KMnO_4$) and the (5/2,1/2) transition for I=9/2.

Table 2.2 Quadrupole parameters for different spins (last 3 columns after (18))

Spin I	Transition	I^2 a-m(m-1)	Y $\frac{3}{2a(2I+1)}$	A 2I(2I-1)	B a-3/4	90° Pulse Length $\frac{1}{Z}$	Peak pulse magnetisation ZY	Quadrupole shift of centre of gravity $\frac{3(a-9m(m-1)-3)}{10A^2}$ (Units $\zeta_q^2/\nu_0 J$=0)	Relative linewidth $\frac{6a-34m(m-1)-13}{6a-9/2}$ and spin-narrowing factor of $(\frac{1}{2},-\frac{1}{2})$transition (B/A^2)	Amplitude of first rotation sideband of higher transition in relation to centre$(\frac{1}{2},-\frac{1}{2})$ transition.
$\frac{3}{2}$	All	-	$\frac{1}{10}$	6	3	1	1	-	-	-
	$\frac{3}{2},\frac{1}{2}$	3				0.578	0.173	-0.050	-0.889	0.031
	$\frac{1}{2},-\frac{1}{2}$	4				0.500	0.200	0.025	1, $\frac{1}{12}$	-
$\frac{5}{2}$	All	-	$\frac{1}{35}$	20	8	1	1	-	-	-
	$\frac{5}{2},\frac{3}{2}$	5				0.447	0.064	-0.021	-1.833	0.0056
	$\frac{3}{2},\frac{1}{2}$	8				0.354	0.081	-0.0008	0.292	0.12
	$+\frac{1}{2},-\frac{1}{2}$	9				0.333	0.086	0.0060	1, $\frac{1}{50}$	-
$\frac{7}{2}$	All	-	$\frac{1}{84}$	42	15	1	1	-	-	-
	$\frac{7}{2},\frac{5}{2}$	7				0.378	0.031	-0.0112	-2.40	0.0022
	$\frac{5}{2},\frac{3}{2}$	12				0.289	0.041	-0.0036	-0.511	0.027
	$\frac{3}{2},\frac{1}{2}$	15				0.258	0.046	0.0010	0.622	0.055
	$\frac{1}{2},-\frac{1}{2}$	16				0.250	0.048	0.0026	1, 5/588	-

Spin I	Transition	Z^2 a-m(m-1)	Y $\frac{3}{2a(2I+1)}$	A $2I(2I-1)$	B a-3/4	90 Pulse Length $\frac{1}{2}$	Peak pulse magnetisation ZY	Quadrupole shift of centre of gravity $\frac{3(a-9m(m-1)-3)}{10A^2}$ (Units $\frac{\chi_Q^2}{\nu_0}$,I=0)	Relative linewidth $\frac{6a-34m(m-1)-13}{6a-9/2}$ and spin-narrowing factor of $(\frac{1}{2},-\frac{1}{2})$transition (B/A^2)	Amplitude of first rotation sideband of higher transition in relation to centre$(\frac{1}{2},-\frac{1}{2})$ transition.
$\frac{9}{2}$	All	-	$\frac{1}{165}$	72	24	1	1	-	-	-
	$\frac{9}{2},\frac{7}{2}$	9				0.333	0.018	- 0.0070	-2.778	0.0012
	$\frac{7}{2},\frac{5}{2}$	16				0.250	0.024	- 0.0033	-1.125	0.007
	$\frac{5}{2},\frac{3}{2}$	21				0.218	0.028	-0.0007	0.056	0.28 *
	$\frac{3}{2},\frac{1}{2}$	24				0.204	0.030	0.0009	0.764	0.046
	$\frac{1}{2},\frac{-1}{2}$	25				0.200	0.030	0.0014	1, 1/216	-

(* - suitable for determining the isotropic chemical shift)

The quadrupole interaction can also affect the line intensities. With pulse techniques the relative intensities of the split spectral transitions depend upon the excitation employed and the size of the quadrupole coupling constant. A thorough investigation of the pulse response of a quadrupole-split spin system using the fictitious spin-$\frac{1}{2}$ formalism[20] shows how the relative intensities change (Table 2.2), provided the excitation is uniform. While the RF-pulse is on, the Hamiltonian, H_p in the frame rotating at the Larmor frequency, for a stationary sample is the sum of two components (Eq. 2.24 with η=0 for simplicity).

$$H_p = \frac{hC_q}{8I(2I-1)}(3\cos^2\theta-1)(3I_z^2-a) - h\nu_1 I_x \qquad [2.24]$$

The time evolution of the spin system may be evaluated directly from equation 2.24 for the two extreme cases $\nu_1(\gamma B_1/2\pi)>>\nu_q$ and $\nu_1<<\nu_q$. In the former case the magnetisation of all the transitions precesses coherently at ν_1, while in the other extreme the precession frequency of the central transition is $\nu_1/(I+\frac{1}{2})$, which is illustrated experimentally for sodium-23 (Fig 2.5(a)) and theoretically for an I=5/2 system (Fig 2.5(b))[21]. It is important to realise this since conditions are often set-up (i.e. the 90°-pulse length determined) on a solution where ν_q~0 while the solid-state samples often represent the large ν_q limit. Between these two extremes the time evolution during the RF-pulse allows the quadrupole interaction strength to be deduced using the two-dimensional NMR quadrupole nutation method[22,23,24]. This nutation can seriously distort the central transition lineshape as illustrated by the lanthanum-139 resonance in $LaAlO_3$ (C_q=6MHz, Fig. 2.5(c)), where even a 1μs pulse distorts the

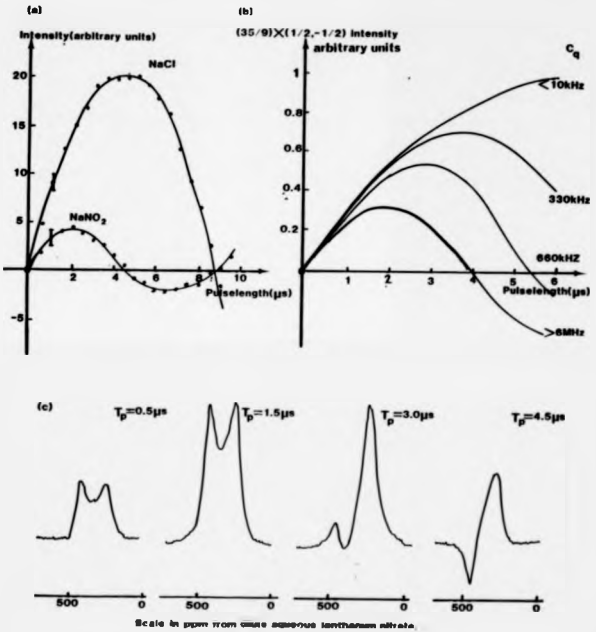

Figure2.8 (a)An experimental plot of the intensity of the Na-23(105MHz) resonance in NaCl(C_q~0) and $NaNO_3$ (C_q~ 1.1MHz) as a functionof pulselength(B_1~8mT). (b)Theoretical plots of the (1/2,-1/2) intensity of Al-27(spin-5/2) nucleus (B_1~4mT, after [21]). (c)The quadrupole distortion of the central transition of the static La-138 spectrum of $LaAlO_3$ (C_q~660Hz) for different pulselengths(T_p:B_1~8mT, B_0= 8.45T).

lineshape, in agreement with theoretical calculations[21,23]. To minimise these effects to produce accurately quantitative high resolution NMR spectra of quadrupole nuclei high magnetic fields in conjunction with short, intense RF-pulses (Fig 2.5(b)) should be employed. For <5% error in signal intensity the effective flip angle should satisfy equation 2.25[25]. The problems of quantitative interpretation of quadrupolar NMR spectra will be discussed in more detail in Chapter 5.

$$(I + \tfrac{1}{2})\ \omega_1 T_p \leq \frac{\pi}{6} \qquad [2.25]$$

Where T_p is the RF-pulse duration.

The production of high resolution spectra of integer-spin nuclei in the solid-state is restricted to those materials where the nucleus is in a relatively symmetric environment as all the transitions experience first-order quadrupole broadening. This will be illustrated for nitrogen-14 in Chapter 6.

References: Chapter 2

1. Abragam, A., 'Principles of Nuclear Magnetism', OUP, 1961.
2. Slichter, C.P., 'Principles of Magnetic Resonance', Springer-Verlag (2nd edition), 1978.
3. Mehring, M., 'Principles of High Resolution NMR in Solids', Springer-Verlag (2nd edition), 1983.
4. Haeberlen, U., 'High Resolution NMR in solids', Ad. Mag. Res. (Ed Waugh, J.S.), Supp. 1, Academic Press, 1976.
5. Rose, M.E., 'Elementary Theory of Angular Momentum', J. Wiley and Son, 1963.
6. Andrew, E.R., Prog. NMR Spec. 8, 1971, 1-40.
7. Mansfield, P., Prog. NMR Spec. 8, 1971, 40-101.
8. Maricq, M. and Waugh, J.S., J. Chem. Phys. 70, 1979, 3300-3316.
9. Herzfeld, J. and Berger, A.E., J. Chem. Phys. 73, 1980, 6021-6030.
10. Clayden, N.J., Dobson, C.M., Lian, L.Y. and Smith, D.J., J. Magn. Reson. 69, 1986, 476-487.
11. Bohm, J., Fenkze, D. and Pfeifer, H., J. Magn. Reson. 55, 1983, 197-204.
12. Pfeifer, H., Proc. RAMIS, 1985, 87-103.
13. Cohen, M. and Reif, F., Sol. St. Phys. 5, 1957, 321-438.
14. Behrens, H.H. and Schnabel, B., Physica. 114B, 1981, 185-190.
15. Muller, D., Ann. Phys. 39, 1982, 451-460.
16. Ganapathy, S., Schramm, S. and Oldfield, E., J. Chem. Phys. 77, 1982, 4360-4365.
17. Kundla, E., Samoson, A. and Lippmaa, E., Chem. Phys. Lett. 83, 1981, 229-232.
18. Samoson, A., Chem. Phys. Lett., 119, 1985, 29-32.
19. Tsang, T. and Ghose, S., Am. Miner. 58, 1973, 748-755.
20. Schmidt, V.H., Ampere Int. Summer School II 'Pulsed Magnetic and Optical Resonance', 1971, 75-83.
21. Fenkze, D., Freude, D., Frolich, T. and Haase, J., Chem. Phys. Lett. 111, 1984, 171-175.
22. Samoson, A. and Lippmaa, E., Chem. Phys. Lett. 100, 1983, 205-208.
23. Samoson, A. and Lippmaa, E., Phys. Rev. B 28, 1983, 6567-6570.
24. Geurts, F.M.M., Rentgens, A.P.M. and Veeman, W.S., Chem. Phys. Lett. 120, 1985, 206-210.
25. Lippmaa, E., Samoson, A. and Magi, M., J. Am. Chem. Soc. 108, 1986, 1730-1735.

CHAPTER 3. EXPERIMENTAL

3.1 Introduction to Pulsed Fourier Transform NMR

One of the major revolutions in NMR spectroscopy was the introduction of the pulse technique by Hahn[1] in 1950 which has now largely replaced the original continuous wave (CW) method. It was shown by Lowe and Norberg[2] that the impulse response function of the spin system, which is the free induction decay (FID) following a short RF-pulse, forms a Fourier pair with the frequency spectrum (i.e. they contain identical information). This was demonstrated experimentally by Clark[3] using a field-sweep, boxcar integration method and by Ernst and Anderson[4] using a computational Fourier transform (FT) of the FID after a single pulse. With the advent of fast FT algorithms (due to J.W. Cooley and J.W. Tukey[5]) and cheap minicomputers which could be dedicated to the spectrometer the FT-pulse technique became useful for high resolution applications giving some advantages, such as time efficiency over the CW method, especially for multiline spectra[4]. A general outline of the basic elements of a pulsed NMR spectrometer (Fig. 3.1(a)) will be given, with particular emphasis on the requirements for high resolution solid-state applications.

A large magnetic field (B_0) is applied to the sample resulting in a net macroscopic nuclear magnetisation on which the experiment is performed. Larger magnetic fields improve both the sensitivity by increasing the Boltzmann factor and the resolution by increasing the chemical shift dispersion. However, large magnetic fields can have an adverse effect on linewidths if chemical shift anisotropy is the principal linebroadening mechanism although any second-order quadrupolar broadening is reduced. For the magnetic field not to contribute noticeably to the linewidth it should be homogeneous over the sample volume and should not drift over the timescale of the

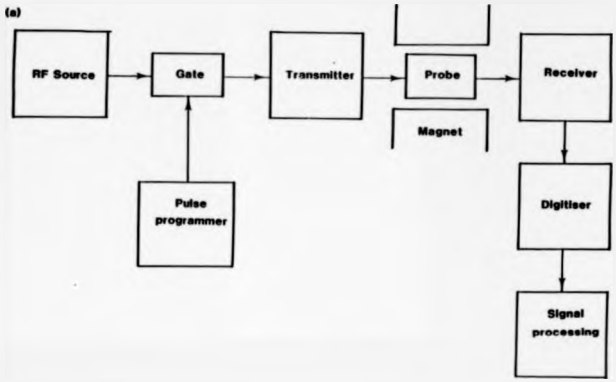

(b) RF Pulse

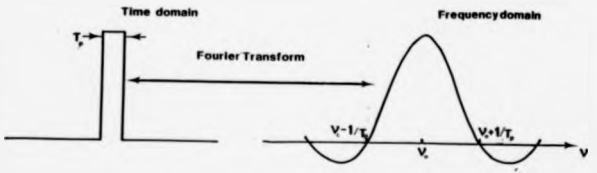

Figure 3.1 (a) The basic components of a pulsed NMR spectrometer. (b) The relationship between the time and frequency domains of an RF-pulse of frequency ν_c and duration τ_p.

experiment which may be many hours for some slowly relaxing systems. Most high resolution spectrometers are equipped with superconducting cryomagnets and generally for high resolution work it is advantageous to work at as high a field as possible.

A pulsed NMR experiment involves the manipulation of the magnetisation by a sequence of RF-pulses applied close to the Larmor frequency of the nucleus of interest, so a fixed field multinuclear system should be capable of generating stable frequencies over a wide range. The frequency source is gated by a pulse programmer which should be highly flexible to allow the production of complex sequences containing pulses of differing lengths, spacing and phase. This drives the RF transmitter which should be capable of generating short (~1μs), intense (~1kW) rectangular pulses.

The transmitter applies RF-pulses to the probe which is a tunable electrical circuit capable of withstanding the transmitter pulse (~kV) as well as being able to convert the precessing nuclear magnetisation into a voltage (~μV) for detection by the receiver. It is important to design the circuit so the probe efficiently couples to both the transmitter the receiver in turn, while isolating one from the other which is often accomplished by the Lowe and Tarr circuit[6]. At the heart of the probe circuit is the NMR coil within which the sample-containing spinner sits. The spinners are carefully designed to allow rapid rotation (~kHz) of the sample, necessary to produce narrowing of solid-state spectral lines. The coil converts the RF-pulses into an oscillating (~ν_0) magnetic field (B_1) whose effect on the magnetisation can best be seen by employing the classical Bloch vector model in the rotating reference frame[7]. A pulse of duration T_p applied exactly on resonance produces a resultant field B_1, orthogonal to B_0, causing a coherent oscillation of the magnetisation

which is "tipped" away from B_o by an angle θ_p [Eq. 3.1] towards the transverse direction containing the coil.

$$\theta_p = \gamma B_1 T_p \qquad [3.1]$$

By FT of the pulse's envelope its spectral irradiation is found which for an ideal rectangular pulse applied at ν_o produces $\mathrm{sinc}(\pi(\nu-\nu_o)T_p)$ (Fig. 3.1(b)). To ensure that all lines or parts of lines are irradiated uniformly (which in the classical Bloch picture means all parts of the spectrum experience equal tip angles) requires that the spectral range of interests lies at the centre of this sinc-function. In the solid-state particularly broad lines may be encountered, hence the necessity for short, intense RF-pulses.

The transverse magnetisation precesses, inducing a small voltage in the coil which is amplified in the preamplifier before passing to the receiver for detection. The receiver should recover rapidly from any overload produced by the RF-pulse and this is especially important for broad lines which decay rapidly in the time domain, as a large proportion of the signal is contained in the interval immediately after the pulse. Other corruptions of the early part of the FID due to spurious ringing effects, which can be caused by pulse induced mechanical oscillations of parts of the probe[8] or by the RF-filters[9], should be reduced to as small a value as practicable to prevent severe lineshape distortion.

The amplified signal is usually detected by a phase sensitive method (PSD) which is necessary for FT methods of signals with small signal-to-noise (S/N) ratios[8]. Most modern high resolution spectrometers employ two PSDs in quadrature configuration which allows more efficient spectral irradiation by placing the applied frequency at the centre of the spectral range and improves the S/N by $\sqrt{2}$ over a single PSD[8]. The filtered signal is then changed into digital form

before it is stored on computer for later manipulation. The maximum spectral range (usually termed sweepwidth even though nothing is actually swept) which may be examined in a single experiment depends on the time between successive data points which is termed the dwell time. For solid-state spectrometers dwell times $\leq 0.5\mu s$ should be available.

3.2 Signal-to-Noise Optimisation of Pulsed NMR Experiments

To enhance the S/N multiscan operation is employed, with n coherently added FIDs leading to an improvement of $\sqrt{n}$ in S/N compared to one pulse, for a system in equilibrium. When the spin-lattice relaxation time (T_1) is short, it is conventional to apply 90°-pulses with at least $4T_1$ between pulses to produce fully relaxed, quantitative spectra. For samples with long T_1's (~hours) it becomes important to carefully optimise experimental parameters so that an adequate S/N may be accumulated at a reasonable rate. For dilute spin-½ nuclei in solid-state systems where there are no nuclei to cross-polarise to, or potent sources of relaxation (e.g. paramagnetic impurities) long T_1 values (e.g. ^{29}Si in $Y_4Si_2O_7N_2$, T_1~ 2-3 hours) are encountered. Commonly paramagnetic impurities are added to shorten T_1 ($Y_4Si_2O_7N_2$ + 1mol%MnO_2, T_1~400s) since the consequences of adulterating the sample are believed to be acceptable. While this practice may be acceptable for homogeneous single-phase samples it is not for the inhomogeneous, multicomponent ceramics of this study as a uniform distribution of paramagnetic impurities is unlikely. Since the earliest pulsed FT NMR experiments[4] optimisation of conditions to improve S/N have been considered, although previous calculations[10,11] were not specifically concerned with the situation where the total duration of the experiment may be only a few T_1. These earlier calculations are not strictly valid in this limit as

they assume a constant magnetisation throughout the experiment. A new calculation of S/N in this regime will now be presented.

Consider a simple pulse sequence of equally spaced (T) strong RF, θ_p-pulses. The equation of motion of the longitudinal magnetisation between pulses is

$$\frac{dM_z}{dt} = \frac{M_0 - M_z(t)}{T_1} \qquad [3.2]$$

Where M_0 is the equilibrium magnetisation in the static applied field (B_0). After a pulse is applied (t=0) the longitudinal magnetisation develops as

$$M_z(t) = M_- \cos\theta_p \exp(-t/T_1) + M_0 [1-\exp(-t/T_1)] \qquad [3.3]$$

M_- is the longitudinal magnetisation immediately prior to the pulse. A second pulse is applied at t=T (t'=0) then

$$M_z(t') = A\cos\theta_p \exp(-t'/T_1) + M_0 [1-\exp(-t'/T_1)] \qquad [3.4]$$

Where $A = M_z(t=T)$ [Eq. 3.3]

Equations 3.3 and 3.4 allow the longitudinal magnetisation to be followed through a pulse experiment. The effect of a train of 30°-pulses is shown (Fig. 3.2(a), (b)) for different pulse spacings. The expected behaviour of progressive saturation of the magnetisation to an equilibrium value which depends on the pulse spacing and angle is clearly seen with a degree of saturation (~7%) even occurring for a pulse spacing of T_1. The number of pulses required to reach equilibrium agrees with a previous calculation[12] and may occupy a significant fraction of the total time of the experiment if T_1 is long. The previous S/N calculations[10,11] are strictly valid in the equilibrium region and will be a good approximation when the total

number of pulses is large compared to the number required to reach equilibrium.

As equations 3.3 and 3.4 express the magnetisation in terms of the magnetisation at the end of the previous interval the value of M_z immediately before each pulse may be calculated in terms of the initial state of the system. Then provided the transverse magnetisation decays rapidly compared to the pulse spacing the S/N for N_0 pulses may be written down as a discrete summation (Eq. 3.5).

$$\frac{S}{N} = \left(\sum_{n=1}^{N_0} M_z(nT)\right) \times \frac{\sin\theta_p}{\sqrt{N_0}} \qquad [3.5]$$

The S/N contours calculated from equation 3.5 as a function of pulse angle (θ_p) and spacing (T) (Fig. 3.2(c)) are similar in form to those calculated under the equilibrium assumption[11]. When the total experimental time is changed by a factor R the contours remain similar in form but they do not quite scale as $\sqrt{R}$, unlike the equilibrium contours. A "ridge" of optimum conditions can be seen which follow the well known Ernst angle condition[4]. Although optimum conditions can be chosen from anywhere along this ridge, sections through these contours show that for small pulse spacings these curves become sharply peaked (Fig. 3.2(d)) so that an accurate knowledge of the pulse angle is required to prevent significant loss of S/N. This suggests pulse angles (30°-70°) are best with the corresponding pulse spacings. It is important to emphasise that although chemical shifts may satisfactorily be obtained under these conditions, for multicomponent systems with different T_1's quantitative data has been lost.

Calculation of the S/N for a fixed 15 hour (overnight) experiment with different T_1's (Table 3.1) shows that for $T_1 \leq 1$ hour the S/N from an overnight accumulation is significantly better than

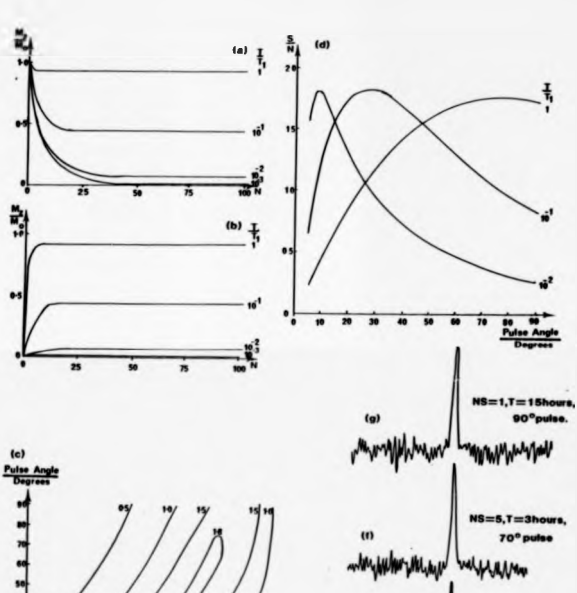

Figure3.2 The evolution of the longitudinal magnetisation as a function of pulse number,N,for different (f)pulse spacings with a train of 30° pulses,on samples initially(a)completely polarised,$M_z(0)=M_0$ and (b)unpolarised,$M_z(0)=0$.(c) The (S/N) contours for an experiment 7.5 T_1 long(1 unit=(S/N) from 1 90°-pulse with $M_z=M_0$). (d)Sections through (c) at constant T. (e)-(g)^{29}Si spectra from 15 hour experiments on $Y_4Si_2O_7N_2$($T_1\sim3$ hours) under various conditions. (NS=number of accumulations, all normalised to constant signal height).

from a single 90°-pulse. As T_1 increases this advantage decreases and with T_1>3 hours, even at optimum conditions this gain is barely significant. This is illustrated by the ^{29}Si spectra of $Y_4Si_2O_7N_2$ (Fig. 3.2(e)-(g)) with the optimum spectrum only slightly better than one 90°-pulse after 15 hours. For long, unknown T_1's the typical 60s pulse spacings, 15°-30° pulses used to accumulate ^{29}Si spectra from ceramics can lead to noticeably worse S/N ratios compared to those spectra obtained from one 90°-pulse applied to a fully relaxed system.

Pulse spacing	Pulse angle	Signal-to-Noise		
		T_1 = 1 hour	T_1 = 3 hours	T_1 = 4 hours
15h	90°	1.0	1.0	1.0
3h	70°	2.0	1.5*	1.3*
1h	45°	2.3	1.5*	1.2
60s	30°	1.7	0.6	0.4
60s	16°	2.5*	1.1	0.8
60s	5°	2.0	1.4*	1.2

(* - near optimum conditions)

Table 3.1 S/N values for variation conditions from a 15 hour "overnight" experiment calculated from Eq. 3.5.

This suggests a scheme for collecting spectra from such samples, as except for the single pulse at the end of the period the coil is superfluous. The samples need only to be held at high field and inserted just before the pulse. This could be repeated after several such periods to enhance the S/N. This has been implemented by developing a high-field sample changer (Fig. 3.3(d),(e)) which holds five double-bearing rotors (Fig. 3.3(a)) within the high field region (axial field, B_0>8.4T for ~9cm[13]). The design considerations have been to make it fit inside the magnet without any changes, be compatible with the commercial Bruker double-bearing probes and allow

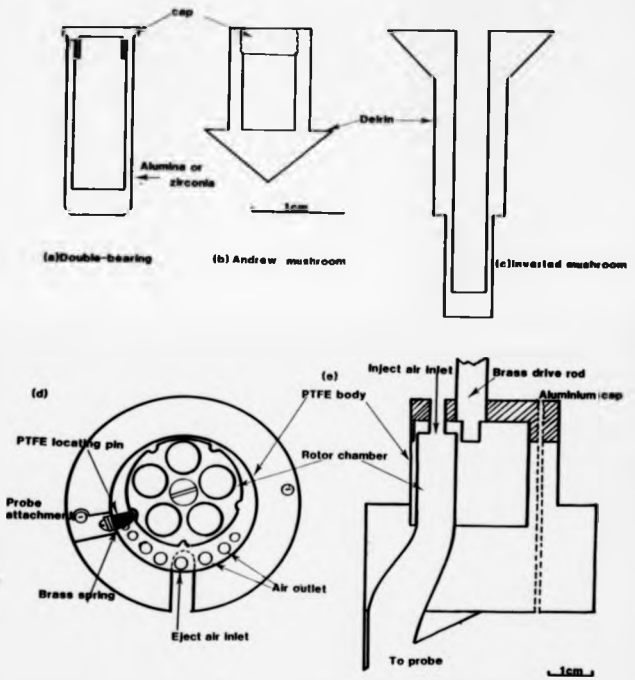

Figure3.3 (a)-(c)Rotors used for MAS experiments.(d)Plan and(e)section of the high-field double-bearing sample changer.

complete operation external to the magnet. The samples are rotated by a simple friction hand-drive on a brass rod which runs up the magnet bore with samples being manoeuvred in and out of the coil by compressed air. The samples are left polarising in high field overnight and then one pulse is collected from each of the samples in turn. The advantages of this scheme are clear in that the spectra become truly quantitative and the efficiency of the spectrometer is greatly improved.

3.3 The Bruker MSL-360 Spectrometer System

A commercial Bruker MSL-360 spectrometer was used to perform the NMR experiments so a brief description of the low frequency (4-156) MHz operation will be given with further details available in the Bruker reference manual[14]. The system is equipped with a widebore (available ~72mm) 8.45T Oxford Instruments superconducting cryomagnet. Field homogeneity achievable by optimisation of the shim coils gives linewidths of ~40Hz in our probes for protons in water with the field drift $\leq$20Hz per week. Simultaneous operations including data acquisition, data manipulation and plotting are allowed by the 7-level priority interrupt system of the Aspect-3000 computer. Normal spectrometer operation is performed by the DISMSL program which allows most parameters and processes to be controlled from the keyboard by short (usually 2 letter) instructions. The system process controller (SPC) of the computer is responsible for the operation of most of the hardware (Fig. 3.4) used in a pulse experiment which it controls by sending instructions via the RF interface. A highly structured language is used[15] which allows the operator to program the SPC to perform complex pulse sequences.

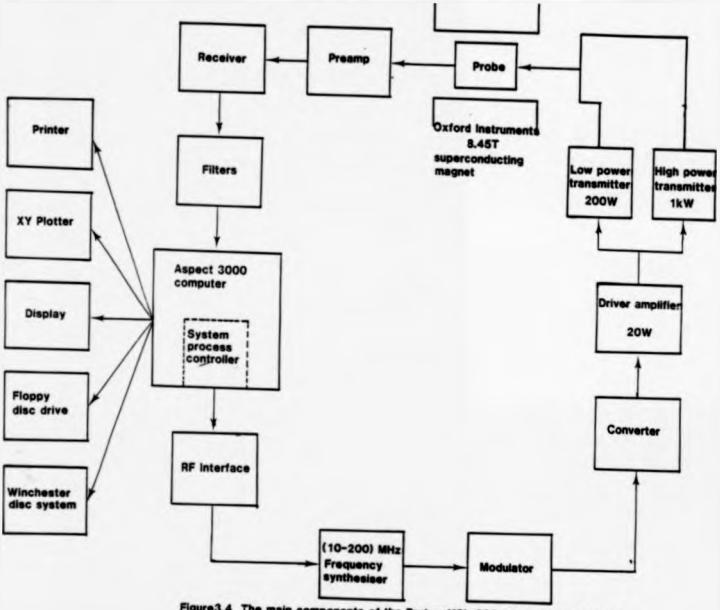

Figure3.4 The main components of the Bruker MSL-360 spectrometer system.

A PTS 200 synthesiser provides the low frequencies (1-200)MHz with 1Hz resolution. Pulses are provided by the SPC in conjunction with a four channel, fixed phase, broadband (10-200) MHz modulator. DC adjustment of the amplitude and phases of these pulses is possible but remain fixed within a pulse program's execution although there is an additional variable output modulator. The converter generates frequencies above 200 MHz while allowing the low frequencies to pass through unmodified. These pulses (~1V) pass through a broadbanded amplifier (15-25)W which acts as a driver of the two available transmitters, one being a low power (~200W) transmitter within the main console which is sufficient for liquid-state work and the other being a high power (~1kW) tunable transmitter. The pulses generated typically have rise times of 0.2μs with a minimum duration 0.5μs are fed to the probe. 40 or 60 dB amplification of the induced voltage from the coil occurs within the preamplifier which contains RF-filters and matching plug-in units that are changed for different frequency ranges. The extremely broadbanded (1-400)MHz receiver allows both single and quadrature PSD with phase and amplitude control of the receiver channels possible from the SPC, as is the level of the receiver gain. The detected signal passes via a Bessel-function filter to the computer for analog-to-digital conversion by one of the two available digitisers with the slower (12-bit) digitiser being replaced by a faster, lower resolution (9-bit) digitiser for dwell times ≤4μs. In quadrature detection the computer takes data points sequentially from each channel.

3.4 The NMR Probes

A range of commercial and homemade, static and spinning probes are available covering the frequencies (20-150)MHz allowing

multinuclear operation. The commercial probes include the Bruker double-bearing (DB) design which uses cylindrical spinners (Fig. 3.3(a)) made from alumina or zirconia and require careful sample packing to ensure spinning, with sample exchange performed whilst the probe is in the magnet. Probes using the conventional Andrew design have the drawback that they have to be removed from the magnet to change the sample but the ease with which these conventional Delrin "mushroom" spinners (Fig. 3.3(b)) spin compared to the cylindrical ones compensates for this. Initially a smooth conical air-bearing surface was used but it was found that the addition of flutes greatly enhanced the spinning speed (~3kHz → ~6kHz). A comparison of the relative sensitivities of these probes at 71.5MHz indicate that the double-bearing probe is ~20% more sensitive than the mushroom probe. A static probe using conventional plug-in horizontal solenoidal coils, with a much larger (~5cm^3) sample volume is also available. Details of these commercial Bruker probes may be found in their respective manuals[16].

The homemade probes have their spinning units based on the "inverted mushroom" design of Gay[17], intended for spinning sealed air-sensitive samples, which were adapted to use complete spinners (Fig. 3.3(c)). The main drawback of these probes is the low sensitivity due to the small filling-factor since the coil is on a former and the small sample volume which has been improved by a scaled-up (x2 diameter) version. The low frequency (20-50)MHz homemade probe uses a series-parallel probe circuit[8] with high voltage 30kV, (5-50)pF Jackson trimmer capacitors to allow the use of high power pulses on wide solid-state lines. Coil ringing was a problem at low frequencies (<40MHz) and this was reduced (~5μs, ν_o=26MHz) by using copper wire (23 SWG) rather than silver, together with mounting the coil in Araldite.

A dry, clean compressed air or nitrogen supply with a maximum pressure ~$6x10^5$Pa allows spinning up to 5kHz in all probes, which is monitored by an optical ratemeter. For the inverted mushroom spinners the maximum spinning speed depends critically on the sample chamber wall thickness since if they are too thin the Delrin deforms on spinning. This is evident in the enlarged probe as a dramatic reduction in the maximum spinning speed (3.5 → 2.1)kHz accompanies a decrease in the wall thickness (1 → 0.5) mm. All spinning probes have their coils nominally mounted at the magic angle to B_0 with a few degrees range of movement.

3.5 Operation of the Spectrometer

3.5.1 Setting up on a Nucleus.

Changing the spectrometer operation to different nuclei is a relatively trivial operation once the appropriate conditions for a nucleus have been determined and stored as a reference file on computer. Recall of this file initialises the RF-interface with the relevant parameters including the operating frequency (Table 3.2) and preamplifier selection. Hardware changes made by the operator include selection of the appropriate high power transmitter and preamplifier plug-in units, together with the probe. In this study operation from 10MHz to 55 MHz used an inverted mushroom probe while between 55MHz and 100MHz both a Bruker double-bearing probe and conventional Andrews probe, which was preferred, were available. The high power transmitter output is tuned by maximising its attenuated pulse output on an oscilloscope by adjusting a software-controlled stepper-motor driven variable capacitance from the console. The power level is set at the required value, determined by the probe and nucleus, with typically at higher frequencies B_1~5mT while at the lower frequencies B_1~8mT is used. Probe tuning is achieved by either examining the

probe circuit impedance characteristics or from the reflected power. The general technique adopted is to roughly tune on the impedance characteristics with fine tuning minimising the reflected power by adjustment of both the tune and match components of the circuit. Finally the preamplifier is tuned by adjustment of its capacitance to maximise the noise level on the FID.

After reading in the appropriate shim-file a solution-state spectrum is run since the inherent narrow line and short T_1 allows a large S/N to be rapidly accumulated. This provides the spectrometer reference which determines the zero of the chemical shift scale (Table 3.2) and as nearly identical conditions are used for these accumulations the S/N is a good indication of how satisfactory the spectrometer operation is. The 90°-pulse is usually determined once for a particular probe and power level. The receiver amplification has to be carefully selected so that no overload of the receiver occurs.

Nucleus	Operating frequency MHz (B_0 = 8.45T)	Chemical shift reference (=0ppm)
^{2}D	55.26	D_2O
^{14}N	26.00	Aqueous $Al(NO_3)_3$
^{25}Mg	22.06	Aqueous $MgSO_4$
^{27}Al	93.83	Aqueous $Al(NO_3)_3$
^{29}Si	71.54	TMS $(CH_3)_4Si$
^{45}Sc	87.46	0.1M aqueous $ScCl_3$
^{139}La	50.87	Dilute aqueous $La(NO_3)_3$

Table 3.2 Operating frequency and chemical shift references for nuclei in this study.

3.5.2 Setting the Magic Angle.

One of the most fundamental steps in obtaining high resolution solid-state NMR spectra is accurate setting of the magic angle. The coil is roughly orientated at the magic angle with fine adjustments by the quadrupole satellite technique[18]. This technique relies on materials containing quadrupole nuclei in nominally cubic environments being distorted by imperfections which quadrupole broaden the non-central transitions, resulting in only the ($\frac{1}{2} \leftrightarrow -\frac{1}{2}$) transition being readily observed. As the narrowing factor is $\frac{1}{8}(3\cos^2\beta-1)$ [Eq. 2.11] for a deviation of $d\beta$ the residual broadening factor is $3\cos\beta\sin\beta d\beta$ which at the magic angle is $\sqrt{2}\ d\beta$. This implies in a suitable material that first-order broadening should not be too severe, to allow the non-central transitions to be narrowed into a visible set of sidebands over a limited but not too restrictive range of angles about the magic value.

At higher frequencies the bromine resonance (90.2 or 97.2) MHz in cubic potassium bromide is ideal[18]. Spinning away from the magic angle means that only spinning sidebands of the ($\frac{1}{2} \leftrightarrow -\frac{1}{2}$) transition are prominent with extensive broadening of the higher order sidebands. As the magic angle is approached the higher order sidebands become very much sharper with eventually an extensive manifold of higher-order sidebands (at least 20 either side) with the consequent gain of sensitivity clearly demonstrated (Fig. 3.5(a)-(c)). In the time domain these sidebands are manifest as a train of sharp rotational echoes. The angle is adjusted by setting the spectrometer frequency close to the bromine resonance which makes the echoes readily observable and then maximising the number in the train (Fig. 3.5(d)).

At lower frequencies (<60MHz) various nuclei were investigated for their suitability for setting the angle. As nitrogen-14 (26.0MHz)

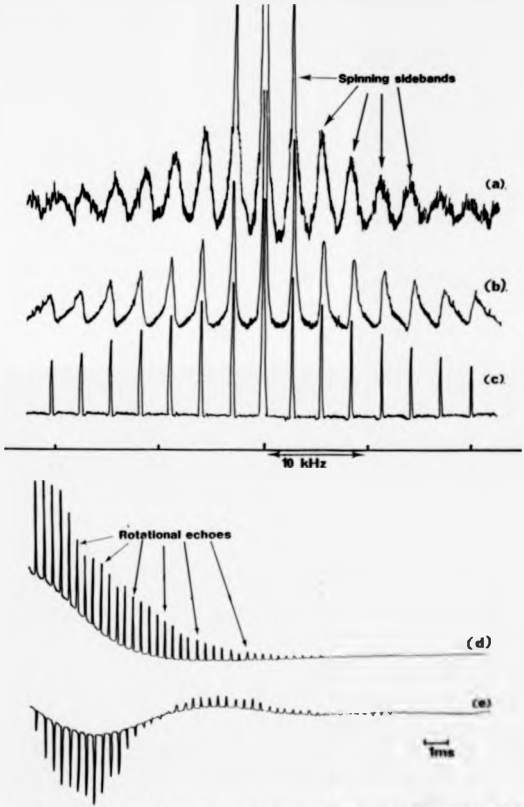

Figure3.5 Magic angle is set on bromine resonance of potassium bromide,with the spinning sidebands sharpening as the correct angle isapproached (a)→(c). (d) FID corresponding to(c). (e) Low frequency,angle set using ^{87}Rb resonance in rubidium chloride.

was of particular interest chlorine-37 (29.2MHz) and chlorine-35 (35.5MHz) were examined. These nuclei proved unsuitable since either only a few sidebands were visible (e.g. alkali halides) indicating the environments are too symmetric and not sensitive to angle or no resonance at all could be observed (e.g. $BaCl_2$). Rubidium-85 (34.7MHz) in RbCl was the most appropriate nucleus for setting the angle giving an extensive train of echoes (Fig. 3.5(e)) similar to KBr, although the experiment with RbCl is far more tedious than with KBr due to the lower sensitivity. For really accurate angle setting the deuterium resonance (55.3MHz) in deuterated polymethylmethacrylate (D-PMMA) was used with the resolution of the two inequivalent deuterium sites only possible when spinning close to the magic angle.

The reproducability of the spinning axis (decreasing double-bearing to inverted mushroom to conventional mushroom) between experiments is usually sufficient for efficient line-narrowing to require the angle only to be checked externally, periodically. It was anticipated for nitrogen-14 where very broad first-order quadrupolar broadened lines are encountered very accurate angle setting is required, so an internal check of RbCl was used.

3.5.3 Data Acquisition

For all data acquisition quadrature PSD was used. Simple pulse programs were employed, the most common being the single pulse phase-cycling CYCLOPS[19] sequence which removes quadrature detection artefacts, while at very long delays (>15 minutes) a constant phase one-pulse sequence was used. Short, intense ($<\pi/6$, (1-2)μs) pulses are used to reduce quadrupolar distortion and provide uniform spectral irradiation, together with sufficient delay between the pulses to prevent saturation, except for ^{29}Si spectra where conditions were

chosen to optimise S/N (Sec. 3.2). Preacquisition delays following the pulses were employed which protect the receiver as well as allowing ringing to decay. These delays (~5μs) were chosen as a compromise between introducing phase and intensity errors and minimising ringing effects[9]. For high resolution solid-state lines typically 2K data points are accumulated with a suitable dwell time which allows sufficient definition of the peak for accurate determination of the chemical shift, while providing enough baseline on which to judge any distortion, yet not covering too wide a frequency range to significantly degrade the S/N.

For static spectra of quadrupolar nuclei a quadrupole echo sequence [$(\pi/2)_{\pm x} - \tau - (\pi/2)_{y} - \tau'(Ac)$] was employed to overcome the ringing effects which are a problem for some broadline static spectra. Although high power levels were used, to further improve spectral irradiation a simple, but not the best[20], composite pulse sequence was used[21] (e.g. Fig. 3.6(a), $135^{\circ}_{x}90^{\circ}_{\bar{x}}45^{\circ}_{x}$ composite 90°_{x} pulses).

Some T_1 estimates were obtained for some of the crystalline oxynitride phases by using the saturation-recovery method which is best suited to the large T_1 values encountered.[8].

3.5.4 Data Manipulation

Once the FID has been accumulated it is usually processed to give a conventional absorption spectrum to allow interpretation. Sophisticated software allows rapid manipulations including Fourier transformation, resolution enhancement, spectral smoothing, phasing and baseline correction. Great caution has to be exercised with this processing to ensure that the final spectrum produced is an accurate reflection of the time domain signal.

A typical set of manipulations (Fig. 3.6(b)) would be to employ some smoothing (termed linebroadening) to improve the S/N by multiplying the FID by a weighting function which enhances the signal at short times[8]. If the lineshapes are Lorentzian (FWHM=(α/π)Hz) and βHz of exponential broadening is applied, the time domain signal is simply the product of two exponentials

$$f(t) = A\exp(-\alpha t) \times \exp(-\beta t) \qquad [3.6]$$

The spectrum thus becomes a convolution of the two frequency domain functions

$$F(\omega) = \frac{A}{(\alpha+\beta)} \quad \frac{1}{1+\frac{(\omega-\omega_0)^2}{(\alpha+\beta)^2}} \qquad [3.7]$$

The exponential smoothing increases the linewidth (FWHM) to $(\alpha+\beta)/\pi$ Hz. Injudicial use of smoothing has lead to incorrect data interpretation[22], so if S/N allowed zero linebroadening was used. Time domain data is Fourier transformed to give the frequency domain data which has to undergo zero-order and first-order phase correction which essentially involves mixing contributions from the two quadrature channels to produce a pure absorption spectrum. Phasing is usually carried out by eye, judged on factors such as peak symmetry and baseline regularity, so it is somewhat subjective. Particular care has to be taken with broad lines encountered in glasses and with quadrupole nuclei, when baseline roll produced by probe ringing can severely distort the lineshape. For narrow lines software algorithms can readily remove the baseline errors or the first few time domain points associated with the ringing may be removed prior to FT, although this can make it difficult to phase complex spinning sideband manifolds.

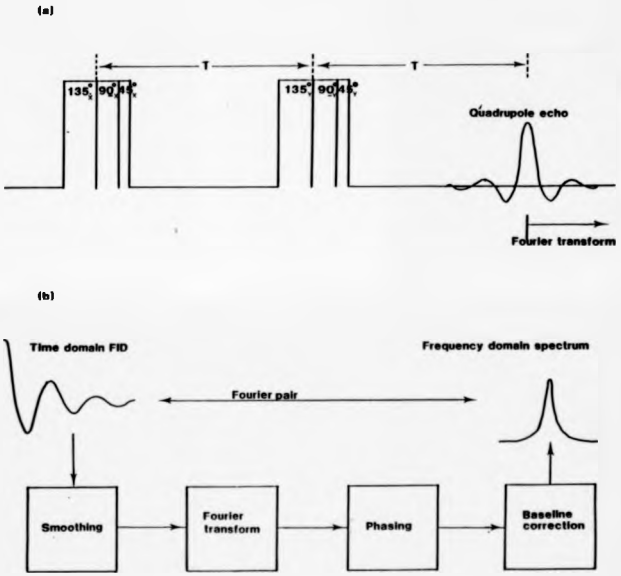

Figure3.6 (a) Composite quadrupole echo sequence used for static spectra of broad quadrupole lines.(b)Typical data processing procedure.

Alternatively FT of a spinning sample may be performed from a rotational echo maximum and this removes ringing problems, with the other processing remaining the same. For quadrupole echo sequences the same procedure may be followed with the zero of the time domain is shifted to the echo maximum (Fig. 3.6(a)).

3.6 Sample Preparation

3.6.1 Introduction to Solid-State Ceramic Reactions

Crystalline ceramics are prepared by sintering of particulate compacts to form densified solid phases. Densification and reactivity of powder compacts are enhanced by using fine (~1μm) powders since the reduction of surface free energy is an important driving force. More complete reaction is ensured by intimate and uniform mixing which is exemplified by the low temperature (~1000°C) preparation of yttrium aluminate phases by calcining mixtures of nitrates and sulphates formed by precipitation from solution. As the solid-state reactions proceed, material is transported to the points of contact at the particle surfaces together with interdiffusion of the materials which increases rapidly as the melting points of the phases (Fig. 1.2) are approached, so that high temperatures (1600-1800)°C are usually employed. Increased reactivity at lower temperatures can be greatly encouraged by the presence of small amounts of liquid phases in which the other materials have some solubility (e.g. Y_2O_3+SiO_2 compounds play this role in the sintering of Si_3N_4), which is termed reactive liquid sintering. At high temperatures loss of volatile components (e.g. Eq. 3.8) or atmospheric contamination (e.g. oxidation of oxynitrides) can readily occur resulting in compositional changes.

$$SiO_2 \rightarrow SiO_{(g)} + \tfrac{1}{2} O_{2(g)} \qquad [3.8]$$

The reaction kinetics in the solid-state can be ponderous, even at elevated temperatures, so there exists the possibility that the

final phase distribution may not be the true equilibrium configuration. The assumption is also made that the rates of cooling applied result in the high temperature phase distribution being preserved in the samples at room temperature. For more detail about solid-state ceramic reactions the reader is referred to the literature[23].

3.6.2 High Temperature Sintering Furnace

Production of the high temperatures necessary for extensive and rapid phase formation is an essential part of sample manufacture. A simple vertical tube RF-induction furnace was employed (Fig. 3.7). The RF current in the copper coil creates a magnetic field which electromagnetically induces eddy currents in the graphite susceptor causing resistive heating. The basic requirements for this furnace are the ability to reach high temperatures (~1700°C) in a short period of time (~1 hour), hold these temperatures stably (=~±5°C) with many repetitions between overhauls. The design chooses simplicity, allowing rapid exchange of worn out parts, over the complexity necessary for more rigorous oxygen exclusion. Typical susceptor lifetimes are extended to around 30 sinterings by the use of an inert argon atmosphere. The temperature is monitored by two thermocouples with a tungsten/(tungsten -26% rhenium) control thermocouple in the centre of the susceptor and a check platinum/(platinum-13% rhodium) thermocouple in the sample chamber. The tungsten thermocouple provides a sufficiently large and rapidly varying emf at elevated temperatures to allow control of the furnace although it is far from ideal due to its severe embrittlement on oxidation, thereafter being very fragile and susceptible to irreparable damage. The Radyne 174B RF power supply is controlled by a proportional-integral-derivative

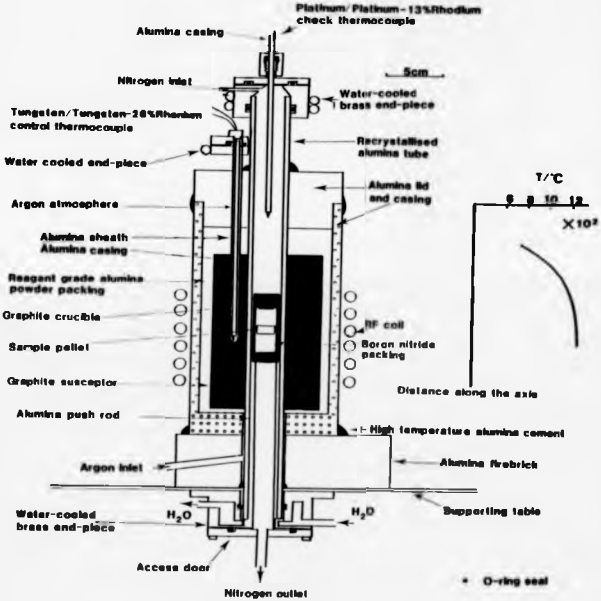

Figure3.7 High temperature RF sintering furnace and the axial temperature gradient when 1250°C is set on the controller,on the same scale ,showing the length and position of the hot zone.

feedback controller which monitors the emf of the tungsten thermocouple. The central sample volume has a flowing overpressure of oxygen-free nitrogen and a 5cm (at 1400°C) hot zone. Periodically lower temperature (1200-1400)°C "dummy" runs were performed to measure the axial temperature gradient with the platinum thermocouple which checks the temperature, length and position of the hot zone. The furnace is allowed to cool by simply turning the power off which results in initial cooling rates of ~100°C/min.

3.6.3 Sample Manufacture

Stoichiometric mixtures of the appropriate high purity powders (nominally $\geq$99.9%;Si_3N_4:SiO_2,Al_2O_3,AlN,Y_2O_3,La_2O_3,Sc_2O_3,YN,LaN) are weighed out and if possible different starting components for the same product are used, since if the final state corresponds to equilibrium it should be independent of the starting point. The nitrides tend to form an oxide surface coating so that compositions are more oxygen-rich than expected. Either dry ball-milling (~24 hours) or hand grinding in a pestle and mortar is used to mix the powders, of which the latter is preferred since there was no apparent difference in reactivity and contamination from the balls is avoided. The powder mixture is compacted by applying a uniaxial pressure (~$5x10^8$Pa) in a steel die, which improves particle contact and allows ready handling, to form (1-3)g disc-like pellets of dimension ~1.5cm diameter by ~0.5cm high. The pellets are embeddad in high purity, inert BN powder in a graphite crucible. The sample is heated in the high temperature sintering furnace where it remains for the whole heating cycle, being at temperature (~1700°C) for about 2 hours, under an oxygen-free nitrogen atmosphere at all times. Both before and after sintering a pellet's mass is measured, to check that no significant volatilisation of any component has occurred. The fired pellets are usually

extremely hard and care has to be taken in powdering them to prevent contamination by similar materials, hence aluminates were ground in an agate pestle and mortar while oxynitrides were ground in an alumina set. The same procedure is applied to all samples except those made from La_2O_3 and the Group 3B nitrides which are stored under a dry nitrogen atmosphere prior to heating. Group 3B nitrides react rapidly with moisture, evolving ammonia, so all processing except pellet formation is carried out under a dry nitrogen atmosphere. Oxidation and annealing is performed in a horizontal alumina tube resistance furnace. Some materials (eg. Y_2SiAlO_5N) which are unstable at high temperatures were alternatively manufactured by crystallisation of nearby glass-forming compositions[24].

An alternative lower temperature manufacture of yttrium aluminates from the thermal decomposition of mixtures of either $Al(NO_3)_3.9H_2O$ or $NH_4Al(SO_4)_2.12H_2O$ and $Y(NO_3)_3.9H_2O$[25,26], made up so that the Y:Al ratio is correct for the final product, was also employed. The two salts are mixed together with a small amount of distilled water to form a saturated solution which is heated by a Bunsen burner in a pyrex beaker. The water boils off redepositing an intimate mixture of the salts which thermally decompose giving off gaseous products (eg. HNO_3, SO_2, NH_4, NO_2). The resulting solid is reground and reheated (~400°C) until no further reaction is observed, finally being transferred to an alumina boat to crystallise at (800-1200)°C for ~30 hours in the resistance furnace.

3.6.4 Sample Characterisation

Although single phase specimens are desirable, with these complex systems multiphase products often result. To identify the phases, along with their distribution, X-ray diffraction (XRD) and scanning electron microscopy (SEM) were performed which allows

comparison of the ability of these techniques and MAS-NMR to characterise these materials. For multicomponent systems the heat treatment and composition are varied to change the phase distribution which may be correlated to changes of intensity in the complex XRD patterns and NMR spectra aiding interpretation.

XRD powder patterns from a Philips 7070 scanning powder diffractometer provide the primary source of phase identification. The powder patterns were taken using CuKα radiation (30mA, 40kV, λ=1.5478Å) between 10° and 60° (2θ), at a scanning rate of 1°(2θ) per minute.

Small fragments of ceramic with faces 5mm by 5mm were analysed in a Cambridge Instruments S250 scanning electron microscope. Conventional preparative procedures were used by mounting the specimens in a Bakelite mould and polishing the upper surface to ~0.5μm smoothness using a series of abrasive papers followed by abrasive diamond paste on a cloth wheel. A very thin sputtered layer of carbon was deposited to prevent surface charging of these insulating ceramics which severely degrades the technique. Microstructural detail (e.g. porosity, topography) can be examined from the direct image, with backscattered secondary electron emission giving Z(atomic number) contrast, providing information about the phase distribution. By energy dispersive X-ray analysis using the microprobe EDAX facility available on the system it is possible to find the approximate chemical composition, in particular the Ln:Si:Al ratio, of the phases present.

References: Chapter 3

1. Hahn, E.L., Phys. Rev. 80, 1950, 580-594.
2. Lowe, I.J. and Norberg, R.E., Phys. Rev. 107, 1957, 46-51.
3. Clark, W.G., Rev. Sci. Inst. 35, 1964, 316-330.
4. Ernst, R.R. and Anderson, W.A., Rev. Sci. Inst. 37, 1966, 93-102.
5. Cooley, J.W. and Tukey, J.W. Math. Comput. 19, 1965, 297-301.
6. Lowe, I.J. and Tarr, C.E., J. Phys. E., 1, 1968, 320-322.
7. Abragam, A., 'Principles of Nuclear Magnetism', OUP, 1961.
8. Fukushima, E. and Roeder, S.B.W., 'Experimental Pulse NMR', Addison-Wesley 1981.
9. Hoult, D.I., Chen, C.-N., Eden, H. and Eden, M., J. Magn. Reson. 51, 1983, 110-117.
10. Waugh, J.S., J. Mol. Spec. 35, 1970, 298-303.
11. Christensen, K.A., Grant, D.M., Shulman, E.M. and Walling, C., J. Phys. Chem., 78, 1974, 1971-1977.
12. Homer, J. and Reavers, M.S., J. Magn. Reson. 63, 1985, 287-297.
13. Oxford Instruments figures.
14. 'MSL System Description' Bruker Manual, Ref. No. 431001, 1986.
15. 'Aspect 3000 MSL Software Manual', Bruker Manual, 1986, Chapter 16.
16. 'NMR Probehead, Series MAS-DB', Bruker Manual, 1985.
17. Gay, I.D., J. Mag. Res. 58, 1984, 413-420.
18. Frye, J.S. and Maciel, G.E., J. Mag. Res. 48, 1982, 125-131.
19. Hoult, D.I. and Richards, R.E., Proc. R. Soc. Lond. A., 344, 1975, 311-340.
20. Siminovitch, D.J., Raleigh, D.P., Olejniczak, E.T. and Griffin, R.G., J. Chem. Phys., 84, 1986, 2556-2565.
21. Levitt, M.H., Prog. NMR Spec. 18, 1986, 61-122.
22. Gladden, L.F., Carpenter, T.A., Elinowski, J. and Elliott, S.R., J. Magn. Reson. 66, 1986, 93-104.
23. Kingery, W.D., Bowen, H.K and Uhlmann, D.R., 'Introduction to Ceramics' (2nd edition) J. Wiley and Son, 1976.
24. Thompson, D.P., in 'Tailoring Multiphase and Composite Ceramics' p(79-91), Ed. Tressler, Messing, Pantano and Newnham, Plenum, 1986.
25. Bertaut, E.F and Mareschal, J., Comp. Rend. Acad. Sci. Paris, C., 257, 1963, 867-870.
26. Messier, D.R. and Gazza, G.E., Bull. Am. Ceram. Soc. 62, 1979, 476-479.

CHAPTER 4. SILICON-29 NMR

4.1 Introduction to Trends of the ^{29}Si Chemical Shift in the Solid-State

The large variety of inorganic materials containing Si-O bonds studied by high resolution ^{29}Si NMR (Sec. 1.3) has led to the compilation of an extensive catalogue of their isotropic chemical shifts. To enhance the utility of ^{29}Si NMR for structure determination, correlations between various structural parameters and the isotropic chemical shift have been attempted. It is accepted that changes of the paramagnetic shielding term dominate and these may be related to the covalency of the bond. Semi-empirical rules have been formulated to explain the general trends of the isotropic chemical shift as there is no direct calculation of the isotropic shift which embraces the effect of all structural influences on bond hybridisation.

The most important feature influencing the chemical shift is the local silicon coordination, such that for inorganic materials tetrahedral units (SiO_4) resonate between -60ppm and -130ppm (w.r.t. TMS)[1] and the much rarer octahedral units (SiO_6) resonate between -180ppm and -220ppm[2]. The increased coordination decreases the electrostatic bond strength S (=Σ(charge)/ν(coordination)), which decreases the covalency of the bond[3] and hence the paramagnetic shielding, moving the resonances to more negative chemical shifts[4]. Extensive overlap of the resonance positions of differently connected SiO_4 tetrahedra (termed Q-types, where Q^n designates an SiO_xN_{4-x} tetrahedron connected to n other tetrahedra) occurs due to the many influences on the chemical shift. Once materials with aluminium next nearest neighbours (nnn) have been excluded, this overlap decreases (Fig. 4.1(a)). The isotropic chemical shift clearly becomes more positive as n decreases. As the number of non-bridging oxygens (i.e.

an oxygen that is not bonded to a network-forming element] in the SiO_4 unit increase the cation-oxygen electrostatic bond strength associated with the unit decreases and hence the average covalency of the Si-O bonds within the unit increases causing a paramagnetic shift. The effect of differing nnn tetrahedra on the chemical shift has been observed for both framework and sheet silicates where replacement of silicon by aluminium causes a shift of ~+5ppm (Fig. 4.1(a)]. In glasses the shift of a particular tetrahedron has been observed to be sensitive to the nature (i.e. Q-type) of its neighbouring silicon tetrahedra[5].

Structural parameters which have been correlated with the isotropic chemical shift include bond length[6], bond angle[7], electrostatic bond strength[8] and group electronegativity[9] (Fig. 4.1(b)]. As the Si-O bond length decreases the s-electron character of the bond increases[6,10] resulting in the shifts becoming more negative, with a change in the average bond length of 0.0001nm causing a change in the shift of ~1ppm[6]. The bond length correlation is one of the poorest (Fig. 4.1(b)], reflecting the average bond length is not a good measure of the overall nature of the bonding. Bond angle changes can profoundly effect the chemical shift, with the degree of s-hybridisation of the bond ρ[4] [Eq. 4.1] being largest for a bond angle (α) of 180°.

$$\rho = \frac{\cos\alpha}{\cos\alpha - 1} = f(\alpha) \qquad [4.1]$$

This effect is shown by Q^1 units, as those with bridging bond angles (α=Si-O-Si] of 180° are shifted to more negative values compared to those units with smaller bridging bond angles. The Q^4 units in the polymorphs of silica, α-quartz (α = 143.7°) δ = -107.4ppm and α-cristobalite (α = 146.4°], δ = -109.0ppm, also follow this trend[7]. Zunyite contains the most negatively shifted Q^4

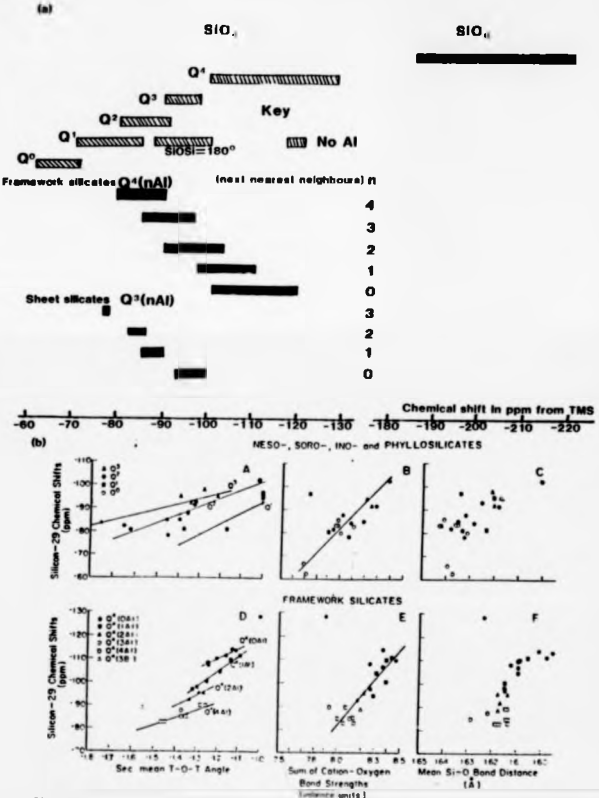

Figure 4.1 Silicon-29 NMR of inorganic materials containing Si-O bonds with (a) shift ranges and (b) correlations of the isotropic shift to structural parameters (taken from [1]).

unit, δ_{Si} = -128ppm, due to the Q^4 unit being connected to the surrounding Q^1 units via bonds with α=180°[11]. A number of angular functions have been used for correlations to the bond angle including α[12], $f(\alpha)$[6] and $\sec\alpha$[13]. $\sec\alpha$ appears to be the best and has the most physical basis (Sec. 1.2), although over the region of interest these angular functions have similar curvatures so that it is difficult to choose between them[7].

The best overall correlation is probably with the electrostatic bond strength which gives a measure of the covalency of the cation-oxygen bond and hence indirectly of the Si-O bond. The polymorphs of Ca_2SiO_4 show a more negative shift of the ^{29}Si resonance as the electrostatic bond strength associated with the cation increases, with α(-70.3ppm (isotropic shift); 8,10,12 (Ca coordination)), β(-71.4ppm; 8,10) and γ(-73.5ppm, 6)[4]. A semi-empirical group electronegativity approach[9] also appears to be potentially useful since it takes into account the nnn and also crudely builds in a bond angle variation by scaling the group electronegativity associated with -OSi fragments by a factor that depends on α.

The isotropic chemical shift is sensitive to relatively small changes in the local environment, so only crystalline materials with accurately defined structures should be used for these correlations. The greatest potential benefit for using these correlations with MAS-NMR spectra are for materials where other techniques provide little structural information (e.g. glasses). The same trends of the isotropic chemical shift are followed by glasses which has been demonstrated by binary soda-silicate glasses with the expected displacement of the chemical shifts of Q^4, Q^3 and Q^2 units relative to one another[14].

The isotropic chemical shift provides information about the average shielding while the chemical shift anisotropy and asymmetry (Sec. 1.2) provide information about the directional variation of the shielding. As the principal elements of more silicate shift tensors have been determined, correlation of the individual bond lengths to specific tensor components has been attempted[10].

Silicon oxynitride materials with their variation of the local silicon nearest neighbour (nn) coordination tetrahedron SiO_xN_{4-x} ($0 \leq x \leq 4$) allows the range of structural parameters to be further expanded. Hence the applicability of the various correlations can be examined and it can then be seen how readily the effects of nitrogen can be built into the general scheme.

4.2 The Y-Si-Al-O-N System

4.2.1 Y_2O_3-SiO_2 System.

The Y_2O_3-SiO_2 system has been the subject of a number of studies[15,16] which have confirmed the existence of two silicates, a metasilicate (Y_2SiO_5) consisting of isolated SiO_4 tetrahedra and a disilicate ($Y_2Si_2O_7$) which is made up of units of two SiO_4 tetrahedra joined by a bridging oxygen to form an Si_2O_7 unit. These silicates exhibit extensive polymorphism with Y_2SiO_5 having two known polymorphs while $Y_2Si_2O_7$ has at least four, with transition temperatures

$$\alpha \xrightarrow{1225^\circ C} \beta \xrightarrow{1445^\circ C} \gamma \xrightarrow{1535^\circ C} \delta \qquad [4.2]$$

The existence of a silicate phase intermediate to the 1:1(SiO_2:Y_2O_3) and 2:1 compositions is disputed, with a range of compositions from $Y_{4.67}(SiO_4)_3O$ to $Y_4(SiO_4)_3$ possible, depending on the nature of the defect structure assumed[16]. This silicate is

supposed to be an extension of the N-apatite solid-solution ($Y_5(SiO_3N)_3\Phi$(Φ=vacancy) - $Y_5Si_3O_{12}N$) to the pure silicate composition line. To satisfy Pauling's Second Crystal Rule (PSCR) (which states, using Pauling's words, "In a stable ionic structure the valence of each anion, with sign changed, is exactly or nearly equal to the sum of the strengths of the electrostatic bonds to it from adjacent cations")[3] in N-apatite the nitrogen bonds directly to silicon rather than replace the fluorine of the isostructural mineral apatite ($Ca_5(PO_4)_3F$).

A 1:1 mixture of Y_2O_3 and SiO_2 sintered at 1700°C for 2 hours shows almost complete reaction with single phase Y_2SiO_5 being produced according to XRD. The MAS-NMR spectrum shows a single resonance at -79.8ppm (Fig. 4.2(a)). High temperature δ-$Y_2Si_2O_7$ formed by direct sintering of the oxides at 1700°C gives a spectrum which shows a clearly resolved splitting of the resonance at -81.2ppm and -82.8ppm (Fig. 4.2(e)). γ-$Y_2Si_2O_7$ formed by annealing δ-$Y_2Si_2O_7$ at 1250°C for ten days under an oxygen atmosphere. Although α-$Y_2Si_2O_7$ and β-$Y_2Si_2O_7$ may be similarly formed by annealing the higher temperature polymorphs at the appropriate temperatures, the reaction kinetics become extremely sluggish and a more rapid preparative route is to take nearby yttrium silicon oxynitride glass-forming compositions and crystallise them under an oxygen atmosphere. (α-1000°C, 15 days; β-1100°C, 15 days). The preferential formation of these polymorphs has been observed in the crystallisation of low nitrogen content YSIALON, glasses.[17] All the products are almost single phase according to XRD and SEM analysis, with any minor impurities being residual glass and SiO_2. γ-, β- and α-$Y_2Si_2O_7$ all have single MAS-NMR peaks γ(-92.8ppm), β(-93.6ppm) and α(-83.4ppm) (Fig. 4.2(d),(c),(b)), with the β-$Y_2Si_2O_7$ spectrum also showing some SiO_2 at -111ppm. The resonance of α-$Y_2Si_2O_7$ is considerably broader (FWHM-350Hz) than the

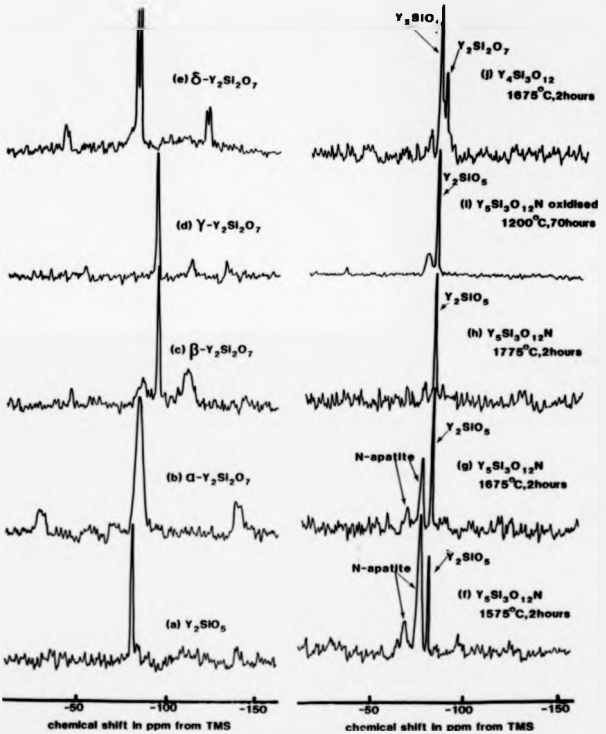

Figure4.2 Silicon-29 spectra from (a)-(e) yttrium silicates and(f)-(j) apatite compositions.

other polymorphs (FWHM~70Hz). Spinning sidebands are also present in these spectra and their intensities indicate the chemical shift anisotropy is considerably greater for α and δ polymorphs compared to β and γ polymorphs.

All yttrium N-apatite compositions sintered at various temperatures (Fig. 4.2(f)-(j)) are multiphase in nature with XRD indicating appreciable amounts of $Y_5Si_3O_{12}N$ and Y_2SiO_5 together with minor levels of $Y_4Si_2O_7N_2$ and Y_2O_3. MAS-NMR confirms the presence of Y_2SiO_5 (~79.9ppm) which leaves two peaks at -67.6ppm and -74.8ppm that are assigned to N-apatite. As the heat treatment is increased more Y_2SiO_5 forms until at 1775°C only the Y_2SiO_5 peak is prominent, in agreement with XRD. This sample shows measureable weight loss and volatilisation of nitrogen may have occurred. The intensities of the peaks at -67.6ppm and -74.8ppm change relative to the Y_2SiO_5 peak, in agreement with the phase content of the sample, while remaining at approximately the same intensity relative to one another, confirming their assignment to N-apatite.

Attempts to manufacture the intermediate silicate by direct sintering of the oxides at 1675°C yielded mixtures of Y_2SiO_5 and δ-$Y_2Si_2O_7$ (Fig. 4.2(j)) while oxidation of an N-apatite rich sample yielded Y_2SiO_5 as the major phase with some residual N-apatite (Fig. 4.2(i)). These results confirm that a pure oxide apatite does not form in the yttrium system.

Y_2SiO_5 provides a useful standard since the SiO_4 tetrahedron has only -OY groups attached, allowing the OY group electronegativity to be deduced by applying equation (1) of reference 9. This gives EN(OY)=3.69, which fits into their scale considering the electronegativity of yttrium relative to the electronegativities of the other elements[9]. Grimmer's bond length correlation[6] applied to Y_2SiO_5, with an average Si-O bond length of 0.163nm[18], gives an

isotropic chemical shift of -79.2ppm. Agreement is quite good but the shifts obtained from these correlations should only be treated as first-order approximations.

The polymorphism of $Y_2Si_2O_7$ allows the influence of structural effects on the isotropic chemical shift to be carefully analysed since compositional variation is removed. The only previous NMR measurements on this system have been for monoclinic γ-$Y_2Si_2O_7$ (-92.9ppm) and orthorhombic δ-$Y_2Si_2O_7$ (-81.6ppm, -83.5ppm) with the 1:1 doublet only being poorly resolved[19], unlike figure 4.2(b). The local structures of most of these polymorphs are only poorly known since the crystal-type is deduced by fitting the XRD pattern to a known disilicate structure, with no individual single crystal structure determinations. In δ-$Y_2Si_2O_7$ the source of inequivalence at the silicon site is the average bond length of the two SiO_4 tetrahedra in the $Si_2O_7^{6-}$ unit differ ($\Delta d(Si-O) \sim 0.001nm$)[20]. The group electronegativity model[9] would not distinguish these units, while the bond length correlations, based on the XRD bond length data, estimates a splitting of ~10ppm, which suggests the XRD data is not accurate. The major difference between δ and γ/β polymorphs is the change in the bridging bond angle (Si-O-Si) $\delta(\alpha = 158.7°)$ and $\gamma/\beta(\alpha = 180°)$, with the expected negative shift as the bond angle increases, in accordance with the various angular correlations (Sec. 4.1), although their predictions for the change of shift corresponding to this angular change differ widely from 3.3ppm to 13.2ppm. γ-$Y_2Si_2O_7$ and β-$Y_2Si_2O_7$ are both monoclinic, with highly regular tetrahedra. This explains the decreased chemical shift anisotropy (from the sideband amplitude) for γ and β relative to α and δ. The small shift difference between γ and β is due to slightly different arrangements of neighbouring $Si_2O_7^{6-}$ groups and YO_6 octahedra. α-$Y_2Si_2O_7$ has been indexed on a triclinic unit cell although a single crystal

determination of the local structure has not been performed[20]. If the local structure is analogous to α-$Ho_2Si_2O_7$, as believed, then Q^0, Q^1 and Q^2 units would be expected as the α-form is unusual in that it is composed of SiO_4 and Si_3O_{10} units rather than Si_2O_7 groups. The increased linewidth of α-$Y_2Si_2O_7$ compared to the other polymorphs indicate a range of distorted Q^1 environments are likely rather than there being distinct Q-types, although neither possibility can be conclusively proved from the spectra. Polymorphic transformation of α-$Ho_2Si_2O_7$ occurs to a form consisting of Q^1 units, so α-$Y_2Si_2O_7$ could have Si_2O_7 units with a bridging bond angle close to the δ-polymorph. Application of the group electronegativity approach to $Y_2Si_2O_7$ (α=169°) gives an average ^{29}Si shift of ~-92ppm. This demonstrates that such an approach can explain general trends, such as the negative shift of Q^1 ($Y_2Si_2O_7$) relative to Q^0 (Y_2SiO_5), but not accurately predict chemical shifts.

The two resonances from yttrium N-apatite can be assigned to Q^0 SiO_3N (-67.6ppm) and SiO_4(-74.8ppm) tetrahedra, although the peak area ratio is larger than the expected 2:1 (SiO_4:SiO_3N) for a stoichiometry $Y_8Si_3O_{12}N$. However, the assignment and stoichiometry remain uncertain due to the multicomponent nature of all the yttrium N-apatite samples that have been prepared in this study. The peak at -74.8ppm is close to the N-YAM (4.2.2) position, but it is appreciably narrower (Table 4.1) than N-YAM and XRD shows N-YAM to be a minor phase. A truly multinuclear approach (e.g. ^{89}Y) would confirm this assignment, since it is unlikely that both ^{29}Si and ^{89}Y would both have coincident shifts in different materials. The shift of the Q^0, SiO_4 resonance in $Y_8Si_3O_{12}N$ relative to Y_2SiO_5 is due to the increase in the yttrium coordination from N-apatite (6,7) to Y_2SiO_5(6). This decreases the Y-O electrostatic bond strength in N-apatite, increasing the covalency of the Si-O bond causing a paramagnetic shift.

Considering the phase equilibria the increase in the amount Y_2SiO_5 with increasing temperature above 1650°C shows that N-apatite becomes unstable with respect to Y_2SiO_5. The inability to form a pure silicate around the apatite composition indicates that nitrogen plays an important role in stabilising the yttrium N-apatite composition.

4.2.2 Sialons and the 2M:3X Plane

Hexagonal Si_3N_4 is a completely connected framework of SiN_4 tetrahedra with each nitrogen atom common to three tetrahedra in trigonal planar arrangements which are stacked parallel to the basal plane of the hexagonal unit cell. Two polymorphs have had their structures completely determined by XRD, differing in the stacking sequence along the c-axis, being (ABCD) for α-Si_3N_4 and (ABAB) for β-Si_3N_4[21]. The β'-sialon solid-solution is an isostructural modification of β-Si_3N_4 with a general formula $Si_{3-x}Al_xO_xN_{4-x}$ ($x \leq 2.1$)[22] (Sec. 1.4). The metastable β"-sialon also has the same crystal structure but with magnesium as well as aluminium substitution and is much enriched in oxygen ($Mg_yAl_{4-y}Si_2O_{4+y}N_{4-y}$)[23]. Similarly α'-structures are based on the $Si_{12}N_{16}$ unit cell of α-Si_3N_4 with the general formula $M_xSi_{12-(m+n)}Al_{m+n}O_nN_{16-n}$ as m(Al-N) bonds and n(Al-O) bonds replace (m+n)(Si-N) bonds, with the more open structure able to accommodate statistically x large metal ions (e.g. Ca^{2+}, Y^{3+}) in the two large interstices per unit cell[22]. Towards the AlN-rich corner of the Si-Al-O-N system (Fig. 1.2) a series of polytypoid phases exist ($Si_{6-u}Al_{u+v}O_uN_{8-v-u}$) which are identified by the metal (M) to non-metal (X) ratio, M_AX_{A+1}[22]. The crystal structures of the polytypoids are based on wurtzite but are modified to incooperate AlO_6 octahedral layers which replace every Ath layer of tetrahedra in the stacking sequence along the c-axis.

In the 2M:3X plane (Fig. 1.2) Si_2N_2O is a useful reference compound as its crystal structure has been fully determined, consisting of fully-connected $SiON_3$ tetrahedra (i.e. Q^3)[24]. Yttrium N-wollastonite ($YSiO_2N$) is known to consist of rings of 3 SiO_2N_2 tetrahedra with nitrogen in the bridging position and these rings are stacked along the c-axis[25]. A metastable phase, Y_2SiAlO_5N forms which is similarly composed of rings $(Si,Al)_3(O,N)_9$ but the local atomic arrangement within these rings is unknown. This compound shows only limited compositional variation and decomposes above 1200°C. N-YAM($Y_4Si_2O_7N_2$)-YAM($Y_4Al_2O_9$) forms a complete solid solution with XRD showing a smooth decrease in the cell volume with increasing silicon content. The crystal structure of $Y_4Al_2O_9$ is known, with two AlO_4 tetrahedra linked by a bridging oxygen[26], but details of changes in the local atomic arrangements across the YAM-NYAM series are unknown.

The α-Si_3N_4 sample was a commercial powder produced by nitriding silicon metal and the β-Si_3N_4 was produced by phase transformation of α-powder during hot-pressing in the presence of a liquid sintering aid. α-Si_3N_4 gave two peaks at -46.2ppm and -48.4ppm (Fig. 4.3(a)) while β-Si_3N_4 has a single peak at -48.8ppm (Fig. 4.3(b)), in agreement with a previous study[27] although the resolution here is much improved. The β'-sialons formed by hot-pressing are single phase according to both XRD and SEM, show a single resonance at -48ppm (x=1, Fig. 4.3(c)) in agreement with a previous study[27]. The β'-sialons show no noticeable change in the isotropic chemical shift across this series but there is an increase in the linewidth (FWHM, 210Hz (x=0.5)→400Hz(x=2) (Table 4.1)). The metastable β"-sialon ($Mg_5AlSi_3O_{11}N$) was crystallized from a β"-glass at 1000°C for 10 days. The ^{29}Si spectrum shows a minor peak at -47ppm and two major peaks at -62ppm and -75ppm, unlike the previous

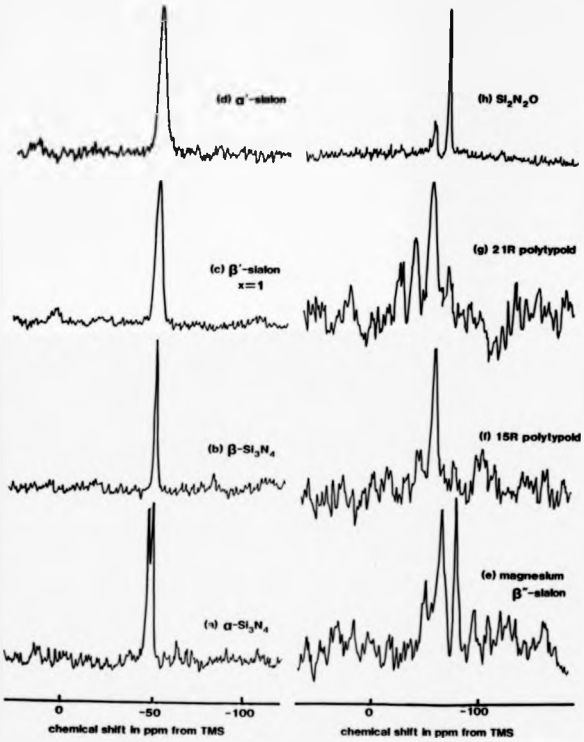

Figure4.3 Silicon-29 spectra of silicon nitride,silicon oxynitride and related Si-Al-O-N ceramics.

study[27] which gave the -75ppm resonance as only a minor peak. α'-sialon gave a single NMR spectral line at -47.8ppm (Fig. 4.3(d)). The polytypoids are also nominally single phase produced by hot-pressing with 15R (A=5) showing a single peak at -49.4ppm (Fig. 4.3(f)) while 21R (A=7) has two definite peaks at -48.9ppm and -32ppm (Fig. 4.3(g)), although the poor S/N increases the error above the ±0.5ppm normally quoted.

Commercial Si_2N_2O shows a dominant peak at -61.9ppm with a smaller peak at -49ppm due to 5% Si_3N_4 impurity (Fig. 4.3(h)). Yttrium N-wollastonite could not be made single phase, as above 1400°C it becomes unstable with respect to N-YAM. As the temperature is raised above 1400°C more N-YAM forms, while below this temperature the reaction kinetics become extremely sluggish with large amounts of unreacted Si_3N_4 remaining, according to both XRD and MAS-NMR. The highest N-wollastonite content was in a sample sintered at 1550°C for 1 hour, whose spectrum (Fig. 4.4(a)) shows three distinct resonances at -48.5ppm, -65.3ppm and -74.4ppm. XRD identifies small amounts of unreacted Y_2O_3 and Si_3N_4, in addition to the major phases N-wollastonite and N-YAM. As the shifts of Si_3N_4 and N-YAM (Fig. 4.4(c)) have been accurately determined this allows the peak at 65.3ppm to be unambiguously assigned to yttrium N-wollastonite. Y_2SiAlO_5N cannot be directly sintered, with a direct sintering of this composition at 1500°C producing $Y_3Al_5O_{12}$ and an unidentified silicon-containing phase. A nearby glass-forming composition ($Y_{1.5}Si_{1.2}Al_{1.2}O_5N$) was crystallized under a nitrogen atmosphere at 1100°C for 10 days. A bulk of the glass crystallized to Y_2SiAlO_5N, with only minor levels of residual glass. Even after a 60 hour spectral accumulation (Fig. 4.4(b)) the S/N is poor with a peak at -73.3ppm apparent and other smaller peaks at -80ppm and -62ppm.

In contrast N-YAM may be readily prepared, with a single phase specimen resulting after sintering at 1550°C for 2 hours, producing a

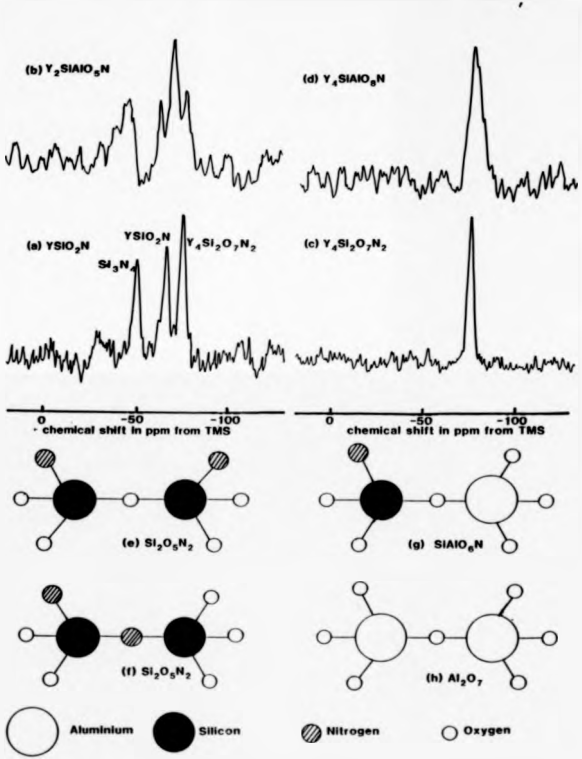

Figure4.4 (a)-(d) Silicon-29 spectra of N-wollastonite,N-YAM and related materials. (e)-(h) Si:Al:O structural units of the YAM series.

single resonance in the NMR spectrum at -74.4ppm (Fig. 4.4(c)). The solid solution which exists for this structure allows varying amounts of aluminium and oxygen substitution to be made although specimens close to the central composition (Y_4SiAlO_8N) are difficult to sinter. Sintering at this composition for 2 hours at 1700°C (the maximum temperature of the original furnace) produced very little reaction, so an alternative method of taking a composition below the YAM-line, closer to the glass-forming region (Fig. 1.2), which melts below 1700°C, was used. Sintering of such a composition produced a multiphase crystalline product which XRD showed principally to be $Y_3Al_5O_{12}$ (confirmed by ^{27}Al NMR) and an intermediate YAM (Si/Al=1.5, SEM analysis) which has a broad ^{29}Si resonance (FWHM~700Hz) at ~-75ppm. Sintering of a YAM composition with a 1:1 (Si:Al) ratio at 1775°C for 4 hours gave a single resonance at -74.8ppm which is also broader (FWHM~700Hz) than the terminal N-YAM (Table 4.1, Fig. 4.4(d)).

The obvious similarity of the isotropic chemical shifts of α', β' and polytypoids to Si_3N_4 indicate that the silicon environment must closely resemble the SiN_4 tetrahedra of Si_3N_4. Hence when Si, Al, O and N are present in a structure, these spectra show there is a preference for Si-N bonding. This local coordination data is useful for formulating structural models for these sialons but such discussions are deferred until the ^{27}Al MAS-NMR has been presented (Sec. 5.6). The Si_3N_4 spectra demonstrate that small differences in the SiN_4 tetrahedra can be detected by NMR. The two different tetrahedral coordinations in α-Si_3N_4 (average bond lengths 1.747Å and 1.740Å)[20] are readily distinguished from β-Si_3N_4 (average Si-N bond length 1.732Å)[20] which shows one distinct resonance. The correlation between bond length and the isotropic chemical shift (Fig. 4.1(b)) for Si-O bonds is invalid for Si-N bonds but the same general trend to more negative shifts with decreasing bond length is also followed in these nitrided environments.

Si_2N_2O shows a much more negative shift than Si_3N_4 emphasising how important the local, nearest-neighbour coordination is in determining the chemical shift with a change of -14ppm from Q^4, SiN_4 to Q^3, $SiON_3$. The change of shift in going to the SiO_2N_2 tetrahedra of N-wollastonite at -65.2ppm is smaller, although it should be remembered that in Si_2N_2O the $SiON_3$ tetrahedra are fully connected, so are expected to be at the negative end of the $SiON_3$ shift range, whereas the SiO_2N_2 tetrahedra in N-wollastonite are Q^2 and towards the positive end of the shift range for SiO_2N_2 tetrahedra. The metastable aluminium-substituted wollastonite (Y_2SiAlO_5N) shows more than one site, with the major peak shifted to a more negative value compared to $YSiO_2N$. A small peak at -65ppm is possible (although S/N is poor) so that some "N-wollastonite like" rings may be present but the most likely ring compositions contain (2Si,1Al) and (1Si, 2Al). If nitrogen bonds only to silicon the principal tetrahedral coordination will be SiO_3N which would account for the negative shift in the major peak position.

High resolution spectra of N-YAM allow silicon's local coordination to be deduced. Pauling's Second Crystal Rule requires the nitrogen to be bonded to silicon rather than one of the positions coordinated by yttrium only[28]. However, two atomic arrangements of $Si_2O_5N_2$ (Fig. 4.4(e),(f)) are possible. MAS-NMR should distinguish these possiblities as one has only SiO_3N tetrahedra (Fig. 4.4(e)), whereas the other (Fig. 4.4(f)) has both SiO_3N and SiO_2N_2 tetrahedra. As the spectrum has a single resonance which is of comparable width to $YSiO_2N$ where a single silicon environment exists, the N-YAM structure with only one silicon environment is correct, which agrees with a neutron diffraction study[29]. Compared to N-YAM the intermediate YAM, $Y_4Si_2Al_2O_9N$ shows a slight negative shift and some broadening of the resonance to the negative shift side (Fig. 4.4(d)) where there may be some structure, although S/N and resolution do not allow

unambiguous interpretation. The peak position suggests that the local silicon coordination does not change from $Y_4Si_2O_7N_2$ to Y_4SiAlO_5N although there is some "disorder" present increasing the linewidth. All structural units (Fig. 4.4(e)-(h)) could be present in Y_4SiAlO_5N, so that some silicons may have nnn aluminium although the well known +5ppm shift for each nnn Si/Al substitution in framework silicates cannot then occur. The range of nnn as well as bond length and bond angles produced by the strain of having different "size" units present (Fig. 4.4(e)-(h)) are the probable sources of linebroadening.

4.2.3 Y_2O_3-Si_3N_4 System.

One compound, N-melilite ($Y_4Si_2O_3N_4$) is known to form in the Y_2O_3-Si_3N_4 system. It is isostructural with the mineral akermanite, so consists of single layers of SiO_xN_{4-x} ($0 \leq x \leq 4$) tetrahedra with the yttrium ions between the layers, although the detailed atomic arrangement about the silicon is uncertain. Under the sole constraint of stoichiometry a number of possible arrangements may be conceived (Fig. 4.5(a),(b),(c)). Structures I and III each have two distinct silicon coordinations with structure I consisting of two SiO_2N_2 tetrahedra in $Si_2O_4N_3$ groups which are connected by a third silicon in an SiN_4 environment and this is consistent with a neutron diffraction study[29]. Structure III has both $SiON_3$ and SiO_2N_2 environments while structure II differs, having just SiO_2N_2 tetrahedra. High resolution NMR should readily distinguish these different silicon environments.

The general phase development of the N-melilite composition with increasing heat treatment produces complex XRD patterns and MAS-NMR spectra (Fig. 4.5(d)-(g)). After 1 hour at 1575°C (Fig. 4.5(d)) the spectrum is dominated by unreacted β-Si_3N_4 with a number of minor peaks at -42.5ppm, -56.5ppm and -74.4ppm. With increasing

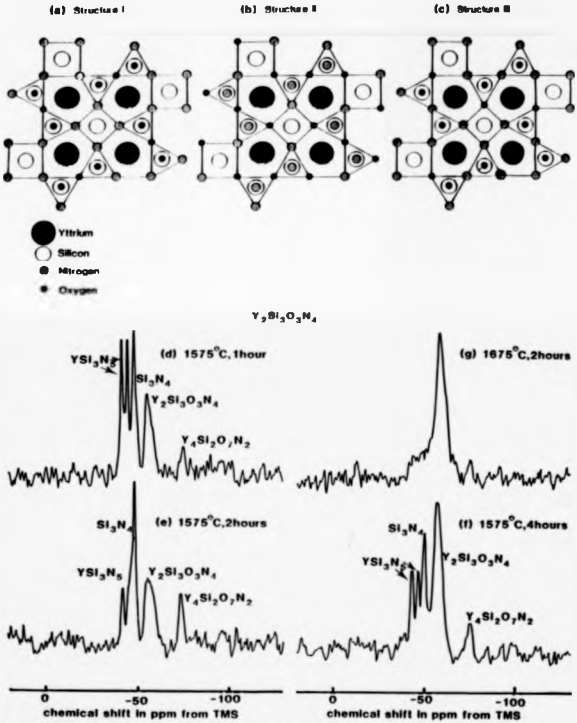

Figure4.5 (a)-(c) Local atomic arrangements of N-melilite under the sole constraint of stoichiometry. (d)-(g) Phase development of N-melilite with increasing heat treatment

heat-treatment the peaks at -42.3 ppm, -45.5ppm and -56.5ppm initially increase. Eventually after 2 hours at 1675°C almost single phase N-melilite is formed with a single broad peak at -56.5ppm (Table 4.1, Fig. 4.5(g)) and a minor resonance at -74.4ppm due to N-YAM. Correlating the changing intensities of XRD patterns and MAS-NMR spectra allows the peaks to be assigned. The presence of N-YAM is unsurprising as it has already been shown to readily form at 1550°C and reactions of Si_3N_4 usually involve some SiO_2 which forms as a surface oxidation layer. XRD identifies both N-YAM and yttrium N-melilite but the three peaks -42.3ppm, -45.5ppm and -56.5ppm cannot be assigned to $Y_2Si_3O_3N_4$ as in the final spectrum the first two peaks are absent. Their chemical shift, more positive than Si_3N_4 suggests an SiN_4 environment with some non-bridging bonds, to parallel the shift trends in silicates. A sample with little N-melilite content (Fig. 4.6(b)) allows the assignment of some XRD lines (principal lines d-spacing ~0.273nm) to the phase corresponding to the MAS-NMR peaks at -42.3ppm and -45.5ppm. A subsequent XRD study of the YN-Si_3N_4 system[30] showed three crystalline phases exist and the XRD pattern can be fitted to YSi_3N_5. The presence of some non-bridging bonds (i.e. N^- ... ^+Y) in YSi_3N_5 agrees with the shift position. The formation of YSi_3N_5 during the early stages of reaction was quite unexpected and has not previously been reported. YSi_3N_5 is a relatively minor phase even though the NMR peaks are prominent since with much longer delays (Fig. 4.5(f)) 1 minute, Fig. 4.6(c) 20 minutes) the intensity of the other peaks grow relative to those YSi_3N_5, indicating YSi_3N_5 has a shorter relaxation time than the other phases present. It is of interest to contrast MAS-NMR and XRD, since XRD shows N-YAM to be prominent while in the MAS-NMR spectrum N-YAM represents only a minor phase. As XRD depends on the X-ray structure factor a compound can give an intense diffraction pattern while

still only being a minor phase, while the NMR spectrum is essentially quantitative, with the peak intensity in a fully relaxed specimen solely dependent on the number of resonant nuclei represented by a particular phase. This demonstrates that a sample is more fully characterised by using both XRD and MAS-NMR.

The results of nominally similar heat treatments on the N-melilite composition can produce quite different phase mixtures (Figs. 4.5(a), 4.6(a); Figs. 4.5(b), 4.6(b)). This is exemplified by a mixture made up with 5mol% excess silica added, which after 2 hours at only 1575°C (Fig. 4.6(d)) produces almost complete reaction whereas a stoichiometric mixture after this heat treatment produces only limited amounts of N-melilite. The reaction kinetics have clearly been speeded up by the addition of silica probably due to the formation of a eutectic sintering liquid at this oxygen-rich melilite composition.

To allow comparison with the lanthanum system, where a 2:1 (Si_3N_4:La_2O_3) compound forms, different sintering temperatures (Fig. 4.6(e),(f),(g)) were tried on a 2:1 (Si_3N_4:Y_2O_3) composition. Initially very little reaction occurs with the major peak in the MAS-NMR spectrum corresponding to unreacted Si_3N_4 and some minor peaks, in particular at positive shifts from the Si_3N_4 position. Eventually a multiphase product results with XRD revealing a complex mixture of Y_2O_3, Si_3N_4, N-melilite, N-YAM and $Y_6Si_3N_{10}$. The peaks at -35.3ppm and -37.7ppm can be assigned to $Y_6Si_3N_{10}$ since the other peaks have previously been assigned to the other phases.

These results reveal that only one stable phase $Y_2Si_3O_3N_4$, exists along the Y_2O_3-Si_3N_4 composition line. The formation of YSi_3N_5 and $Y_6Si_3N_{10}$ in oxygen-containing systems has not previously been reported and they demonstrate that MAS-NMR can aid phase characterization of complex phase mixtures, with the chemical shifts of "unknown" materials giving a clue to their nature. The single

Figure4.8 Silicon-29 spectra of (a)-(d) N-melilite composition and (e)-(g) 2:1 Si_3N_4:Y_2O_3 composition after various heat treatments.

resonance from N-melilite is indicative of a single silicon environment which favours structure II as it consists of only SiO_2N_2 tetrahedra, as opposed to structures II and III which have two distinct nn environments. Structure II has two different Q-types (Q^3, Q^4) and this more subtle distinction may account for the increased linewidth of the ^{29}Si NMR line, compared to other single phase specimens (Table 4.1).

4.2.4 YN-Si_3N_4 System.

The three phases recently reported[30] along the YN-Si_3N_4 tie-line are at compositions 1:1 (YN:Si_3N_4), 2:1 and 6:1 (Fig. 1.2). Powder XRD has characterised the unit cells of hexagonal YSi_3N_5 and orthorhombic $Y_6Si_3N_{10}$. Synthesis of these compounds allows the assignment of phases formed during Y_2O_3-Si_3N_4 sinterings to be confirmed, together with providing SiN_4 tetrahedra of varying connectivity.

The main experimental problems in using YN are to prevent it hydrolysing which causes oxygen contamination and to generate sufficiently high temperatures for reaction of these high melting point (YN>2700°C), covalently bonded nitrides. The 1:1 (YN:Si_3N_4) composition shows very little reaction at 1575°C (Fig. 4.7(a)) while at 1725°C a complex MAS-NMR spectrum is obtained (Fig. 4.7(b)) which XRD shows principally to be $Y_6Si_3N_{10}$ with small amounts of YSi_3N_5, $Y_2Si_3N_6$ and the reactants. After 2.5 hours at 1775°C (Fig. 4.7(c)) the only spectral features are some minor structure at ~-60ppm and a prominent doublet from $Y_6Si_3N_{10}$ at -35.3ppm and -37.7ppm which suggest some silicon has been volatilised from this composition, although no significant mass-loss was detected. 2:1 (Si_3N_4:YN) compositions partially reacted after two hours at 1725°C, with resonances at

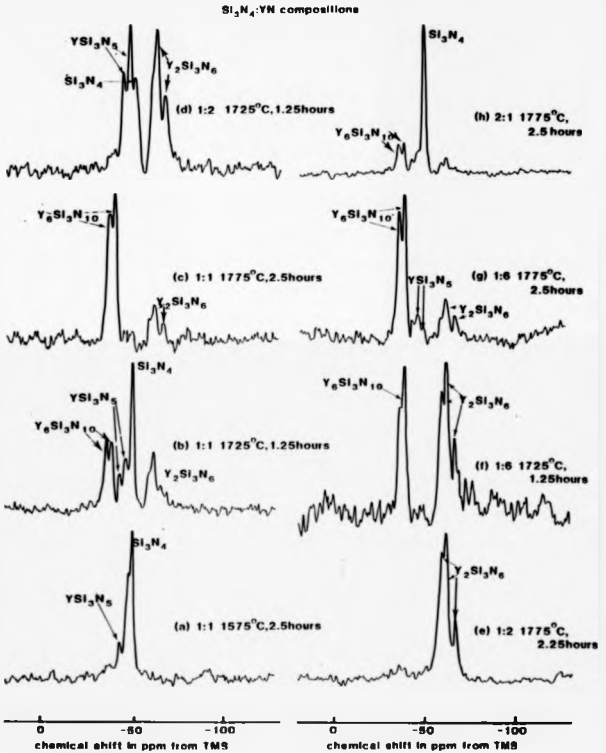

Figure4.7 Silicon-29 spectra of mixtures of yttrium nitride and silicon nitride.

-42.3ppm, -45.5ppm (both YSi_3N_5), -48.8ppm, -60.8ppm and -65.3ppm from the multiphase product. After 2 hours at 1775°C this composition produced single phase $Y_2Si_3N_6$ according to XRD, with the MAS-NMR spectrum only having peaks at -58.3ppm, -60.8ppm and -65.3ppm. The yttrium-rich 6:1 (YN:Si_3N_4) composition reacted at 1725 °C (Fig. 4.7(f)) to form $Y_6Si_3N_{10}$ and $Y_2Si_3N_6$ with some residual YN. After increased heat treatment (Fig. 4.7(g)) $Y_6Si_3N_{10}$ becomes dominant with small amounts of $Y_2Si_3N_6$ and YSi_3N_5. Attempts to sinter a 1:2 (YN:Si_3N_4) composition produced very little reaction even after 2.5 hours at 1775°C (Fig. 4.7(h)) with small amounts of each Y-Si-N phase apparent from both XRD and MAS-NMR.

The existence of three Y-Si-N phases is clearly confirmed by the MAS-NMR spectra. At 1775°C when almost complete reaction results $Y_2Si_3N_6$ and $Y_6Si_3N_{10}$ can be made as single phase products but YSi_3N_5 appears to be unstable with respect to the other two. The detailed atomic structures of these phases are unknown although they must be based on arrangements of SiN_4 tetrahedra. Two distinct SiN_4 environments exist in both YSi_3N_5 and $Y_6Si_3N_{10}$ since their resonances split into doublets, while it appears $Y_2Si_3N_6$ has three distinct environments. A simplistic view would expect that as the Y/Si ratio increases the number of non-bridging bonds increases and hence the average connectivity of the tetrahedra would decrease. If this were to parallel the ^{29}Si shift trend in SiO_4-containing materials the chemical shift would become more positive as the Y/Si ratio increases. Hence all these phases may be expected to have more positive shifts than Si_3N_4 (which is fully connected) and both YSi_3N_5 and $Y_6Si_3N_{10}$ fit into this trend but $Y_2Si_3N_6$ clearly does not. This emphasises that it is difficult to predict the chemical shift without a detailed knowledge of the local atomic structure. Even this small sample of compounds shows extensive overlap of the shift ranges of SiN_4 tetrahedra with different connectivities.

4.3 The La-Si-O-N System

4.3.1 La_2O_3-SiO_2 System.

Phase diagrams of the La_2O_3-SiO_2 system[31] show three crystalline silicates at compositions 1:1 (La_2O_3:SiO_2), ~2:3 and 1:2, although one study[32] claimed no silicate La_2SiO_5 formed. The 2:3 composition is probably more accurately described by a formula $La_{4.33}Si_3O_{12-13}$, being an extension of the N-apatite solid-solution to the pure silicate phase boundary. The disilicate composition shows limited polymorphism with a low temperature (l) tetragonal form transforming to a high temperature (h) orthorhombic form at ~1275°C. Lanthanum belongs to the group of "large" rare-earth cations, unlike yttrium which behaves as a "medium" rare-earth ion, so that yttrium and lanthanum have no disilicate polymorphs in common. Accurate structural data for the $La_2Si_2O_7$ polymorphs is not available, although single crystal determinations have been made for the isomorphic $Pr_2Si_2O_7$.

Repeated attempts to sinter La_2SiO_5 in the range (1600-1700)°C always resulted in mixtures of unreacted La_2O_3 and the apatite-structured silicate with MAS-NMR showing a single resonance at -77.7ppm (Fig. 4.8(a)). To try to force La_2SiO_5 formation a lanthia (La_2O_3) rich composition was sintered at 1675°C but again only an apatite silicate formed, with XRD indicating increased levels of unreacted La_2O_3. The apatite composition sintered at 1675°C (Fig. 4.8(b)) gave a mixture of apatite (-77.7ppm) and h-$La_2Si_2O_7$ (-82.6ppm). Similarly $La_2Si_2O_7$ compositions gave multicomponent mixtures but with h-$La_2Si_2O_7$ as the dominant phase (Fig. 4.8(c)). Applying different temperatures (1575-1675)°C to the disilicate

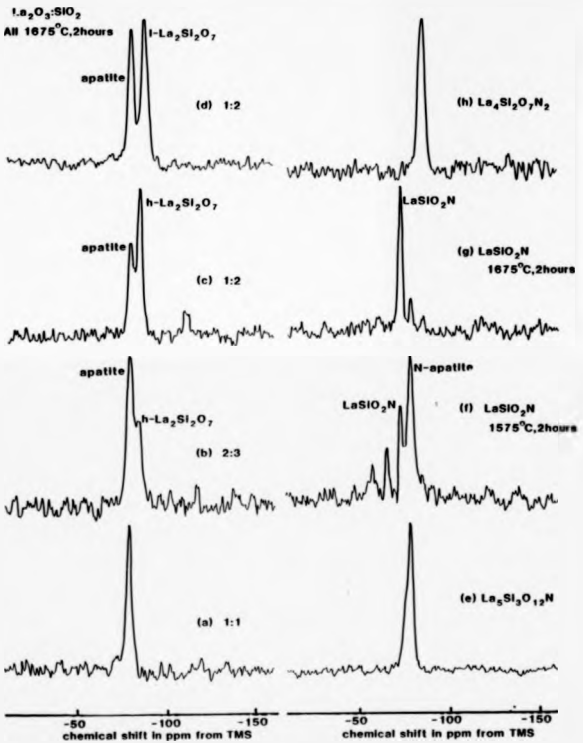

Figure4.8 Silicon-29 spectra of (a)-(d) lanthanum silicates and(e)-(h) some lanthanum silicon oxynitrides.

composition always gave mixtures but one sintering resulted in a mixture of apatite and l-$La_2Si_2O_7$ which was confirmed by both XRD and the change of the isotropic chemical shift to -84.9ppm.

Lanthanum N-apatite was easily prepared as a single phase at 1550°C, unlike the yttrium analogue where mixtures of N-apatite and Y_2SiO_5 form. Also there are not the two well resolved resonances of the yttrium system, although there is a positive shift shoulder on the main resonance (Fig. 4.8(e)). This reproducible shoulder is absent both from pure-oxygen apatite sinterings and the apatite formed by oxidation of a single phase N-apatite specimen. The peak at -77.7ppm may unambiguously be assigned to Q^0 SiO_4 while the negative shoulder of N-apatite is probably due to Q^0 SiO_3N.

Lanthanum clearly changes the relative stability of these phases compared to their relative stability in the yttrium system. In particular it is difficult to form Me_2SiO_5 which readily forms in the yttrium system and this is probably related to the increased ionic radius of lanthanum. The stability of the apatite phase has increased with both a pure-oxide apatite and single phase N-apatite forming. The apatite solid-solution clearly extends to the La_2O_3-SiO_2 phase boundary which is confirmed by the SiO_4 resonance position remaining constant throughout the compositions from $La_{4.33}Si_3O_{12-13}$ to $La_5Si_3O_{12}N$. The shift position of h-$La_2Si_2O_7$ is in agreement with a previous study (-82.4ppm)[33] and the two polymorphs can clearly be distinguished from their shift difference of ~2ppm. This must reflect a change in the local silicon environment (e.g. bond angle h~133°, l-no data) with the low temperature polymorph having a larger Si-O-Si bridging bond angle, if this angle determines the chemical shift difference. The increased widths of these resonances relative to the yttrium disilicates (Table 4.1) could be caused by increased local "disorder" or, more probably the quadrupolar nature of lanthanum

(Sec. 2.3). If the bridging bond angle was solely determining the shift variation between lanthanum disilicates and yttrium disilicates, compared to δ-$Y_2Si_2O_7$ (α-153°) the h-lanthanum disilicate would be expected to have a more positive chemical shift since its bridging bond angle is 133°. Its more negative chemical shift position demonstrates that other structural effects are important.

The Q^0 SiO_4 unit for N-apatite of -77.7ppm is positively shifted from Q^1 SiO_4 units of $La_2Si_2O_7$, as expected. The absence of any change in the shift of the SiO_4 resonance throughout the solid solution indicates that the isolated Q^0 units have very little influence on one another. The shoulder at ~-74ppm which is attributed to SiO_3N tetrahedra, indicates that the shift between successive SiO_xN_{4-x} tetrahedra can be quite small, hence distinct environments may only be partially resolved. The SiO_3N resonance in lanthanum N-apatite shows a negative shift compared to yttrium N-apatite.

4.3.2 The 2M:3X Plane.

In the lanthanum system efforts were concentrated on the La-Si-O-N face of the Janecke prism (Fig. 1.2), where the phases are better known. N-wollastonite ($LaSiO_2N$) and N-YAM ($La_4Si_2O_7N_2$) form which are isotypic with the yttrium compounds. Unlike the yttrium system no extensive YAM solid-solution exists since no pure aluminate $La_4Al_2O_9$ forms (Sec. 5.4).

Phase development of $LaSiO_2N$ is readily followed by using MAS-NMR spectra (Fig. 4.8(f),(g)]. At 1575°C (Fig. 4.8(f)] a multiphase mixture is produced with XRD indicating the presence of only N-wollastonite and N-apatite. The XRD pattern of N-wollastonite is dominant although the major peak in the NMR spectrum is N-apatite (-77.7ppm]. Three other resonances are apparent -56.8ppm, -64.7ppm and -72.4ppm. Increasing the sintering temperature increases the peak

at -72.4ppm while the N-apatite peak decreases, until after 2 hours at 1675°C (Fig. 4.8(g)) N-wollastonite dominates the NMR spectrum. The correlation of MAS-NMR spectra with XRD patterns allows the peak at -72.4ppm to be assigned to $LaSiO_2N$. Single phase N-YAM formed by sintering a stoichiometric mixture at 1550°C (Fig. 4.8(h)) gives a single resonance at -84.2ppm.

$LaSiO_2N$ produces a single resonance, indicative of a single silicon environment. The crystal structure gives the silicon coordination as Q^2 SiO_2N_2 tetrahedra, the same as for the yttrium system. The thermal stability of N-wollastonite clearly increases for the lanthanum compound relative to the yttrium compound over the temperature range (1550-1650)°C. The secondary phase in the lanthanum system is N-apatite rather than N-YAM. $La_4Si_2O_7N_2$ shows a single silicon environment, indicating only Q^1 SiO_3N units are present. Both these materials are shifted to more negative values compared to the isotypic yttrium compounds.

4.3.3 The La_2O_3-Si_3N_4 System

Some dispute exists as to the phase behaviour of La_2O_3-Si_3N_4 mixtures, in particular whether or not an N-melilite, $La_2Si_3O_3N_4$ forms. Initial studies[34] suggested $La_2Si_3O_3N_4$ formed although the XRD pattern was almost identical to $LaSiO_2N$, while another study[35] claimed all $Re_2Si_3O_3N_4$ (Re=rare-earth) compounds were isostructural and just listed the unit cell dimensions without any XRD pattern from the lanthanum compound. More recently it was claimed[36] no N-melilite formed and the 1:1 composition melted at 1650°C forming a mixture of N-apatite, N-wollastonite and $La_2Si_6O_3N_8$. Unlike the yttrium system a compound forms at the $2Si_3N_4$:$1La_2O_3$ composition in common with other large rare-earth cations (e.g. Ce). All that is known about this phase is that it indexes on an orthorhombic unit cell

with no information about the local structure available since unlike most other oxynitride materials there is no mineral analogue.

Various mixtures of Si_3N_4 and La_2O_3 were sintered at 1675°C with the 1:1 (Si_3N_4:La_2O_3) and 2:1 compositions more extensively investigated by employing a range of sintering temperatures. MAS-NMR of the 3:1 composition gave three peaks (Fig. 4.9(a)) at -49ppm, -56.5ppm and -64.6ppm. The 2:1 composition shows the same three peaks (Fig. 4.9(b),(c)), with increasing heat treatment resulting in the peak at 49ppm disappearing while those at -56.5ppm and -64.6ppm increase. Correlation of the XRD patterns with the NMR spectra shows the -56.5ppm peak to be from $La_2Si_6O_3N_8$ while that at -64.6ppm is $LaSi_3N_5$. $LaSi_3N_5$ could not be detected in the XRD powder patterns of specimens sintered at 1575°C and 1625°C, which XRD shows to be single phase $La_2Si_6O_3N_8$, while the MAS-NMR peak is clearly visible (Fig. 4.9(b)). At the 1:1.5 composition these two phases are again present (Fig. 4.9(d)). The 1:1 (N-melilite) composition produced some complex spectra with an abrupt change in these spectra about the melting point. Those spectra from samples sintered below the melting point (Fig. 4.9(e)) show a prominent peak at -64.6ppm and minor peaks at -56.5ppm, -72.8ppm and -77.2ppm, although the latter two are not resolvable in a specimen sintered at 1625°C. These specimens have a distinctly yellow-ochre hue unlike the grey or off-white ceramics normally produced. XRD showed dominant $LaSiO_2N$ peaks, with much lower intensity $LaSi_3N_5$ peaks and the 1575°C specimen showed traces of N-apatite. This explains why the initial work[34] identified the existence of a crystalline N-melilite but gave an XRD pattern identical to $LaSiO_2N$. Specimens sintered at 1650°C (Fig. 4.9(f)) appeared partially melted with SEM showing it to have almost pore-free regions (i.e. melted) surrounded by quite porous regions characteristic of a solid-state sintered ceramic. This confirms that

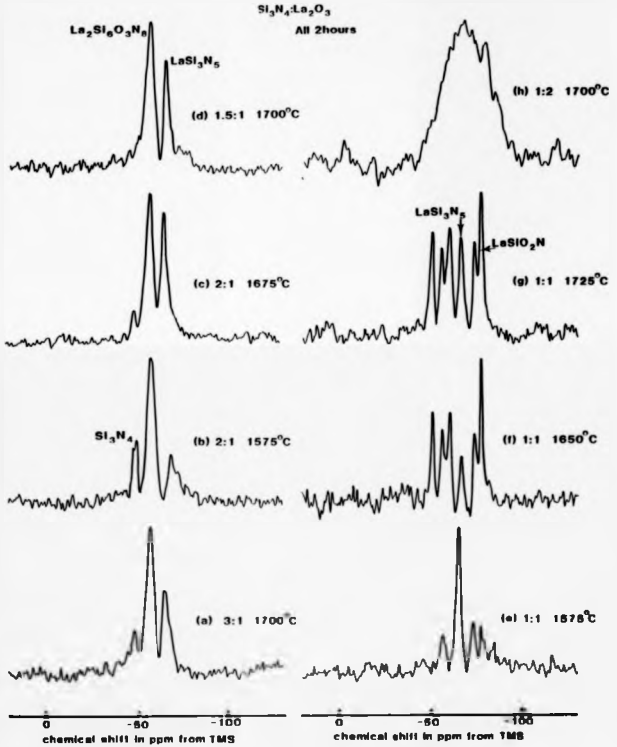

Figure4.9 Silicon-29 spectra of sintered mixtures of silicon nitride and lanthia.

the melting point of this composition is close to 1650°C. The specimen sintered at 1725°C melted and gave a similar NMR spectrum (Fig. 4.9(g)) to the 1650°C specimen. Six peaks (-50, -54.7, -59, -64.8, -72.5, -75.9)ppm occur reproducibly, although their relative amplitudes change with different sinterings. The XRD patterns are still dominated by $LaSiO_2N$ (d-spacing 0.476nm, 0.366nm, 0.291nm) show a definite splitting in specimens from above the melting point. The NMR peaks at -64.6ppm and -72.5ppm are due to $LaSi_3N_5$ and $LaSiO_2N$ respectively, with the origin of the other peaks remaining unknown at present. Above the melting point at this composition $LaSi_3N_5$ becomes unstable as the peak intensity is much reduced. Although N-wollastonite appears to be only a minor phase it has a very long T_1 relaxation time which results in the peak intensity from the N-wollastonite being much reduced compared to the other, faster relaxing phases under normal accumulation conditions. Although some of the other peaks are close to β-Si_3N_4, $La_2Si_6O_3N_8$ and $La_5Si_3O_{12}N$, they cannot be assigned to these phases since they cannot be exactly matched to the isotropic chemical shifts and widths of these peaks. Once the N-wollastonite peaks have been removed from the XRD patterns, many low intensity peaks remain which cannot be identified with any of the crystalline lanthanum silicon oxynitride phases which are known to exist nor any of the reactants. A Si_3N_4:2La_2O_3 composition sintered at 1675°C melted, producing an XRD powder pattern with some weak crystalline peaks (d-spacing ~0.325nm, 0.294nm) and a broad underlying component. The MAS-NMR peak (Fig. 4.9(h)) is very broad (FWHM~2kHz) indicating a glassy rather than a crystalline product.

The MAS-NMR spectra provide additional information which helps to clarify the phase relationships in this system and allows comparison with previous studies. The only stable crystalline phase on the La_2O_3-Si_3N_4 tie-line is $La_2Si_6O_3N_8$ which appears to lie on a

tie-line with the pure nitride, $LaSi_3N_5$. This nitride forms during the early stages of reaction of the $1Si_3N_4$:$1La_2O_3$ composition (cf yttrium) in agreement with an earlier study[37]. Another study[36], based on XRD analysis, showed distinct temperature regimes at which different crystalline phases formed from the 1:1 composition. Below 1250°C, M-wollastonite and $La_4Si_2O_7N_2$ form, between (1250°-1650)°C M-wollastonite and Si_3N_4 are present, while in the high temperature regime (>1750°C) $La_2Si_6O_3N_8$, N-apatite and a glass form. It is probable XRD gives an incomplete picture, since for many samples which XRD shows to be principally $LaSiO_2N$, NMR shows to be more complex phase mixtures. These results show $LaSiO_2N$ forms from the $1Si_3N_4$:$1La_2O_3$ composition at all sintering temperatures with no preferential formation of $La_2Si_6O_3N_8$ or N-apatite at higher temperatures. One study[36] tentatively suggested that a glass may form close to the La_2O_3-Si_3N_4 phase boundary. The 1:2 composition clearly confirms this for the first time as there is no ambiguity about the presence of a glass from the linewidth, although the exact composition is less certain. As the whole sample appears glassy and quite stable even after moderate cooling rates the Si_3N_4:$2La_2O_3$ composition must be close to the eutectic. This also explains the behaviour of the 1:1 composition since if it is too close to the glass-forming region, any glassy phases formed towards the edge of this region are less stable, hence cooling from just above or close to the melting point can result in metastable crystalline phases forming, which could have a number of silicon sites. All these results show $La_2Si_3O_3N_4$ does not form, from the preparations used here.

The single ^{29}Si resonance from $La_2Si_6O_3N_8$ indicates one distinct silicon environment is present in this phase and any structural model should be constrained to a single type of tetrahedral environment. The nitrogen-rich composition would suggest $SiON_3$

tetrahedra which agrees with the resonance position although the NMR spectra cannot conclusively prove this.

4.3.4 LaN-Si_3N_4 System

Pressure sintering of an equimolar mixture of La_2O_3 and Si_3N_4 at 2000°C under a nitrogen atmosphere produced well sintered specimens with small single crystals of a new phase on the surface, in a previous study[37]. This phase was identified as $LaSi_3N_5$, which single crystal XRD revealed to be composed of SiN_4 tetrahedra in five-membered rings with large lanthanum ions at the centre of these rings. Two distinct nitrogen environments are present with 2/5 of the nitrogens coordinated by 3 silicon atoms and the remaining 3/5 coordinated by 2 silicon and 2 lanthanum nn. According to the single crystal data the SiN_4 tetrahedra have similar Si-N bond lengths (~1.73Å) to Si_3N_4 and the number of nitrogens which have non-bridging bonds attached to a particular silicon (i.e. $N^{\delta-}$ ... $^{\delta+}La$) vary between 1 and 3. No evidence for any other La-Si-N phases has been published.

To allow comparison with the yttrium system the same stoichiometric mixtures of LaN and Si_3N_4 were sintered at (1725-1775)°C. LaN reacts with oxygen/water even more rapidly than YN, so some oxygen contamination may be expected. After sufficient heat treatment (Fig. 4.10(a)) $LaSi_3N_5$ develops as the major phase according to XRD and can be assigned to the MAS-NMR peak at -64.6ppm. The minor phases present are Si_3N_4(-49ppm) and $La_2Si_6O_3N_8$ (-56.5ppm) which were assigned by matching the chemical shifts and were confirmed by XRD. A preliminary investigation of LaN-rich compositions produced noisy XRD patterns with a few narrow lines that cannot be matched to any known phases that are likely to occur in this system (e.g. LaN, Si_3N_4, $LaSi_3N_5$, $La_2Si_6O_3N_8$). A distinct change in the NMR spectra (Fig. 4.10(b),(c),(d)) is apparent. The 2LaN:Si_3N_4 composition has

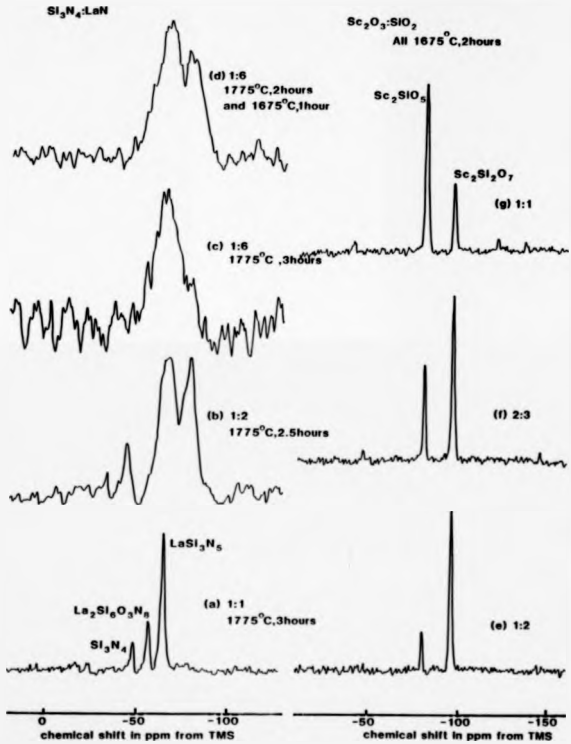

Figure4.10 Silicon-29 spectra of (a)-(d) sintered mixtures of silicon nitride and lanthanum nitride and (e)-(g) scandium silicates.

definite peaks at -65ppm and -78ppm with much increased linewidths (FWHM~770Hz). The 6LaN:Si_3N_4 composition melted below 1775°C and gave a broader resonance still (FWHM~1.1kHz), which peaks around -65ppm. When this composition is first heated to 1775°C (2 hours), then held at 1675°C (1 hour) a second peak at -78ppm develops (Fig. 4.10(d)).

The resonance from $LaSi_3N_5$ is quite narrow (FWHM~120Hz) with no sign of any structure. This indicates a single silicon environment which is the case from a nn consideration, although there are differing numbers of non-bridging nitrogens attached to the silicon atoms. The situation is more complex than silicate systems since nitrogen is trivalent so that a nitrogen can have a non-bridging bond and still be connecting two SiN_4 tetrahedra. The conclusion which may be drawn is that the non-bridging effect is not as important as for SiO_4 containing systems. Comparison with YSi_3N_5 (hexagonal) which gives a doublet that is positively shifted from $LaSi_3N_5$ indicates that their structures are different. Extensive overlap of the different SiO_xN_{4-x} ($0 \leq x \leq 4$) is shown by isotropic shift of $LaSi_3N_5$. The spectra from the LaN-rich compositions indicates that other new phases exist (probably with some level of oxygen) which exhibit some disorder causing the much increased resonance linewidths.

4.4 Sc_2O_3-SiO_2 System

In the scandium system two silicates exist (Sc_2SiO_5, $Sc_2Si_2O_7$) but no intermediate silicate ($Sc_4Si_3O_{12}$) or N-apatite have been reported. Sc_2SiO_5 consists of isolated SiO_4 tetrahedra but no accurate bond length data could be located. The disilicate which is isostructural with the mineral thortveite, exhibits no polymorphism unlike yttrium and lanthanum. $Sc_2Si_2O_7$ has the same structure as β-$Y_2Si_2O_7$ with a bridging bond angle Si-O-Si of 180° and an average

Si-O bond length of 0.162nm[33].

The results of sintering 3 compositions (1:1(Sc_2O_3:SiO_2), 2:1 and 1:2) at 1675°C for 2 hours agree with there only being two phases in this system (Fig. 4.10(a)-(g)). All produced phase mixtures of Sc_2SiO_5 and $Sc_2Si_2O_7$ with the relative amplitudes changing as expected with composition. This allows assignment of the MAS-NMR peaks to Sc_2SiO_5 (-80.0ppm) and $Sc_2Si_2O_7$ (-95.5ppm).

A previous study[33] measured the shift of $Sc_2Si_2O_7$ as -95.3ppm, in agreement with the value obtained here. The 180° bridging bond angle (O) means this Q^1 unit shows a marked negative chemical shift. Comparing $Sc_2Si_2O_7$ to β-$Y_2Si_2O_7$ (-93.6ppm) the increased negative chemical shift of the scandium disilicate is attributable to the increased electronegativity of scandium (1.3 Pauling units) relative to yttrium (1.2) which increases the ionicity of the Si-O bond. However, this is a relatively minor effect for this small electronegativity difference compared to other local structural influences such as bond angle on the chemical shift.

4.5 Discussion of Trends of the ^{29}Si Chemical Shift

The chemical shift ranges for tetrahedra SiO_xN_{4-x} ($0 \leq x \leq 4$) show a general trend to more positive chemical shifts with decreasing x (Fig. 4.11, Table 4.1). For the oxynitrides when cation effects are absent (e.g. Si_3N_4, Si_2N_2O, SiO_2) the isotropic chemical shift appears to follow an almost linear variation, with steps of ~15ppm between successive units ($\Delta x=1$). In fitting Gaussians to spectra from Y-Si-Al-O-N glasses a similar linear step of 12.5ppm was used[38]. The semi-empirical group electronegativity approach for the calculation of the chemical shift also assumes a linear variation with the electronegativity of the attached groups. This variation can be used as a first approximation, although in other mainly solution-state

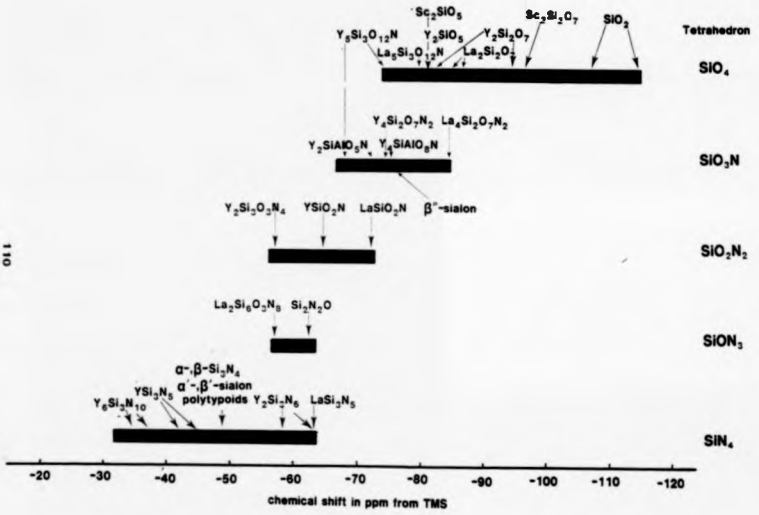

Figure4.11 Silicon-29 isotropic chemical shifts from crystalline materials of the (Y,La,Sc)-Si-Al-O-N systems.

Phase	Proposed local Si structural Unit	Isotropic chemical shift ppm (wrt TMS=0ppm) ±0.5ppm	FWHM ±20Hz Hz	Phase	Proposed local Si structural unit	Isotropic chemical shift ppm (wrt TMS=0ppm) ±0.5ppm	FWHM ±20Hz Hz
Y_2SiO_5	$SiO_4.Q^0$	-79.8	<100	$Y_2Si_3O_3N_4$	$SiO_2N_2.Q^3,Q^4$	-56.5	430
α-$Y_2Si_2O_7$	$SiO_4.Q^1$	-83.4	350	Si_2N_2O	$SiON_3.Q^1$	-61.9	120
β-$Y_2Si_2O_7$	$SiO_4.Q^1$	-93.6	80	$La_2Si_6O_3N_8$	$SiON_3.Q^1$	-56.8	350
γ-$Y_2Si_2O_7$	$SiO_4.Q^1$	-92.8	70	YSi_3N_5	SiN_4	-45.5,-42.3	140
δ-$Y_2Si_2O_7$	$SiO_4.Q^1$	-81.2,-82.9	50	$Y_2Si_3N_6$	SiN_4	-58.3,-60.8,-65.3	150
h-$La_2Si_2O_7$	$SiO_4.Q^1$	-82.6	230	$Y_6Si_3N_{10}$	SiN_4	-35.8,-37.7	230,180
l-$La_2Si_2O_7$	$SiO_4.Q^1$	-84.7	280	$LaSi_3N_5$	SiN_4	-64.6	120
$La_{(4.6)}Si_3O_{12-13}$	$SiO_4.Q^0$	-77.7	200	β'*sialon $Mg_5Al_2Si_3O_{11}N$	$SiON_3$,SiO_2N_2, $SiON_3$	-82.0,-75.1	350,300
Sc_2SiO_5	$SiO_4.Q^0$	-80.0	70	β'-sialon $Si_{3-x}Al_xO_xN_{4-x}$			
$Sc_2Si_2O_7$	$SiO_4.Q^0$	-95.5	60	x=0.5	SiN_4	-48.2	210
$Y_5Si_3O_{12}N$	$SiO_4.Q^0$	-74.8	210	x=1	SiN_4	-48.0	290
	$SiO_3N.Q^0$	-67.8	220	x=2	SiN_4	-48.0	400
$Y_4Si_2O_7N_2$	$SiO_3N.Q^1$	-74.4	320	α'-sialon	SiN_4	-47.8	300
Y_4SiAlO_8N	$SiO_3N.Q^1$	-74.8	700	15R-polytypoid	SiN_4	-49.4	500
$La_4Si_2O_7N_2$	$SiO_3N.Q^1$	-84.2	270	21R-polytypoid	SiN_4	-48.9,-32	500
				α-Si_3N_4	$SiN_4.Q^B$	-46.2,-48.4	110
Y_2SiAlO_5N	$SiO_3N.Q^2$	-72.2	430	β-Si_3N_4	$SiN_4.Q^B$	-48.8	100
$YSiO_2N$	$SiO_2N_2.Q^2$	-65.2	400				
$LaSiO_2N$	$SiO_2N_2.Q^2$	-72.4	160				

Table 4.1 Summary of ^{29}Si Isotropic Chemical Shifts and Linewidths from Ceramic Phases

studies of SiX_aY_b (a+b=4) tetrahedra, the chemical shift rarely follows a linear variation[39,40] with some intermediate member having the largest p-electron imbalance about the silicon and thus having the most paramagnetic shift [Eq. 1.5]. This non-additivity results in a so-called "sagging" pattern of the chemical shifts as the attached groups are changed[34] and this effect can be expected to enhance the overlap of the chemical shift ranges from the different tetrahedra. The general trend to more positive chemical shifts with increasing nitrogen coordination about the silicon is consistent with the average covalency of the bonds increasing. Replacement of Si-O bonds by the more covalent Si-N bonds causes an increase in the paramagnetic shielding term, leading to a deshielding of the silicon making the chemical shift more positive with decreasing x.

For a particular x, there is additional variation of the chemical shift due to structural influences (Sec. 4.1). For SiO_4 tetrahedra obtained in this study, where the cation range is limited, Q^0, Q^1 and Q^4 units are clearly separated. Q^0 units give the most positive shift, since the group electronegativity of the attached group is much less than more connected units (cf EN(OY)~3.7, EN(OSi)~4.0) so that the Si-O bonds of the central silicon become more covalent. Although a similar Q-type variation can be perceived in some of the other results (e.g. SiO_3N units of $Y_5Si_3O_{12}N$,Q^0 and $Y_4Si_2O_7N_2$,Q^1; SiN_4 in YSi_3N_5, $Q^{<8}$ and Si_3N_4,Q^8), other structural influences clearly complicate this trend, as typified by the shifts of $LaSi_3N_5$ and $Y_2Si_3N_6$ relative to Si_3N_4. From the crystal structure of $LaSi_3N_5$ it is known the SiN_4 units do have some non-bridging character (i.e. $Q^{7,6,5}$) and hence would be expected to have more positive shifts than fully connected Si_3N_4. Since nitrogen tends to form a trigonal sp^2-hybridised bonding patterns the distinction between a bridging and non-bridging nitrogen is less clear than for divalent oxygen. The

second bond from oxygen forms either with a network forming atom (i.e. bridging) or an ionic species which disrupts the network (i.e. non-bridging). A single nitrogen can clearly fulfil both these roles simultaneously, so any change of the chemical shift may be less noticeable. A group electronegativity argument would give the effect of non-bridging bonds (to M) as decreasing the covalency of the M-N bonds, hence increasing the covalency of the central Si-N bond. Clearly the situation is more complex, so the range of materials containing only SiN_4 units needs to be much expanded to gain a better understanding of the mechanism that is operating.

The isotropic chemical shift does not allow unambiguous assignment of a resonance to a particular structural unit (in common with silicates). This is clear since resonances from all types of SiO_xN_{4-x} tetrahedra have been observed close to -65ppm. However, with additional information about the system, the NMR spectrum does provide a more complete description of the local structure. In some instances very subtle structural inequivalences in the silicon environment can be detected (e.g. δ-$Y_2Si_2O_7$ and α-Si_2N_4). For other cases more marked structural differences produce very much smaller changes in the chemical shift. This is exemplified by $La_5Si_3O_{12}N$ where both SiO_4 and SiO_3N tetrahedra are expected, with the only evidence for SiO_3N being a shoulder on the main resonance. In M-YAM after aluminium substitution it is expected some nnn aluminium will be present. The spectra show no splitting or the expected positive shift with Si/Al nnn substitution. This may be explained either by strict partitioning of the atoms within the structure or by the presence of nitrogen making the chemical shift less sensitive to such changes. For yttrium M-melilite where Q^3 and Q^4 SiO_2N_2 tetrahedra are expected, again no splitting of the resonance occurs. In most of the samples where

resolution of different environments is not observed the resonances are appreciably broader than in other cases (Table 4.1). This broadening may be attributed to there being an increased range of local environments although the materials are ordered over a long-range scale as XRD shows them to be crystalline. As silicon is often bonded to ^{14}N, if the nitrogen environment is sufficiently distorted the quadrupolar interaction can significantly impair the MAS-averaging of the Si-N dipolar coupling (Fig. 2.2(c))[41]. The residual linewidths could then obscure small shifts between different environments.

Comparison of the chemical shifts from nominally isostructural yttrium and lanthanum silicon oxynitrides show the lanthanum compounds always have more negative chemical shifts (Table 4.1). If the O-M bond polarity was the determining feature of the chemical shift for the SiO_xN_{4-x} unit (for given x) then with decreasing electonegativity of the attached metal atom M(ie. Si-O...M) the chemical shifts would become more positive as the O-M bond becomes more ionic. The Pauling electrongativities of yttrium (1.2) and lanthanum (1.1) should make the shifts of the lanthanum materials more positive than the yttrium analogues. The negative chemical shift of the lanthanum materials indicates that bond polarity is not the determining feature of the paramagnetic term and other structural factors have to be more important in determining the isotropic chemical shift. Lanthanum is a large rare-earth cation with an ionic radius of 1.15Å compared to yttrium which behaves as a medium rare-earth ion of radius 0.95Å. If the large lanthanum ion decreases the average Si-(O,N) distance this would increase the ionicity of the bond producing the observed shifts.

The absence of spinning sidebands from a majority of specimens is quite surprising, since in mixed environments the electron distribution is expected to be non-spherical. In most cases an adequate S/N was accumulated to observe spinning sidebands, so that their absence indicates that δ (chemical shift anisotropy) must be less than 40ppm for these $Si(O,N)_4$ units which can be compared to the yttrium disilicates where spinning sidebands were seen, implying $\delta > 40$ppm. In the mixed units some internal charge compensation has to occur, smoothing out the electron distribution.

References: Chapter 4

1. Kirkpatrick, R.J., Dunn, T., Schramm., S., Smith, K.A., Oestrike, R. and Turner, G. in "Structure and Bonding in Non-Crystalline Solids" (Ed. Walrafen, G.E. and Revesz, A.G.), Plenum Press, 1986, 303-327.
2. Grimmer, A.-R., Lampe, F.V.and Magi, M., Chem. Phys. Lett., 132, 1986, 549-553.
3. Pauling, L, "The Nature of the Chemical Bond", Cornell University Press, 1960.
4. Magi, M., Lippmaa, E., Samoson, A., Engelhardt, G. and Grimmer, A.-R., J. Phys. Chem. 88, 1984, 1518-1522.
5. Dupree, R., Holland, D., and Williams, D.S., J. Non-Cryst. Solids, 81, 1986, 185-200.
6. Grimmer, A.-R. and Radeglia, R., Chem. Phys. Lett. 106, 1984, 262-265.
7. Engelhardt, G. and Radeglia, R., Chem. Phys. Lett. 108, 1984, 271-274.
8. Smith, K.A., Kirkpatrick, R.J., Oldfield, E. and Henderson, D.M., Am. Miner. 68, 1983, 1206-1215.
9. Janes, N. and Oldfield, E., J. Am. Chem. Soc. 107, 1985, 6769-6775.
10. Grimmer, A.-R., Chem. Phys. Lett., 119, 1985, 416-420.
11. Grimmer, A.-R., Lampe, F.V., Tarmak, M. and Lippmaa, E., Chem. Phys. Lett. 97, 1983, 185-187.
12. Thomas, J.M., Klinowski, J., Ramdas, S., Hunter, B.K. and Tennakoon, D.T.B., Chem. Phys. Lett., 102, 1983, 158-162.
13. Smith, J.V. and Blackwell, C.S., Nature, 303, 1983, 185-225.
14. Dupree, R., Holland, D., McMillan, P.W. and Pettifer, R.F., J. Non-Cryst. Sol. 68, 1984, 399-410.
15. Ito, J. and Johnson, H., Am. Miner. 53, 1968, 1940, 1952.
16. Liddell, K. and Thompson, D.P., Br. Ceram. Trans. J., 85, 1986, 12-22.
17. Leng-Ward, G., (Private Communication).
18. Maksimov, B.A., Kharitonov, Y.A., Ilyukhin, V.V. and Belov, N.V., Sov. Phys. Dok., 13, 1969, 1188-1190.
19. Mitteilung, K., Grimmer, A.-R., Lampe, F.V., Magi, M. and Lippmaa, E., Mon. Chem., 115, 1984, 561-564.
20. Felsche, J., Structure and Bonding 13, 1973 99-198.
21. Grun, R., Acta. Cryst. B35, 1979, 800-804.
22. Jack, K.H., J. Mater. Sci. 11, 1976, 1135-1158.
23. Wild, S., Leng-Ward, G. and Lewis, M.H., J. Mater. Sci. 16, 1981, 1815-1828.
24. Idrestat, I. and Brosset, C., Acta. Chem. Scand. 18, 1964, 1879-1884.
25. Morgan, P.E.D., Carroll, P.J. and Lange, F.F., Mat. Res. Bull., 12, 1977, 251-260.
26. Brandle, C.D. and Steinfink, H., Inorg. Chem. 8, 1969, 1320-1324.
27. Dupree, R., Lewis, M.H., Leng-Ward, G. and Williams, D.S., J. Mater. Sci. Lett. 4, 1985, 393-395.
28. Morgan, P.E.D., J. Mater. Sci. Lett. 5, 1986, 377.
29. Roult, R., Bacher, P., Liebaut, G., Marchand, R., Goursat, P. and Laurent, Y., Acta. Cryst. A40(Suppl.), 1984, C226.

30. Thompson, D.P., in "Tailoring Multiphase and Composite Ceramics" Eds. Tressler, Messing, Pantano and Newnham, Plenum Press, 1986, 79-91.
31. Phase diagram 2372 in "Phase Diagrams for Ceramist", Ed. Levin, E.M., Robbins, C.R. and McMurdie, F., Publ. Am. Cer. Soc., 1969.
32. Kuimin, E.A. and Belov, N.V., Sov. Phys. Dokl. 10, 1966, 1009-1011.
33. Mitteilung, K., Grimmer, A.-R., Lampe, F.V., Magi, M. and Lippmaa, E., Mon. Chem. 114, 1983, 1053-1057.
34. Wills, R., Stewart, R.W., Cunningham, J.A., and Wimmer, J.M., J. Mater. Sci. 114, 1983, 1053-1057.
35. Marchand, R., Jayaweera, A., Verdier, P. and Lang, J., C.R. Acad. Paris. C285, 1976, 675-677.
36. Mitomo, M., Izumi, F., Horiuchi, S. and Matsui, Y., J. Mater. Sci. 17, 1982, 2359-2364.
37. Inoue, Z., Mitomo, M. and Nobou, I., J. Mater. Sci. 15, 1980, 2915-2920.
38. Aujla, R.S., Lang-Ward, G., Lewis, M.H., Seymour, E.F.W., Styles, G.A. and West, G.W., Phil. Mag. Lett. 54, 1986, 51-56.
39. Tossell, J.A. and Lazzeretti, P., Chem. Phys. Lett. 133, 1986, 463-465.
40. Harris, R.K. "NMR Spectroscopy", Pitman, 1984.
41. Bohm, J., Fenkze, D. and Pfeifer, H., J. Magn. Reson. 55, 1983, 197-204.

CHAPTER 5. ALUMINIUM-27 NMR.

5.1 Introduction to High Resolution ^{27}Al NMR in the Solid-State

A number of high resolution ^{27}Al NMR studies of inorganic solids over the last 6 years[1,2] have pointed out that structurally useful information is obtainable from ^{27}Al NMR spectra. In common with ^{29}Si the most important influence on the isotropic chemical shift is the local coordination. Increasing the coordination number decreases the electrostatic bond strength, leading to more electron density residing on the ions rather than in the bonds, making the system more ionic. For networks containing Al-O bonds only (i.e. no Si, B or P next nearest neighbours (nnn)) the different local coordinations have well defined chemical shift ranges (i.e. AlO_4(86-62)ppm, AlO_5(40-25)ppm and AlO_6(15-0)ppm; Fig. 5.1(a)). Hence the isotropic chemical shift provides rapid coordination determination, even for amorphous materials.

Advances in understanding how more subtle structural changes influence the isotropic chemical shift have been hindered because of the quadrupolar nature of ^{27}Al. The quadrupole interaction, although a sensitive measure of local environmental distortion, is seldom accurately obtainable from powder spectra at fixed field since the second-order quadrupole broadening is often convolved with other broadening mechanisms, washing out any quadrupole structure. Subtle changes of shielding are often masked, or the peak position is significantly shifted down frequency from the true isotropic value by the quadrupole interaction (Sec. 2.4). This shift is illustrated by the peak position of kaolinite ($Al_2Si_2O_5(OH)_4$) at different magnetic fields (peak position in ppm is proportional to B_0^{-2}, Fig. 5.1(b)). If incorrectly accounted for this effect can lead to misleading interpretation of data since the quoted shift is too diamagnetic if

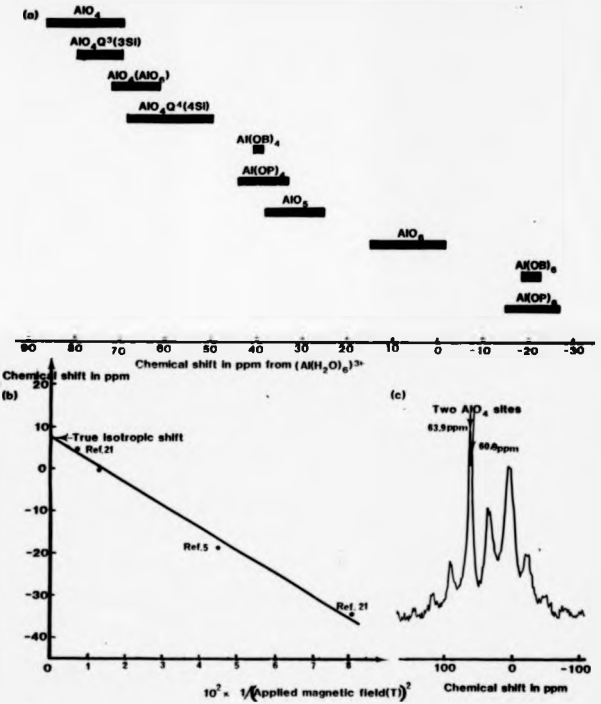

Figure6.1 (a) Aluminium-27 chemical shift of structural units containing Al-O bonds from crystalline and amorphous materials.(b) ^{27}Al peak position(in ppm)of kaolinite as a function of the squared reciprocal of the applied magnetic field.(c) ^{27}Al spectrum of nepheline showing two distinct tetrahedral(AlO_4)sites. (Octahedral site(~4ppm)due to a secondary phase).

neglected or too paramagnetic if corrected by calculating the quadrupole interaction assuming a Gaussian lineshape[3]. This is exemplified by andalusite (Fig. 2.4) as the AlO_5 peak (peak position ~10ppm, B_o=9.4T) has been attributed to AlO_6 units[4] since the quadrupole induced shift moved the peak position into the AlO_6 isotropic shift range. Some authors[5] have suggested that markedly different shifts occur for similar structural units, but this was based on peak positions rather than isotropic shifts and once quadrupole shifts have been taken into account it is likely these apparent differences will be largely removed. This is typified by the polymorphs β-$LiAlO_2$ (e^2qQ/h~1.8MHz) and γ-$LiAlO_2$ (e^2qQ/h~3.2MHz), both of which have similar AlO_4 local coordinations with apparently a large shift difference in peak positions (>10ppm at B_o=6.4T), but this is reduced to ~1ppm once quadrupole corrections have been included[6].

Techniques have been developed to determine the isotropic chemical shift from quadrupole perturbed spectra including:-

(I) Computer simulation of spectra[7].

(II) Centre of gravity for spinning sidebands of satellite transitions[8].

(III) Quadrupole correction from known efg.

(IV) Extrapolation of the field-dependent peak position.

Application of these techniques to ^{27}Al in materials solely comprised of AlO_4 tetrahedra show no distinct shift ranges for the different Q^nAlO_4 units[9]. The strong ionic character of the Al-O bond is reflected in smaller differences between bridging and non-bridging bond lengths in aluminates as compared to silicates and phosphates, which may explain the inability to clearly distinguish different Q^nAlO_4 units. When octahedral aluminium is adjacent to AlO_4 units the oxygen at the corners of the tetrahedra is usually shared between 4 aluminiums and a decreased paramagnetic shift results as the

bonds become more ionic. In aluminosilicates, provided stoichiometry allows, Lowenstein's rule limits the framework nnn of AlO_4 units to silicon only[10]. Well resolved chemical shift ranges for Q^4(4Si) and Q^3 (3Si) (Fig. 5.1(a)) have been found which are probably due to nnn effects rather than the different connectivities, as changing nnn results in AlO_4 units with definite shift ranges. Increasing nnn electronegativity (EN(P)>EN(B)>EN(Si)) leads to increased ionicity of the Al-O bond, decreasing the paramagnetic shift and this has been demonstrated in both crystalline and amorphous materials[11,12]. In some aluminosilicates small inequivalences may be detected (Fig. 5.1(c)), although similar inequivalences cannot be observed in others, presumably due to quadrupolar broadening obscuring them. Correlations between the isotropic chemical shift and the Al-O-T(T=Si,P) bond angle, similar to that for silicon have been attempted[3,13], although a more limited data set was employed and the accuracy of the chemical shifts is generally less reliable than ^{29}Si.

For AlO_6 octahedra similar nnn effects have been observed with all AlO_6 shifts being more negative than for AlO_4 due to the increased coordination number. A covalency scale for differently connected AlO_6 units, based on chemical shifts has been suggested, with increasing covalency through the series isolated<corner-sharing <edge-sharing <face-sharing[5]. This scale should be treated somewhat sceptically as peak positions rather than isotropic values were used. It is unlikely that distinct shift ranges for these units will be observed given the chemical shift dispersion once quadrupole corrections have been made.

The chemical shift anisotropy (csa) provides information about the shielding variation around the aluminium but no csa effects for aluminium have yet been published. The strong ionic character of the Al-O bond would lead to a small csa and any distortion of the

electronic environment which produces csa, also gives rise to an efg resulting in quadrupol ar broadening which will probably mask any csa effects.

5.2 The Problem of Aluminium Quantification by NMR Spectra

Even the earliest CW NMR experiments of quadrupolar nuclei found the signal intensity-number of nuclei proportionality of the NMR spectrum was not strictly obeyed. The effect of dislocations in metals[14] reduced the spectral intensity to the value expected solely from the central transition while annealing these specimens restored the full intensity in these cubic ($e^2qQ/h=0$) materials. Addition of alloying elements (point defects) to cold-worked metals further reduced the intensity below that of the central transition as second-order quadrupole broadening occurred. Defects affect the efg by introducing a strain (ε)which changes nearest neighbour (nn) distances and the ion core polarisation (for dislocations, $\Delta(eq)=6\lambda e\varepsilon a^{-3}$ a-nn distance, λ-ion core distortion[14]). For a FCC metal lattice the frequency displacements of first, second and third nn shells about a point defect were found to be 27:3.4:1[15]. This explained the simple "all-or-nothing" model which could be fitted to the NMR intensity results from metals, since no appreciable broadening accompanied the increasing loss of signal intensity as the concentration of point defects increased. Similar effects were found in ionic crystals[16].

In pulsed NMR experiments further complications are introduced with the peak pulse magnetisation differing from CW experiments (Sec. 2.4). Particular pulse lengths have differing effects on different transitions and on samples with different sizes of quadrupole interaction. For different sizes of quadrupole interaction the effect is reduced by employing short, intense RF-pulses (Eq. 2.25, Fig. 2.5(b)) although problems with quantitative interpretation still exist, even if they are not always considered. If the efg is

sufficiently large and inadequate excitation is employed no resonance is observed which has been demonstrated by the absence of octahedral ^{27}Al resonances from basic aluminium sulphate[17] and andalusite (AlO_6, e^2qQ/h=15.6MHz). A study of phyllosilicates pointed out that the AlO_6/AlO_4 ratio's determined for compounds by MAS-NMR often markedly disagreed with known crystal structures[18]. In amorphous materials, where the range of environments in a sample is increased compared with a crystalline materials, the amount of aluminium recorded in the NMR spectra is variable[5,19] and levels as low as 2% of the total aluminium content have been attributed to the recorded signal.

Techniques have been developed to try to determine how much aluminium is represented by the spectra. The number of aluminium nuclei present in a sample may trivially be estimated by weighing the sample. The signal intensity can be measured either from the FID or the spectrum. The initial intensity of the FID often has to be estimated by extrapolation to t=0, as system deadtime prevents the amplitude immediately after the pulse being accurately recorded. One technique[20] involves setting the signal exactly onto resonance (to make extrapolation easier) and adjusting the receiver phase to put all the signal into one quadrature channel. An almost identical technique uses the initial intensity of the FID following a pulse whose duration maximises the intensity of the FID[21]. Some variation in intensity can be expected between samples for this case (Fig. 2.5(b)). In this study the amount of aluminium was estimated by simply integrating the spectra obtained after short (0.5μs)intense (B_1~5mT) pulses. A comparison between FID extrapolation and spectral integration was made on a few samples with the methods agreeing within experimental error. These methods require a standard from which all the aluminium signal is observed and produces the same system response as the other

samples. The use of dilute aqueous solutions of aluminium salts was not possible since susceptibility and dielectric effects considerably alter the probe tuning. α-Al_2O_3 was chosen as an arbitrary reference for these insulating ceramics which all have similar dielectric properties.

The signal intensity per aluminium nucleus from different samples is quite variable as can immediately be seen from the results of signal integration (Table 5.1(a)). A similar variability can by seen in the results from another study[21] using the FID technique (Table 5.1(b)). Note that materials common to both studies give similar relative intensities, although it is not obvious why agreement should be so close as results from maximising the FID would be expected to be more dependent on the efg (Fig. 2.5(b)) and the studies were carried out at different magnetic fields. The samples which give larger signal integrals ($\geq$2, Table 5.1(a)) all have small enough efgs that the higher-order transitions noticeably contribute to the signal, although they are not the 4 times larger expected if all higher-order transition intensity is measurable (Table 2.2). Loss of higher-order transition intensity occurs more readily than the central transition since these transitions are susceptible to first-order quadrupole broadening. Static spectra accumulated for ammonium alum (e^2qQ/h~0.4MHz)[22], α-Al_2O_3 ((Cq)~2.39MHz)[23] and AlN (Cq - unknown) allowed examination of the higher-order transitions. In both ammonium alum and α-Al_2O_3 all 5 transitions were apparent although the intensities of the outer transitions were much reduced relative to the central transition, with the reduction much larger for α-Al_2O_3. For AlN none of the higher-order transitions could be observed. For the central transition, theory would expect that provided short enough pulses are employed all intensities should be equal[24]. This can be demonstrated by considering the two extremes e^2qQ/h >5MHz (peak

Table 5.1 Relative ^{27}Al Signal Intensities from NMR Spectra

(a) This study, based on spectral integral (B_0=8.45T)

Sample	Relative aluminium integral per nucleus ±0.1 (Arbitrary units) (α-Al_2O_3=1)	Sample	Relative aluminium integral per nucleus ±0.1 (Arbitrary units) (α-Al_2O_3=1)
α-Al_2O_3	1	Spinel(mineral)	1.1
γ-Al_2O_3	1	spinel (x=2.1)	0.9
		β'-sialon ($Si_{3-x}Al_xO_xN_{4-x}$	
$AlCl_3.6H_2O$	2.4	x=0.5	0.1
$AlCl_3$	0.8	x=1	0.2
ALON(5AlN !9Al_2O_3)	0.4	x=2	0.5
		β''-sialon	
AlN	0.64	$Mg_5Si_3AlO_{11}N$	0.1
$YAlO_3$	0.8	15R polytypoid	0.3
$Y_3Al_5O_{12}(AlO_6)$	0.9	21R polytypoid	0.3
(AlO_4)	0.4	Pyrophyllite	1.3
$Y_4Al_2O_9$	0.4	Topaz	0.3
		Chabazite	0.9
$Y_4Si_2Al_2O_8N$	0.5		
$NH_4Al(SO_4)_212H_2O$	1.9	Analacite	0.6
$LaAlO_3$	1.9	Kaolinite	0.8
$LaAl_{11}O_{18}$	1.1	Pollucite	0.6

Table 5.1 Relative ^{27}Al Signal Intensities from NMR Spectra

(b) Maximum FID intensity (taken from (21))
(B_0 = 11.7T)

Sample	Relative FID maximum intensity	$\frac{e^2qQ}{h}$ (MHz)
$AlCl_3.6H_2O$	100	0.05
α-Al_2O_3, Low S.A.	40	2.39
α-Al_2O_3, high S.A.	30	2.39
Albite	44	3.29
Anorthite	28	5.8 (av)
Kaolinite	40	3
Gibbsite	35	3
Pyrophyllite	50	2
Muscovite	22	2.5
Margarite	18	2.5

(S.A. = Surface area).

intensity $I_{\omega,\omega 1} = \omega_{eq}$ and e^2qQ/h^-0 (peak intensity $I_O=(3I_{eq})$ and $\omega_1=\omega_O=(\omega_{eq}/3)$]). After an α ($=\omega_1\tau_p$) pulse the signal intensity is I_{eq} (α-small) and $I_O\omega_O=I_{eq}\omega_{eq}$ (Sec. 2.4), so comparable intensities would be expected from all samples.

There does not appear to be any strong correlation between the loss of intensity and quadrupole interaction strength (where known). The range of intensities may be explained if quadrupolar broadening removes some sites from the spectra. General distortions of an environment increase the efg. XRD characterisation presents some kind of long-range average from which the bond lengths and angles are obtained. In a "real" solid there are numerous imperfections (e.g. dislocations, point defects, surfaces, a distribution of environments) which lead to distortions of the local environment and could broaden the signal beyond detection. These effects have been observed in CW experiments in both metallic and ionic samples. As the samples in this study are powdered, surface areas may be significant and large distortions of the local coordination units near the surface are expected. The study of Kinsey[21] noted a difference in the signal intensity from high and low surface area aluminas, although experimental error did not allow unambiguous interpretation.

Now consider mixed species AlX_aY_b (a+b=4,6), for symmetric units where all bonds are identical (e.g. AlX_4, T_d symmetry) the efg is zero. From this study even the end-members (a or b=0) can have large efgs due to distortion of the units. For mixed units (e.g. AlX_3Y) although fortuitous cancellation of efg effects from the attached species is possible, usually these units will have large efgs due to the different charges and bond lengths associated with the different elements X and Y. Calculations using a point-charge model showed that this effect is proportional to a factor $(e_x/r_x^3 - e_y/r_y^3)$, where $e_{x,y}$ and $r_{x,y}$ correspond to the charge and distance from the

nucleus of the species X and Y[25]. For an AlO_3N unit (e_O=1e e_N=1.5e r(Al-O)= 0.175nm and r(Al-N)=0.187nm) an efg ~1MHz is predicted. However, any covalent character will increase the efg because of polarisation of the electronic charge within the bond[25]. As the Al-X,Y bonds have differing covalency, this variation in bonding will increase the efg at the nucleus. A large increase in linewidth in going from AlX_4 to AlX_3Y species has been observed in the solution-state[26]. Also in MAS-NMR spectra of glasses signal has been recorded from the end members $Al(OAl)_4$ and $Al(OB)_4$ but it was unobservable from the units with different nnn (eg. $Al(OAl)_3(OB)_1$) which was ascribed to quadrupole broadening effects[12]. The above results make it unlikely that units containing both Al-O and Al-N bonds will be observed in high resolution ^{27}Al spectra. The complete absence of resonances is an extreme example of the "missing" intensity that occurs to some extent from all pulsed NMR spectra of quadrupolar nuclei in solids. Hence an estimate should always be made of the relative fraction of the nuclei in a sample that is represented by the NMR spectrum.

5.3 The Y_2O_3-Al_2O_3 and Y-Si-Al-O-N Systems

Three crystalline yttrium aluminate phases are known to exist, $Y_3Al_5O_{12}$ (Y_3A_5), $YAlO_3$ (YA) and $Y_4Al_2O_9$(Y_2A)[27]. Single crystals of YA and especially Y_3A_5, which is the easiest to fabricate, are commercially important solid-state laser materials when doped with neodymium. Some dispute exists as to the thermal stability of these phases with early work claiming that below 1825°C YA decomposed into Y_3A_5 and Y_2A[28]. The crystal structures and hence the aluminium coordination of these phases are well known. Monoclinic Y_2A contains two AlO_4 tetrahedra joined by a bridging oxygen[29] and (Si,N)/(Al,O) substitution occurs in Y_2A giving a complete solid solution to $Y_4Si_2O_7N_2$ (Sec. 4.2.2). Cubic Y_3A_5 contains tetrahedra which

interconnect the octahedra by corner-sharing, with the ratio AlO_4:AlO_6 equal to 3:2[30] and no silicon substitution is known in this structure. YA is believed to have two forms with a high temperature orthorhombic form containing corner-sharing AlO_6 units and a low temperature hexagonal form ($\leq$950°C)containing a distorted pentacoordinate (AlO_5) environment[31]. Substitution of silicon and nitrogen is possible in YA but the metastable intermediate Y_2SiAlO_5N has a very limited range of composition so that there is not an extensive YA-Y_2SiAlO_5N solid-solution. Any structural resemblance (i.e. XRD) between the hexagonal form of the pure aluminate YA and the substituted form is only superficial due to the yttrium atoms alone having a similar disposition, with the aluminium coordination being quite different[32]. The various preparations and heat treatments allow XRD and MAS-NMR to be contrasted as aids to phase characterisation of the solid-state (Table 5.2).

5.3.1 $Y_3Al_5O_{12}$

Samples prepared by direct sintering of the oxides and by thermal decompositon of the nitrates were single phase Y_3A_5 according to both XRD and NMR. The phase development in the nitrate preparation can be followed, with the product immediately after decompositon (300-400]°C being amorphous according to XRD and MAS-NMR (Fig. 5.2(a)]. NMR shows in this amorphous product both AlO_4 and AlO_6 units are present. This completely crystallises after 30 hours at 1200°C (Fig. 5.2(b)] with MAS-NMR clearly showing two aluminium coordinations, 0.8ppm (peak position AlO_6 unit) and 74ppm (isotropic shift of AlO_4 unit). The two sites can only partially be resolved in the static spectrum (Fig. 5.2(a)] due to the increased linewidth. Direct sintering at 1775°C for 2 hours also produced single phase Y_3A_5. However, figure 5.2(d] illustrates tht spinning very close to

Table 5.2 A Comparison of XRD and ^{27}Al MAS-NMR Characterisation of the Y-Si-Al-O-N System.

Specimen	XRD	^{27}Al NMR Peak position ppm ±0.5ppm	FWHM ±5% Hz	Specimen	XRD	^{27}Al NMR Peak position ppm ±0.5ppm	FWHM ±5% Hz
α-Al_2O_3	α-Al_2O_3	11.5	1400	YA,AD,1775°C, 2 hours	Ortho YA,Y_2A,Y_3A_5	0.8 9.4	- 380
γ-Al_2O_3	γ-Al_2O_3	8 70.5	2200 ~2200	YA,ND, no heat treatment	Amorphous	8.9 74.7	2300 3600
AlN	AlN	113	1400	YA,ND,1200°C, 3 hours	YA,Y3,A5,Y2A	0.8 9.4	420 400
$Al(NO_3)_3.nH_2O$	$Al(NO_3)_3.nH_2O$	-1.2	1650	YA,DS,1775°C, 2 hours	YA(major),Y_2A,Y_3A_5	0.8	-
$NH_4Al(SO_4)_2.12H_2O$	$NH_4Al(SO_4)_212H_2O$	-0.1	1900			9.4	350
$1Y_2O_3$:$11Al_2O_3$,1775°C, 2.5 hours	α-Al_2O_3,Y_3A_5	11.6	1400	YA,single crystal	YA	9.4	420
		0.8	280	Y_2A,ND,no heat treatment (300-400)°C	Amorphous	6.1	3300
Y_3A_5,ND,no heat treatment (300-400)°C	Amorphous	6.1 72.0	2100 ~2000	Y_2A,ND,1200°C,30 hours	Y_2O_3,Y_2A,YA,Y_3A_5	69.5 0.8 9.5	- - 380
Y_3A_5,ND,1200°C,30 hours	Y_3A_5	0.8 74.0*	240 2000	Y_2A,DS,1775°C, 2 hours	Y_2A	9.4	390
				Y_4SiAlO_8N,1775°C,4hours	Y_4SiAlO_8N	+26+70(?) +113	-
Y_3A_5, commercial prepared sample	Y_3A_5	0.8 74.0*	280 -				
				Sub-YAM Al rich compound			
Y_3A_5,DS,1775°C,2 hours	Y_3A_5	0.8 74.0*	240 -	1700°C, 2 hours	Y_2A,Y_3A_5	0.8 74.0*	310 1800
				Y_2SiAlO_5N,1600°C,direct sinter	Y_3A_5	0.8	280
YA,AD,No heat treatment	Amorphous	-0.6	2500				
YA,AD, 900°C, 2 hours	HexYA,OrthoYA Y_2A,Y_3A_5,Y_2O_3	0.9 9.5	350 300	Y_2SiAlO_5N,1100°C crystallisation of oxynitride glass	Y_2SiAlO_5N	0.6	1300

ND- Nitrate decomposition, AD alum decomposition, DS direct sinter, (see section 3.6.3) * = isotropic chemical shift.

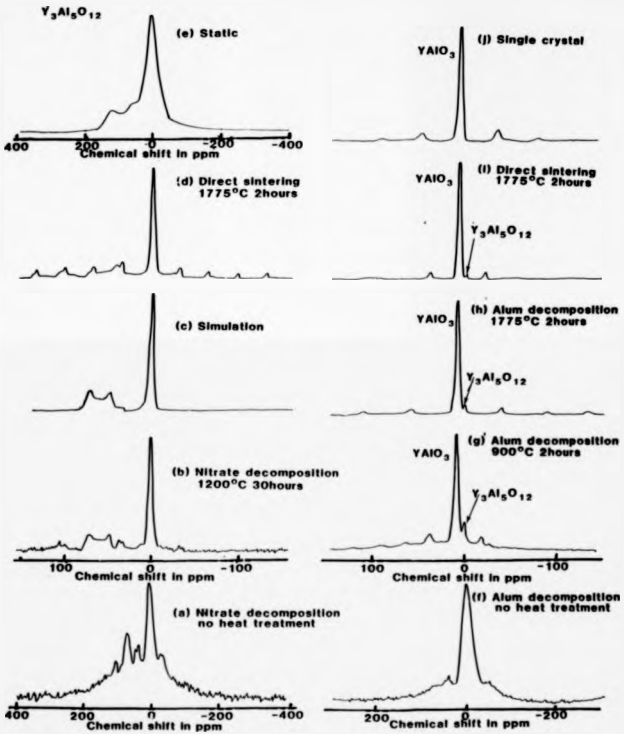

Figure5.2 Aluminium-27 spectra of yttrium aluminates ((a)-(e) $Y_3Al_5O_{12}$, (f)-(j) $YAlO_3$) prepared by different techniques (see text). (b), (c) B_0=9.4T. Simulation of isotropic lines η=0 C_q(tet)=6MHz and C_q(oct)=0.6MHz with 400Hz linebroadening and ratio AlO_4/AlO_6=1.5.

the magic angle can make interpretation more difficult as the higher-order transitions of the octahedral site narrow into a complex manifold of spinning sidebands, obscuring the tetrahedral site. Determination of the relative populations of the two aluminium environments by deconvolution of the spectra gives a ratio of 0.7±0.3 (AlO_4/AlO_6) which does not agree with the 1.5 from the crystal structure. This disagreement is to be expected when only ~75% of the aluminium is represented by the spectra, compared with α-Al_2O_3.

Single crystal NMR measurements on Y_3Al_5 have determined the quadrupolar interaction strength at the two sites, with a much larger efg at the tetrahedral site (e^2qQ/h = 6MHz, η=0) compared with the octahedral site (e^2qQ/h = 0.6MHz, η=0)[33]. The MAS-NMR spectra (Fig. 5.2(a)) clearly shows a broadened second-order quadrupole lineshape from the tetrahedral site. The separation of the singularities (~22ppm at B_0=9.4T) gives e^2qQ/h = (6.0±0.5)MHz, in agreement with the single crystal determination. Spectral simulation of the isotropic lines using the single crystal efg and η values and 400 Hz broadening satisfactorily fits the spectrum (Fig.5.2(c)). The quadrupolar lineshape allows determination of the isotropic shift for the AlO_4 unit (+74ppm) which is not possible from the featureless "near-Gaussian" lineshapes normally obtained. The decrease in the linewidth of the tetrahedral site (static → spinning) is in agreement with theory (Fig. 2.4(a)) for a line whose width is principally determined by second-order quadrupolar broadening. However, the resonance from the AlO_6 unit is considerably broader than can be accounted for by second-order quadrupolar broadening, as it should be 100 times narrower than the AlO_4 resonance, suggesting local distortions cause a range of efgs to be present increasing the linewidth. The small efg means the second-order quadrupolar shift of the peak position from the isotropic shift is only ~0.5ppm. A high

resolution NMR powder study of Y_3Al_5[5] in an applied magnetic field of 4.7T gave no shift for the AlO_4 unit as it could not clearly be resolved and its presence was only inferred from the asymmetry in the spinning sidebands of the AlO_6 resonance. Increasing the applied magnetic field to 9.4T improves the resolution by a factor of 4 compared to 4.7T which allows deconvolution of the spectrum. The AlO_4/AlO_6 ratio obtained implies the site with the larger efg has suffered the greater loss of signal.

5.3.2 $YAlO_3$ and Related Phases

At the YA composition complex phase mixtures resulted even at the highest sintering temperatures. Thermal decomposition of yttrium nitrate and ammonium alum was employed as the hexagonal YA was prepared via this route[31]. Immediately after thermal decomposition a disordered material is produced with the bulk of the aluminium in AlO_6 coordination (Fig. 5.2(f)). After only two hours at 900°C extensive crystallisation has occurred with XRD indicating Y_2O_3, orthorhombic YA, Y_3Al_5, Y_2A and some hexagonal YA have formed. MAS-NMR can detect signals from orthorhombic YA and Y_3Al_5 (Fig. 5.2(g)). After 2 hours at 1775°C only orthorhombic YA, Y_3Al_5 and Y_2A are present, with the level of YA increased (Fig. 5.2(h)). Direct sintering of the oxides at 1775°C for 2 hours produced a similar phase mixture of YA, Y_3Al_5 and Y_2A (Fig. 5.2(i)), to that from the alum decomposition at 1775°C. The shift of orthorhombic YA was unambiguously assigned as 9.4ppm from a single crystal sample of YA (Fig. 5.2(j)). Attempts to directly sinter the metastable $Y_2Si_3AlO_5N$ at 1600°C resulted in Y_3Al_5 being the dominant aluminium-containing phases. The ^{27}Al spectra of the metastable phase itself (Fig. 5.3(b)) formed by crystallisation of a nearby oxynitride glass, gave a resonance with a similar shift to Y_3Al_5 but the increased linewidth and XRD indicate that Y_3Al_5 is not

formed. The MAS-NMR signal from the metastable sample is produced by <10% of the total aluminium content when compared with α-Al_2O_3.

Single crystal measurements on orthorhombic YA have determined the quadrupole interaction strength as e^2qQ/h = 1.3MHz with η=0.2.[34] The 9.4ppm peak can unambiguously be assigned to the AlO_6 unit in YA and the FWHM ~350Hz is indicative of additional broadening, probably due to a range of distortions of the environment. The limited signal from the $YSiAlO_5N$ sample corresponds to an AlO_6 unit which must be from some minor phase that cannot be detected by other techniques. In Y_2SiAlO_5N aluminium is in an AlO_4 unit in three-membered rings but the quadrupole interaction must broaden the resonance beyond detection.

5.3.3 $Y_4Al_2O_9$ and Related Phases

Sintering a $2Y_2O_3$:Al_2O_3 mixture at 1775°C for 2 hours produced single phase Y_2A according to XRD (Fig. 5.3(a)). An MAS-NMR accumulation with 20µs deadtime produced a peak corresponding to an AlO_6 unit which could be matched to orthorhombic YA. The initial spectra were recorded on a Bruker WH-400 (B_1~2mT) and later ones were accumulated on a Bruker MSL-360 (B_1~5mT) which coupled with a shorter deadtime (~4µs) clearly reveals the presence of a much broader spectral component (Fig. 5.3(d)). The peak integrals show that the broad and narrow components account for 50% and 3% of the total aluminium content compared with α-Al_2O_3, with the rest undetected. Preparation of Y_2A by crystallisation of the nitrate decomposition product at 1200°C for 30 hours gave a complex mixture of Y_2A, orthorhombic YA and Y_3A_5 according to XRD with MAS-NMR (Fig. 5.3(c)) showing the presence of YA and Y_3A_5. The intermediate Y_4SiAlO_8N sample gave the major peak in the NMR spectrum at 113.5ppm which must be residual AlN even though XRD cannot detect its presence. There is some other structure on top of a broad component. Running the

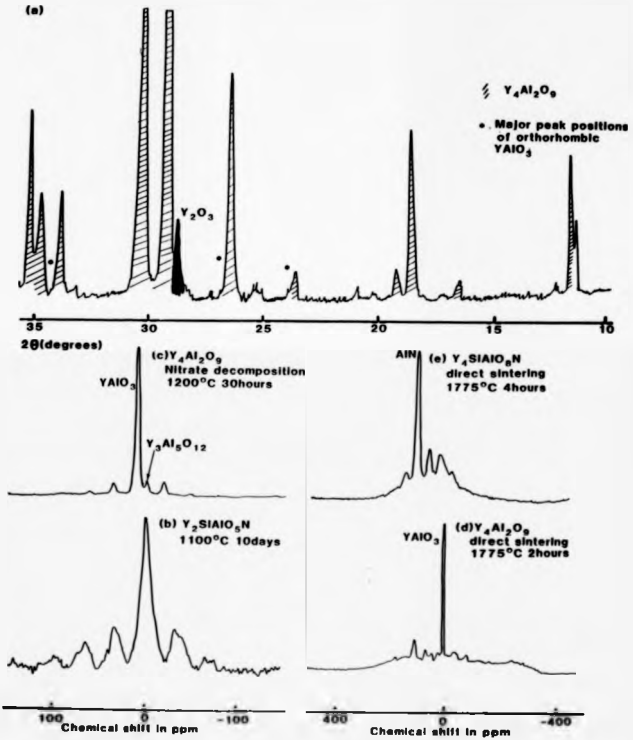

Figure8.3 (a) XRD powder pattern of $Y_4Al_2O_9$ composition directly sintered at 1775°C,2hours (CuKα,λ=0.154 nm).(b)-(e) Aluminium-27 spectra of yttrium aluminates and YSiAlON ceramics prepared by different techniques.

Y_4SiAlO_8N sample at 11.7T markedly increases the intensity of some of the narrow components (not shown) which emphasises that a large fraction of the aluminium nuclei can be missing from the NMR spectra.

The MAS-NMR spectra from Y_2A and Y_4SiAlO_8N clearly demonstrate both the strength and weakness of ^{27}Al for characterising solid-state samples. If the quadrupole interaction becomes too large no distinct resonance is apparent. This must be the case for the AlO_4 units in Y_2A and related phases where the quadrupole interaction strength probably exceeds 10MHz. No single crystal measurements of the quadrupole interaction strength or accurate bond length data could be located to confirm this. For phases with small quadrupole interactions (e.g. YA) very low levels can be observed which are undetected by other techniques such as XRD.

5.3.4 Phase Relationships of the Yttrium Aluminates

This study shows Y_3A_5 is the most stable phase and can be readily formed free from other phases. Y_2A and YA are also stable at 1775°C and although they cannot be formed as single phase products, the expected phase is dominant at a particular composition. There is no indication of preferential formation of Y_3A_5 independent of composition or that YA decomposes into Y_3A_5 and Y_2A at 1775°C, in agreement with the most recent phase equilibria work[27]. The decomposition of the soluble salts provides intimate mixing of the components as the salts precipitate out of solution. Initially an amorphous product forms which is confirmed by XRD and the increased linewidths of the MAS-NMR spectra. Crystallisation of this product forms the aluminates at temperatures where direct sintering of the oxides produces very little reaction, although the phase mixtures are more complex which may indicate that equilibrium has not been achieved in these samples.

5.4 The La_2O_3-Al_2O_3 System

Phase equilibrium of the La_2O_3-Al_2O_3 system is more straightforward than that of the Y_2O_3-Al_2O_3 system, with the formation of only two compounds, both of which are stable from their melting points to room temperature[35]. The 1:1 (La_2O_3:Al_2O_3) perovskite is almost cubic, although below ~(435±25)°C a small rhombohedral distortion occurs[36]. $LaAlO_3$ can be contrasted with YA which is orthorhombic, a trend often found in perovskites and similar orthoferrites, with the larger rare-earth ions giving less distorted compounds. No compounds form at the $2La_2O_3$:Al_2O_3 and $3La_2O_3$:$5Al_2O_3$ ratios found in the yttrium system. However, a β-alumina forms at approximately La_2O_3:$11Al_2O_3$, with a nominal composition $LaAl_{11}O_{(18-19)}$. The hexagonal β-alumina has a magnetoplumbite structure which is based on blocks of magnetite structure (Fe_3O_4) which in turn is related to the spinel structure, hence consists of ribbons of edge-sharing AlO_6 octahedra interconnected by AlO_4 tetrahedra. Single crystal XRD studies show three different AlO_6 environments, with the ratio AlO_6/AlO_4 ~4.3. The magnetite blocks are interconnected by distorted AlO_5 units (~2 per unit cell) and this variation of the occupancy of these sites which result in a range of composition for this compound[37].

A range of compositions from 2:1 (La_2O_3:Al_2O_3) to 1:11 were sintered for (2-3) hours at 1775°C, as well as attempts to make $LaAlO_3$ by the nitrate decomposition method (Sec. 3.6.3). The results of XRD and ^{27}Al MAS-NMR (Fig. 5.4) are compared in Table 5.3. The nitrate method initially gave an amorphous product with 2 environments, presumably AlO_6 and AlO_4, which was confirmed by spinning at different speeds and remaking the sample. Crystallisation of the amorphous decomposition product occurred after 3 hours at 400°C, which formed cubic $LaAlO_3$.

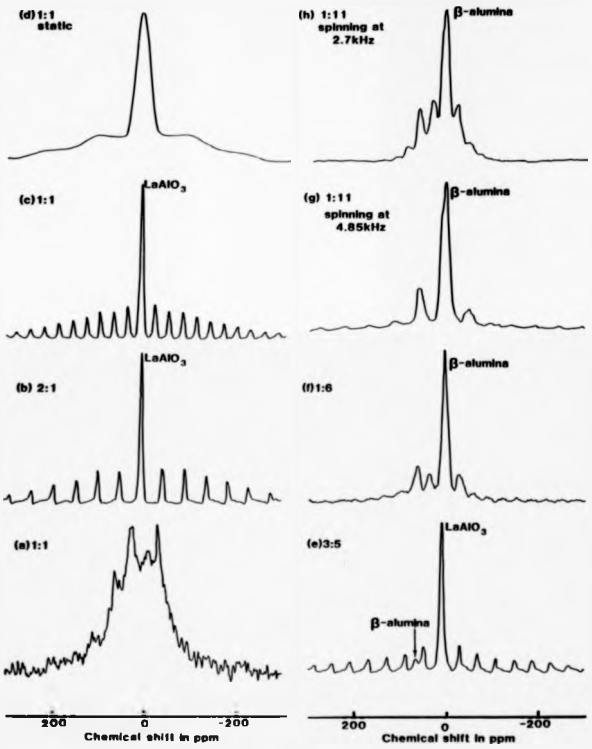

Figure 8.4 Aluminium-27 spectra of lanthanum aluminate mixtures(La:Al)from (a)nitrate decomposition prior to crystallisation and(b)-(h)direct sintering 1778°C,2hours

Table 5.3 Comparison of XRD and ^{27}Al MAS-NMR Characterisation of the La_2O_3-Al_2O_3 System

Sample	XRD	^{27}Al MAS-NMR	
		Peak position ppm ±0.5ppm wrt $[Al(H_2O)]^{3+}$	FWHM ±5% Hz
1:1 $La(NO_3)_3$:$Al(NO_3)_3$ decomposed, no heat treatment	Amorphous	~30 -27	2400 1600
400°C, 4 hours	$LaAlO_3$	11.9	390
2:1 La_2O_3:Al_2O_3 1775°C, 2 hours	$LaAlO_3$,La_2O_3	11.9	380
1:1 La_2O_3:Al_2O_3 1775°C, 2 hours	$LaAlO_3$	11.7	500
3:5 La_2O_3:Al_2O_3 1775°C, 2 hours	$LaAlO_3$,$LaAl_{11}O_{18}$	11.7 66	500
1:6 La_2O_3:Al_2O_3 1775°C, 2 hours	$LaAlO_3$,$LaAl_{11}O_{18}$	8.5 66	1200 1300
1:11 La_2O_3:Al_2O_3 1775°C, 2 hours	$LaAl_{11}O_{18}$	8.3 65	1200 1800

All direct sinterings at 1775°C produced only the two known crystalline phases, with their relative amounts changing as expected with composition.

XRD and ^{27}Al MAS-NMR generally agree on the phase content of the samples, although the different aspects measured by each technique have to be carefully taken into account. XRD depends on the structure factor which is dominated by the heavy, larger Z (atomic number) elements (e.g. lanthanum). $LaAlO_3$ and $LaAl_{11}O_{18}$ each have 1 lanthanum atom per formula unit so that XRD directly gives a reasonable measure of the amount of each phase present. However, the ^{27}Al NMR spectra depend on the aluminium content which is much higher in the β-alumina. For the La_2O_3:$6Al_2O_3$ mixture XRD indicates the expected ~1$LaAlO_3$:1$LaAl_{11}O_{18}$ from its stoichiometry midway between the two phases. The ^{27}Al MAS-NMR spectrum of this composition (Fig. 5.4(f)) is dominated by β-alumina, and $LaAlO_3$ cannot be resolved, which demonstrates that ^{27}Al MAS-NMR can be misleading if the two phases have markedly different aluminium contents.

The aluminium coordination in $LaAlO_3$ is clearly octahedral from the peak position (11.7ppm). The near cubic symmetry of the crystal structure is reflected in the symmetric local environments in $LaAlO_3$ which creates only a small efg at the aluminium site. No second-order quadrupole structure of the central transition is observable but the efg is small enough that the first-order powder pattern of the higher-order transitions can be seen in the static spectrum (Fig. 5.4(d)). The quadrupole interaction strength, estimated from the higher-order transitions, is e^2qQ/h = (0.12±0.02)MHz. The difficulty in obtaining higher accuracy is that the broadening present prevents the higher-order lineshape being precisely defined. A previous single crystal NMR study[36] measured e^2qQ/h for $LaAlO_3$ as a function of temperature over the range

(100-300)K and found it decreased (e^2qQ/h=0.2 → 0.15MHz) with increasing temperature which agreed with the smoothly decreasing rhombohedral distortion of the structure. Integration of the static powder pattern gives the ratio of the intensities of higher-order transitions/central transition as 5/3 compared to the expected value of 8. This agrees with a greater loss of signal occurring from the first-order quadrupole broadened higher-order transitions compared to the second-order quadrupole broadened central transition. The small efg results in the higher-order transitions readily narrowing into an extensive manifold of spinning sidebands. These higher-order transition sidebands are always formed by $LaAlO_3$ compared with α-Al_2O_3 where only occasionally are broad sidebands from the higher-order transitions observed. This is a consequence of the larger quadrupole interaction in α-Al_2O_3 requiring increased accuracy/stability of the magic angle to achieve narrowing.

No NMR has previously been performed on lanthanum β-alumina. The similar sodium β-alumina ($NaAl_{11}O_{18}$) has had the MAS-NMR spectrum recorded, with two resonances at 9.0ppm and 68ppm[5,21]. $LaAl_{11}O_{18}$ also gives two resonances (Fig. 5.4(g),(h)), one at 8.5ppm which has some structure, and one at 68ppm. These can be compared to γ-Al_2O_3 which has a similar spinel-type structure with AlO_6 (8 ppm) and AlO_4 (70.5ppm). It is difficult to attribute the structure of the octahedral peak in $LaAl_{11}O_{18}$ since it could either be due to second-order quadrupole effects or be the peak positions of different AlO_6 sites which are known to be present from the crystal structure. Figures 5.4(g) and (h) demonstrate the advantages of spinning faster, with deconvolution of the intensities from the two sites easier in the specimen which was spun faster. Integration of the spectrum (Fig. 5.4(g)) gives the ratio (AlO_6/AlO_4)-(5.0±0.7) which can be compared with 4.1 from the crystal structure. This again demonstrates the general inaccuracy of quantitative ^{27}Al NMR, even when a comparable

fraction of the aluminium content is seen compared with α-Al_2O_3 (Table 5.1). The ratio being above the expected value could be due to the efg being small at some of the octahedral sites, so that excitation of the AlO_6 sites is more complete and consequently the loss of AlO_6 intensity is reduced. Some higher-order transition sidebands associated with the octahedral site are visible confirming the efg at some of the octahedral sites is relatively small. Additionally some AlO_5 intensity may be quadrupole-shifted down frequency into the octahedral region (cf andalusite) thereby contributing to the AlO_6 intensity. As the AlO_5 signal cannot be clearly observed the various structural models based on the occupancy of the AlO_5 sites cannot be distinguished by these spectra.

5.5. Non-Stoichiometric Spinels $MgO.xAl_2O_3$

Spinel may be regarded as an FCC structure of 32 oxygen ions per unit cell. In stoichiometric spinel ($MgO.Al_2O_3$) 8 magnesium ions occupy (1/8) of the 64 tetrahedral interstitial sites, while the 16 aluminium ions occupy (1/2) of the 32 octahedral sites per unit cell. Ribbons of edge-sharing AlO_6 units are interconnected by MgO_4 tetrahedra. Despite the relatively simple structure of an AB_2O_4 spinel, complex disordering phenomena can occur over the cation sites which has important thermochemical and physical consequences[38]. This disorder varies between the limiting cases of the "normal" distribution $(A)_{Tet}(B_2)_{Oct}O_4$ with all the B cations on octahedral sites and the "inverse" distribution $(B)_{Tet}(AB)_{Oct}O_4$ with the B cations divided equally between octahedral and tetrahedral sites. The disorder is characterised by an inversion parameter, i, which is the fraction of the tetrahedral sites occupied by the B cations and has values 0(normal), 2/3(random) and 1(inverse).

The basic spinel structure has been known for some time but study of the cation distribution by XRD refinement was hampered by the similar X-ray scattering factors of Mg^{2+} and Al^{3+} ions.[39] An indirect method using the ESR spectra from natural and synthetic spinels with low levels of Cr^{3+} substitution for Al^{3+} has been applied. Different next nearest neighbours produce distinct ESR lines and the stoichiometry allows the inversion parameter to be calculated[40]. The ESR study gave a small inversion parameter (0.05) for a natural spinel although this steadily increased with temperature to ~0.3 at 900°C. Recently two ^{27}Al MAS-NMR studies[41,42] have examined the aluminium distribution since the quantitative signals for the well resolved AlO_4 and AlO_6 environments allow it to be readily determined. For a natural spinel one study[41] gave an inversion parameter of (0.12±0.06) with a much higher degree of inversion (0.36±0.03) in a magnesium aluminate sintered directly at 1400°C. A more extensive range of annealing temperatures was used in the other study[42] and essentially the same results were obtained, with the inversion parameter increasing steadily with temperature, reaching a plateau i ~0.4 at 900°C, similar to the ESR study. The plateau is believed to be due to the inability to quench in any higher disorder from above this temperature. Both NMR studies were aware of the problems of quantitative ^{27}Al NMR and claimed that all the aluminium was present in the spectra within experimental error, although the "standard" used was not given. No attempts were made to measure the ^{25}Mg resonance which would provide a check on the inversion parameter obtained from the ^{27}Al NMR spectra.

For magnesium aluminate spinels the composition may be varied, with a solid solution range ($MgO.xAl_2O_3$ $0 \leq x \leq 4$) existing at elevated temperatures[39]. For these non-stoichiometric compositions Al^{3+} ions replace Mg^{2+} ions and to maintain charge neutrality cation vacancies

are formed. An X-ray analysis of non-stoichiometric spinels[39] indicated the vacancies predominantly form on the octahedral sites. NMR can probe the cation distribution in non-stoichiometric spinels.

In this work four compositions were examined, with x=1 a natural spinel, x=1.38 a polycrystalline sample produced by solid-state sintering of the oxides and the other two specimens (x=2.1, 3.4) single crystals grown by the Verneuil technique. Energy dispersive X-ray analysis was used to determine the Al_2O_3/MgO ratio. The natural spinel gave one resonance (Fig.5.5(a), x=1) and no inversion could be detected within experimental error with only spinning sidebands flanking the main octahedral peak. The non-stoichiometric spinels (Fig. 5.5(a)) show two peaks at 9ppm and 68ppm confirming that both octahedrally and tetrahedrally coordinated aluminium are present. To calculate the amount of each environment the spectra were deconvolved. Gaussian curve-fitting gave poor results due to the distinctly asymmetric lineshapes caused by second-order quadrupolar linebroadening. A screen integration determined the spectral intensity of the octahedral and tetrahedral sites, including the associated sidebands. The overlap of tetrahedral and octahedral sidebands at -40ppm (Fig. 5.5(a)) was accounted for by assuming equality of the sidebands either side of their respective peaks. The relative uncertainty in the AlO_6/AlO_4 ratio for the x=1.38 sample is higher than for other samples since the second sideband of the octahedral peak overlaps the main tetrahedral peak, making a significant contribution to the area and has to be subtracted to obtain the true intensity of the tetrahedral site. The error in the ratio AlO_6/AlO_4 obtained from integration ~10%. Comparison with α-Al_2O_3 shows that a comparable amount of aluminium is seen from the natural spinel (Table 5.1) but this is reduced in the non-stoichiometric spinel to ~0.9, indicative of a decrease in the

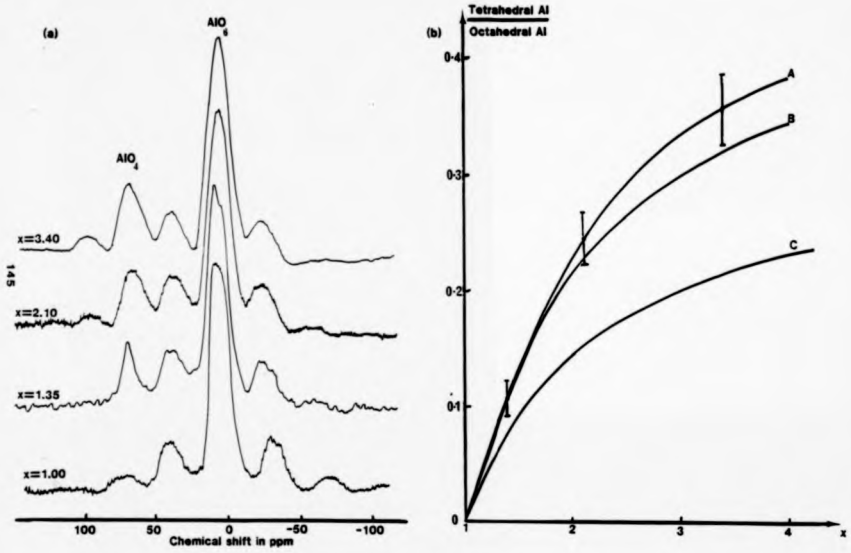

Figure 5.5 (a) Aluminium-27 spectra of spinels $MgO.xAl_2O_3$.(b) Ratio of tetrahedral to octahedral aluminium for vacancies on octahedral sites(A),randomly distributed(B)and on tetrahedral sites(C)compared to experiment.

local symmetry. Compared to stoichiometric spinel the number of variables has increased with magnesium, aluminium and vacancies being distributed over the cation sites. Hence either some assumptions have to be made or additional information is required, which ^{25}Mg NMR could provide. The stoichiometric spinel gave a single ^{25}Mg resonance (Sec. 6.2) confirming that the natural spinel is normal. Unfortunately all attempts to obtain ^{25}Mg spectra from non-stoichiometric spinels resulted in no signal. ^{25}Mg is more sensitive to local distortions than ^{27}Al and the lack of ^{25}Mg NMR signal confirms that the non-stoichiometric spinels are more distorted than the natural spinel.

To examine the vacancy distribution three schemes can be envisaged with vacancies either on octahedral sites (scheme A), randomly distributed (scheme B) or on tetrahedral sites (scheme C). For each occupancy scheme the number of aluminiums in tetrahedral and octahedral sites can be calculated by considering n units of ($MgO.xAl_2O_3$) per unit cell. n may be deduced from the condition that 32 oxygens ions are required per unit cell to form the basic FCC structure [Eq. 5.1].

$$n = 32/(3x+1) \qquad [5.1]$$

n is also the number of magnesium ions per unit cell. Making the assumptions that the distribution of vacancies and cations occurs over the cation sites normally occupied in the stoichiometric spinel, and that magnesium ions occupy tetrahedral sites only (from the stoichiometric spinel here i=0), t tetrahedral sites remain unoccupied, where

$$t = 24(x-1)/(3x+1) \qquad [5.2]$$

The number of aluminium ions per unit cell is 2nx. The distribution of the aluminium ions amongst the octahedral and remaining tetrahedral sites may be written down as a function of x for the three occupancy schemes [Eqs. 5.3-5.5]. The ratios, R, relate the

vacancy occupation to the aluminium occupation which are shown as a function of x (Fig. 5.5(b)).

$$A,\quad R_A = \frac{\text{Tetrahedral}(AlO_4)}{\text{Octahedral}(AlO_6)} = 3(x-1)/(5x+3) \qquad [5.3]$$

$$B,\quad R_B = 3(x-1)/2(3x+1) \qquad [5.4]$$

$$C,\quad R_C = (x-1)/(3x+1) \qquad [5.5]$$

The NMR evidence is consistent with the cation vacancies predominantly forming on octahedral sites, with scheme A favoured. This is compatible with the X-ray evidence[39]. The inversion parameter has previously been measured using the ESR technique in a non-stoichiometric spinel (x=1.5) which gave a value for i=0.6±0.15. Converting the ratio R into an inversion parameter for aluminium gives i_A=0.65, i_B=0.55, i_C=0.37 and i_{exp}(=0.64±0.07), at x=1.4. The experimental value obtained here clearly agrees with the ESR value. However, the ratio R depends on the assumption that magnesium occupies only tetrahedral sites since no independent evidence can be obtained about its distribution. Unlike stoichiometric spinels measurement of the aluminium inversion parameter does not define the magnesium inversion. Any scheme consistent with the aluminium distribution determined by MAS-NMR and with the bulk of the vacancies on octahedral sites means in these non-stoichiometric spinels the magnesium inversion is lower than in the stoichiometric sintered spinels in the previous MAS-NMR studies[41,42].

In γ-Al_2O_3 which has a defective spinel structure, it was found that all the vacancies are located on tetrahedral sites[43] in contrast with the non-stoichiometric spinels. A thermochemical study of the $MgAl_2O_4$-$Al_{8/3}O_4$ series concluded that the stable cation distribution for defective spinels are primarily determined by energetic considerations[38]. The interactions between various cations and vacancies lead to distributions which are separated by

small energy differences as the stable vacancy distributions change markedly with composition.

5.6 ALON and Sialon Phases

To date most high resolution solid-state ^{27}Al studies have concentrated on materials where aluminium is solely coordinated by oxygen. In the study of oxynitride ceramics extension of the range of coordinations to AlO_xN_{4-x} ($0 \leq x \leq 4$) tetrahedra occurs although it is expected that mixed units (i.e. x=1,2,3) will have large quadrupole interactions (Sec. 5.2) which will make the resonance broad. AlN provides a useful reference since it is tetrahedrally coordinated by only nitrogen in the wurtzite structure. Addition of oxygen to AlN causes a local charge imbalance which is removed by changing the coordination of some of the aluminium from 4 to 6. In the AlN rich corner of the Si-Al-O-N system the complex series of polytypoids exist (Fig. 1.2) which have the wurtzite structure modulated by layers of AlO_6 units to allow charge compensation. Those layers adjacent to the AlO_6 layers are believed to consist of $(Si,Al)O_3N$ tetrahedra with all other tetrahedral coordinations $(Si,Al)N_4$. Addition of nitrogen to γ-Al_2O_3 inhibits its high temperature transformation to α-Al_2O_3 as the mixed tetrahedral/octahedral structure of γ-Al_2O_3 can accommodate nitrogen, whereas the presence of nitrogen in α-Al_2O_3, which contains only octahedra, would lead to local charge imbalance. The range of compositional stability of this aluminium oxynitride phase (ALON) has been thoroughly investigated at high temperatures (>1700°C) and is centred on 35.7mol% AlN ($Al_{23}O_{27}N_5$)[44]. The structure is identical to spinel with 32 cations and 23 anions (i.e. 1 anion vacancy) per unit cell, so that some of the local aluminium coordinations have to be mixed. The other sialon phases are arrangements of $(Si,Al)(O,N)_4$ tetrahedra (Sec. 4.2.2). The general crystal structures of these

phases are known but local coordination models have not been formulated because of the difficulty in distinguishing elements with similar scattering factors (e.g. Si/Al and O/N).

Aluminium nitride gives a single resonance at 113ppm (Fig. 5.6(a)) which corresponds to an AlN_4 unit. In the oxynitrides to emphasise the narrow spectral features when broad backgrounds are present, the first 20μs of the time domain signal are removed. In the polytypes 21R (not shown) and 15R (Fig. 5.6(b)) two distinct resonances are apparent. In both cases the major peak is at ~112ppm, with a much smaller octahedral peak at ~10ppm. Spectral integration reveals that only 30% of the aluminium (compared to α-Al_2O_3) is represented by these spectra (including the broad components). Although the AlO_6/AlN_4 ratio obtained from the spectrum is close to the value expected from a model of the structure, no reliance should be placed on the experimental ratio since only a fraction of the total aluminium is observed. However, these spectra clearly demonstrate that the structural model which requires both octahedrally and tetrahedrally coordinated aluminium is correct. The ^{29}Si spectrum for 15R (Fig 4.3(f)) suggests that silicon is coordinated by nitrogen only, so that aluminium is expected in both $AlON_3$ and AlN_4 environments. The similarity of the shift at 112ppm to AlN allows this resonance to be assigned to AlN_4 units. The absence of any distinct resonance from $AlON_3$ tetrahedra suggests that the mixed tetrahedral units have been quadrupole broadened beyond detection.

In ALON it is expected that a range of local tetrahedral and octahedral environments for aluminium will be present, including mixed anion (i.e. oxygen and nitrogen) environments. Direct solid-state sintering of various compositions of AlN and γ-Al_2O_3, close to $5AlN:9Al_2O_3$, under a flowing oxygen-free nitrogen atmosphere at 1775°C for 3 hours produced almost single phase ALON, according to XRD, with

minor levels of the residual reactants. A typical NMR spectrum (Fig. 5.6(c)) shows three distinct resonances 114ppm, 65ppm and 12ppm. These could be conveniently ascribed to AlN_4, AlO_4 and AlO_6 environments expected in ALON but the close agreement of the peak positions with those of the reactants suggest they could be the source. The spectra can only account for ~40% of the total aluminium content compared to α-Al_2O_3, so that the narrow spectral features can account for only a small fraction of the total aluminium content. As not all the aluminium nuclei contribute to the MAS-NMR spectrum the various possibilities of oxygen-nitrogen ordering cannot be distinguished. However, for all schemes (i.e. from strictly partitioned AlO_4, AlN_4 ordering to a purely random distribution) AlO_4 tetrahedra would be dominant over AlN_4 tetrahedra. For a random distribution ~40% of the aluminium would be coordinated by oxygen only with a negligible fraction coordinated solely by nitrogen. Hence all the recorded signal could be attributed to local environments of single species nearest neighbours and the peak at 114ppm may be assigned to AlN, estimated to be ~5% of the total aluminium content, which is just detectable by XRD. As γ-Al_2O_3 and ALON are isostructural it is probable that AlO_4 resonances from both are coincident. It appears that only resonances corresponding to single species environments (i.e. AlN_4, AlO_4, AlO_6) are observable.

α'-sialon, which is based on α-Si_3N_4, has a range of solid solubility with Al/Si and O/N substitution, with the sample used in this study having an approximate composition $Y_{0.6}Si_9Al_3ON_{15}$. It is a nitrogen-rich material and the ^{27}Al resonance at ~102ppm (Fig. 6.5(d)) can be attributed to a purely nitrided environment. As all the silicon is in an SiN_4 environment some of the aluminium would be expected to be in mixed environments (e.g. $AlON_3$). There is no evidence for even a minor secondary resonance which suggests that the

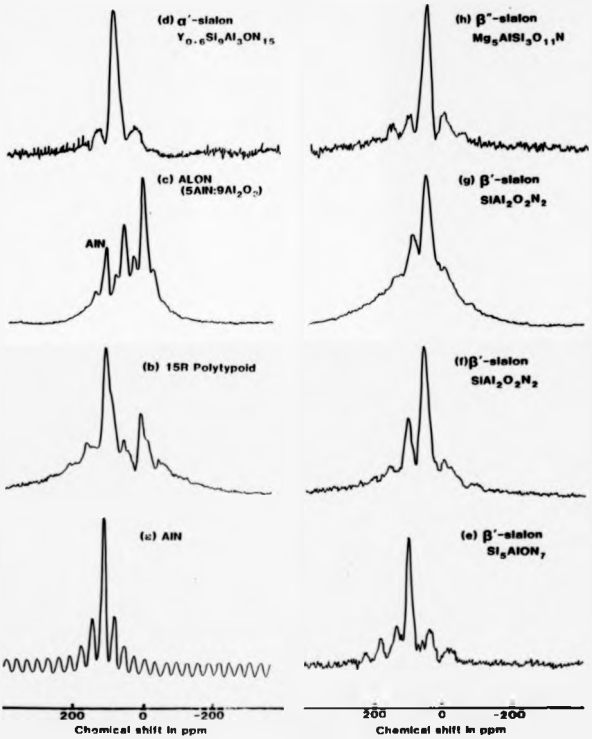

Figure 8.6 Aluminium-27 spectra of oxynitride ceramic phases. (b),(d),(e),(f),(h) have had the initial(15-20)μs of the time domain signal removed to remove the broad spectral components.

$AlON_3$ units make up part of the undetected signal.

The β'-sialon solid solution ($Si_{3-x}Al_xO_xN_{4-x}$) allows extensive aluminium and oxygen substitution into the β-Si_3N_4 structure. The ^{27}Al NMR spectra show some narrow components on top of a much broader component (Fig. 5.6(g)). The amount of aluminium represented by these spectra decreases from ~50% (x=2) to ~10% (x=0.5) of the total aluminium content compared to α-Al_2O_3. The narrow components (Fig. 5.6(e)),(f)) represent a relatively small fraction of the total aluminium content. However, the spectra do indicate that there are two relatively symmetric environments in these materials which cannot be assigned to the reactants but are probably AlN_4 (103ppm) and AlO_4 (67ppm) environments in β'-sialon. As x increases the dominant AlN_4 peak for x=0.5 becomes the minor peak relative to AlO_4 at x=2. There is a small increase in the shift of the AlN_4 peak position (103ppm → 109ppm) with increasing x. In the x=2 sample a small, reproducible peak occurs at ~4ppm which corresponds to an AlO_6 unit. This peak may be explained either as a low level impurity phase, or at high oxygen substitution levels there is a tendency for aluminium to go into an octahedral coordination. In β''-sialon (Fig. 5.6(h)) the only narrow component has a shift of 67ppm, consistant with AlO_4 units expected from the oxygen-rich composition of this phase.

Previous structural studies of β'-sialon by infra-red spectroscopy[45,46] and neutron diffraction[47,48] have demonstrated that β'-sialon has the same crystal structure as β-Si_3N_4, but have been able to say little about the local coordination changes across this series. As both ^{29}Si and ^{27}Al NMR have been performed a model for the local structure can now be proposed. The ^{29}Si resonance shift position shows very little change with composition, indicating that the silicon remains in a SiN_4 environment throughout (Sec. 4.3). The gradual increase in the width of the ^{29}Si resonance with increasing x

(FWHM=210Hz(x=0.5) → 400Hz(x=2)) is indicative of an increase in the "disorder" about the silicon environment with increasing x. ^{27}Al NMR shows a distinct change of the number of AlN_4 and AlO_4 environments with x. Unfortunately, the ^{27}Al spectra can say nothing about the mixed environments (e.g. AlO_3N) as they cannot be detected, presumably due to extensive quadrupolar broadening.

A structural model constrained by the NMR results allows silicon to be only in SiN_4 coordination, while the aluminium has a range of coordinations AlO_xN_{4-x} ($0 \leq x \leq 4$), with at x=2 AlO_4 dominant over AlN_4 and vice-versa at x=0.5. A purely random model is clearly not feasible as both silicon and aluminium local environments would be dominated by mixed local coordinations. This is not the case for silicon and even for aluminium where mixed local coordinations probably exist the number of AlO_4 units would not be expected to exceed the number of AlN_4 units. This suggests a more ordered model, which is in fact generally implicit in these materials. If aluminium accepts a lone pair of p-electrons, as in aluminosilicates, it will be isoelectronic with silicon. Oxygen in a trigonal planar bonding arrangement can donate one of its lone pairs so that it is isoelectronic with nitrogen. This associated substitution is suggested as equal numbers of aluminium and oxygen atoms enter the system and by the similarity of the Al-O and Si-N bond lengths (~0.175nm). A microdomain-type structure is probable of which a layered variation is favoured (Fig. 5.7) by analogy with the isostructural materials phenacite (Be_2SiO_4), willemite (Zn_2SiO_4) and β'-sialon all of which have layered structures. The similarity of the constituent elements scattering factors make it unlikely that other techniques can detect this ordered site selection. NMR can only determine the local structure so that the periodicity along the c-axis (Fig. 5.7) is arbitrary in our NMR model. Variations in composition are accommodated by changing the block dimensions with the thickness

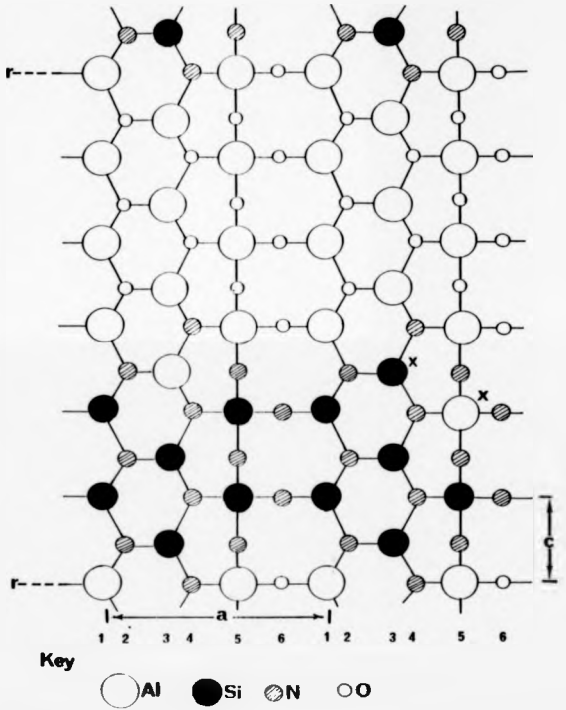

Figure5.7 Schematic representation of a possible structure for x=2 β'-sialon,consistent with the MAS-NMR data.Atoms in columns 1,4 and 6 are above the plane of the paper,3 below with 2and 5 in the plane. The planes of atoms carry on in the same form perpendicular to the paper and parallel to 'a' with the repeat unit along 'c' between the lines r,X are defects within the layers.

of the aluminium region increasing relative to the silicon layer with increasing x. This explains the increase in the amount of aluminium signal with increasing x since as the block width increases the "strain" in the aluminium layer will decrease. In contrast, the silicon layer decreases in width with increasing x which can increase the range of environments (e.g. bond lengths and next nearest neighbours) leading to the increased ^{29}Si resonance linewidth. This demonstrates that ^{27}Al NMR can provide useful structural information, although the problem of "missing" signal intensity should always be carefully considered.

5.7 General Discussion of ^{27}Al NMR of Ceramics

These ^{27}Al NMR results have two general features. There is the obvious advantage of straightforward qualitative identification of the local structural units present, but there is the drawback that the spectra may only represent a small fraction of the total aluminium content, which can lead to a misleading impression of the aluminium distribution.

Provided the efg is sufficiently small to allow excitation and narrowing of the resonance, the distinct shift ranges for AlO_6, AlO_4 and AlN_4 units allow the local coordination of aluminium to be identified (Table 5.4). The positive chemical shift of AlN_4 units relative to AlO_4 units parallel the shift trend for ^{29}Si. The more covalent Al-N bond gives a more paramagnetic ^{27}Al chemical shift than the Al-O bond. The ^{27}Al chemical shifts in AlN and the polytypoids (>112ppm) are distinctly different from those of α' and β'-sialon (~105ppm) even though they are all assigned to AlN_4 units. If quadrupole effects are comparable (which the linewidths suggest they are) the difference in the peak positions will be a chemical shift effect, with the former group having the more covalent bonds. In AlN

Table 5.4 ^{27}Al MAS-NMR Peak Positions at a Magnetic Field of 8.45T from Ceramic Phases

Material	Aluminium coordination	Peak position ppm ± 1 ppm wrt $[Al(H_2O)_6]^{3+}$
α-Al_2O_3	Face-sharing AlO_6	11.5
γ-Al_2O_3	Chains of edge-sharing AlO_6 units connected by sharing corners with AlO_4 tetrahedra.	8 68
$YAlO_3$	Corner-sharing AlO_6	9.4
$Y_3Al_5O_{12}$	Isolated AlO_6 interconnected by corner-sharing with AlO_4 units.	0.8 74*
$LaAlO_3$	Corner-sharing AlO_6	11.7
$LaAl_{11}O_{18}$	AlO_6 } As γ-Al_2O_3 AlO_4 }	8.5 66
$MgO.xAl_2O_3$	AlO_6 } As γ-Al_2O_3 AlO_4 } with MgO_4 substitution	9 68
β''-sialon	Corner-sharing AlO_4	67
β'-sialon	Corner-sharing AlO_4 Corner-sharing AlN_4	68 ~105
α'-sialon	Corner-sharing AlN_4	102
Polytypoid	Corner-sharing AlO_6 Corner-sharing AlN_4	~10 112
AlN	Corner-sharing AlN_4	113

* Isotropic chemical shift

and the polytypoids the nitrogen is tetrahedrally coordinated, so is sp^3-hybridised whereas in the sialons it is trigonally bonded, and is therefore sp^2-hybridised. Hence the more positively shifted group has the greater p-character in the bonds as expected. For AlO_4 units no distinction between units with differing connectivities and next nearest neighbours is apparent. Materials with similar structures give almost coincident chemical shifts, being exemplified by the AlO_4 units in γ-Al_2O_3, $MgO.xAl_2O_3$ and $LaAl_{11}O_{18}$ at (70.5-68)ppm.

Similarly the AlO_6 units in these materials, γ-Al_2O_3, $MgO.xAl_2O_3$ and $LaAl_{11}O_{18}$ are clustered about one value ~8ppm. The chemical shift dispersion of AlO_6 units (<20ppm) means that although the chemical shift scale suggested for different AlO_6 connectivities[5] cannot be denied, the ability to assign a particular connectivity given the peak position is doubtful. The results for $Y_3Al_5O_{12}$ (~0.8ppm, isolated AlO_6) and $YAlO_3$ (~9.4ppm, corner-sharing AlO_6) agree with this trend to more paramagnetic shifts with increasing connectivity, while the chemical shifts of $LaAlO_3$ (11.7ppm, corner-sharing AlO_6) and $LaAl_{11}O_{18}$ (8ppm, edge sharing AlO_6) does not.

The peak characteristics (i.e. position and width) allow phase identification by matching the resonances in spectra from complex phase mixtures, to the known resonances of phases that are likely to be present. This was demonstrated by the unambiguous identification of $Y_3Al_5O_{12}$ and $YAlO_3$ in complex phase mixtures of the yttrium aluminates.

More revealing than the observed chemical shifts are the resonances which could not be detected. The results here show that signal intensity is "lost" to some extent from all ^{27}Al spectra of solid-state specimens which essentially removes the quantitative advantage of the NMR technique. $Y_4Al_2O_9$ gave a prominent octahedral resonance which would have led to an incorrect coordination

determination if the structure had not already been known and a check on the level of aluminium represented by the spectrum had not been made. Hence some estimate of the loss of aluminium from the recorded signal should always be made especially if the local coordination in the sample is ill-defined. The absence of a resonance indicates that the local distortion is such that quadrupolar broadening prevents detection. In $Y_4Al_2O_9$ the aluminium is in a Q^1 AlO_4 unit, so that one bond is different from the other three in the tetrahedron and this can give rise to a large quadrupole interaction. As the variation of the bonds increases the quadrupole broadening effects will increase. This effect is expected to be most pronounced when changes in the nearest neighbour occur. The efgs that are anticipated in these mixed units are likely to make their detection in pulsed, high resolution NMR in the currently available magnetic fields difficult. This is confirmed by the spectra from the sialons, polytypoids and ALON whose structures all contain mixed AlO_xN_{4-x} (x=1,2,3) units but no resonances could be detected from these units. The excitation and intensity problems in ^{27}Al NMR spectra are obviously linked to the quadrupole interaction, although the actual mechanism which determines the signal intensity is unclear.

References: Chapter 5

1. Muller, D., Gessner, W., Behrens, H.J. and Scheler, G., Chem. Phys. Lett. 79, 1981, 59-62.
2. Muller, D., Gessner, W., Samoson, A., Lippmaa, E. and Scheler, G., Polyhedron 5, 1986, 779-785.
3. Lippmaa, E., Samoson, A. and Magi, M., J. Am. Chem. Soc. 108, 1986, 1730-1735.
4. Cruickshank, M.C., Dent-Glasser, L.S., Barri, S.A.I. and Poplett, I.J.F., J. Chem. Soc., Chem. Commun. 1986, 23-24.
5. De Jong, B.H.W.S., Schramm, C.M. and Parziale, V.G., Geochim. Cosmochim. Acta., 47, 1983, 1223-1236.
6. Muller, D., Gessner, W. and Scheler, G., Polyhedron, 2, 1983, 1195-1198.
7. Kundla, E., EESTI/NSV Tea. Akad. 34, 1985, 68076.
8. Samoson, A., Chem. Phys. Lett, 119, 1985, 29-32.
9. Muller, D., Gessner, W., Samoson, A., Lippmaa, E. and Scheler, G., J. Chem. Soc. Dalton Trans. 1986, 1277-1281.
10. Lowenstein, W., Am. Mineral., 39, 1954, 92-96.
11. Muller, D., Berger, G., Grunze, I. and Ladwig, G., Phys. Chem. Glasses. 24, 1983, 37-42.
12. Dupree, R., Holland, D., and Williams, D.S., Phys. Chem. Glasses 26, 1985, 50-52.
13. Muller, D., Jahn, E., Ladwig, G., Haubenreisser, U., chem. Phys. Lett. 109, 1984, 332-336.
14. Bloembergen, N. in "Conference on Defects in Crystalline Solids:Report", Phys. Soc. 1954.
15. Abragam, A., "Principles of Nuclear Magnetism", OUP, 1961.
16. Watkins, G.D. and Pound, R.V., Phys. Rev. 89, 1953, 658.
17. Von Lampe, F.V., Muller, D., Gessner, W., Grimmer, A.-R and Scheler, G., Z. Anorg. Allag. chem. 489, 1982, 16-22.
18. Sanz, J. and Serratosa, J.M., J. Am. Chem. Soc. 106, 1984, 4790-4793.
19. Hallas, E. and Mahnert, M., Crystal. Res. Technol. 20, 1985, (25-28).
20. Kirkpatrick, R.J., Oestrike, R., Weiss, G.A., Smith, K.A. and Oldfield, E., Am. Mineral. 71, 1986, 705-711.
21. Kinsey, R.A., Ph.D. Thesis, Univeristy of Illinois, Urbana 1984.
22. Zax, D.B., Bielecki, A., Pines, A. and Sinton, S.W., Nature, 312, 1984, 351-352.
23. Pound, R.V., Phys. Rev., 79, 1950, 685-702.
24. Fenkze, D., Freude, D., Frolich, T. and Haase, J., Chem. Phys. Lett. 111, 1984, 171-175.
25. Valiyev, K.A. and Zripov, M.M., Zh. Strukt, Khim. 7, 1966, 494-503.
26. Delpeuch, J.J., in "NMR of Newly Accessible Nuclei: Volum 2", Ed. Laszlo, P. Academic Press, 1983, 153-196.
27. Cockayne, B., J. Less Common Metals, 114, 1985, 199-206.
28. Toropov, N.A. Bondar, I.A., Galadhov, F.V., Nikogasyan, K.S. and Vinogradov, N.V. I. Akad. Nauk. SSSR. Ser. Khim. 7, 1969, 1158-1163.
29. Brandle, C.D. and Steinfink, H., Inorg. Chem. 1969, 1320-1324.

30. Euler, F. and Bruce, J.A. Acta. Cryst. 19, 1965, 971-978.
31. Bertaut, F. and Mareschal, J., Comp. Rend. Acad. Sci. Paris, 257, 1963, 867-870.
32. Morgan, P.E.D., Carroll, P.J. and Lange, F.F. Mat. Res. Bull. 12, 1977, 251-260.
33. Broq, E.C., Jones, W.H. and Verber, C.M., Phys. Lett. 20, 1966, 258-260.
34. Grochulski, T. and Zbieranowski, W., in "Magnetic Resonance and Related Phenomena", Ed. Kundla, E., Lippmaa, E. and Saluvere, T., 1979, 973.
35. Bondar, I.A. and Vinogradova, N.V., Fig. 2340 in "Phase Diagrams for Ceramists", Ed. Levin, E.M., Robbins, C.E. and McMurdie, H.F., Pub. Am. Ceram. Soc. 1969.
36. Muller, K.A., Brun, C., Derighetti, B., Drumheller, J.G. and Waldner, F., Phys. Lett. 9, 1964, 223-224.
37. Iyi, N., Inoue, Z., Takekawa, S. and Kimura, S., J. Sol. St. Chem. 54, 1984, 70-77.
38. Navrotsky, A., Wechsler, B.A., Geisinger, K. and Siefert, F., J. Am. Soc. 69, 1986, 418-422.
39. Jagodzinski, V.H. and Saalfeld, H., Z. fur Krist. 110, 1958, 197-210.
40. Schmocker, U. and Waldner, F., J. Phys. C. 9, 1976, L(235-237).
41. Gobbi, G.C., Christoffersen, R., Otten, M.T., Miner, B., Buseck, P.R., Kennedy, G.J. and Fyfe, C.A., Chem. Lett., 1985, 771-774.
42. Wood, B.J., Kirkpatrick, R.J. and Montez, B., Am. Mineral, 71, 1986, 999-1006.
43. Dupree, R., Farnan, I., Forty, A.J., El-Mashri, S. and Bottyan, L., J. Phys. Colloq. C8, 1985, 113-117.
44. McCauley, J.W. and Corbin, N.D., J. Am. Ceram. Soc. 62, 1976, 476-479.
45. Wild, S., Elliott, H. and Thompson, D.P., J. Mater. Sci. 13, 1978, 1769-1775.
46. Takase, A., Umebayaski, S. and Kishi, K., Jap. J. Appl. Phys. 21, 1982, 1447-1452.
47. Gilliot, L, Cowlam, N. and Bacon, G.E., J. Mater. Sci. 16, 1981, 2263-2268.
48. Roult, G., Braissart, M., Labbe, J.C. and Goursat, P., in "Non-oxide Technical and Engineering Ceramics", Ed. Hampshire, S., Elsevier Applied Science, 1986, 191-201.

CHAPTER 6. NMR OF OTHER NUCLEI

The other NMR-active nuclei present in the ceramics of this study, besides ^{29}Si and ^{27}Al, could further constrain the local atomic arrangements. Solid-state NMR of these other nuclei is much less common (Sec.1.3) and in this chapter the results of preliminary investigations of their likely utility in high resolution NMR of ceramics will be presented.

6.1 Nitrogen-14

In oxynitride ceramics nitrogen NMR is attractive since many of the different structures depend on the role of nitrogen, so its direct investigation would be useful. An obvious example is $LaSi_3N_5$, where nitrogen has two distinct coordinations (Sec. 4.3.4). Nitrogen-15 being spin-$\frac{1}{2}$, would be ideal except its low sensitivity (Sec. 1.3) rules it out in these materials where techniques such as cross-polarisation cannot be used to enhance the signal intensity. Nitrogen-14 is a spin-1 nucleus, so that both its transitions are first-order quadrupole broadened in common with the non-central transitions (e.g. $\frac{1}{2} \leftrightarrow 3/2$) from half-integer spin nuclei. In α-Al_2O_3 spinning sidebands from such transitions are only occasionally observed when the magic angle is accurately set and similar requirements will be necessary to observe any sidebands in ^{14}N spectra.

Initially static spectra were accumulated using a commercial Bruker static probe. To determine the spectrometer conditions and set the shift reference, a spectrum of dilute, aqueous aluminium nitrate was recorded. Static samples of solid ammonium chloride (Fig. 6.1(b)) and ammonium bromide both gave narrow spectra (~450Hz) which narrowed to ~100Hz on spinning (Fig. 6.1(a)) in a homebuilt "inverted"

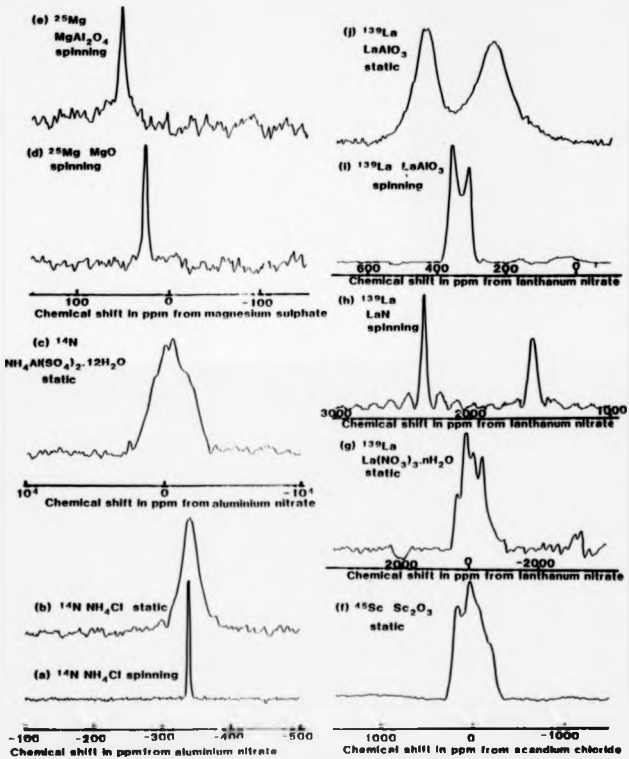

Figure6.1 Static and spinning spectra of ^{14}N(a)-(c),^{25}Mg(d),(e),^{45}Sc(f)and ^{139}La(g)-(j) from various compounds (c),(f)and(g) were accumulated using a quadrupole echo sequence. (Zero of chemical shift scale is dilute aqueous solution of the salt)

mushroom probe. A small chemical shift difference between NH_4Br(-334ppm) and NH_4Cl(-336.2ppm) was measured. In accumulating the spectra a number of drawbacks of the homebuilt probe were noted, in particular the small sample volume and the deadtime which was never better than 50μs. For NH_4Cl and NH_4Br with relatively narrow resonance lines these problems are comparatively unimportant but for the detection of very broad resonances they are severe handicaps.

As an intermediate step between the symmetric ammonium halides and the ceramics where distorted environments are expected, ammonium alum ($NH_4Al(SO_4)_2.12H_2O$) was examined. Single crystal measurements of ammonium alum have determined e^2qQ/h as 196kHz for ^{14}N(1). Attempts to obtain a direct static spectrum failed due to the deadtime (~20μs, Bruker static probe). To overcome this problem a quadrupole-echo sequence ((Sec. 3.5.1), with a 10μs π/2-pulse) was used. The lineshape obtained (Fig. 6.1(c)) does not have the form expected for a quadrupolar broadened spin-1 pattern, being narrower than for the efg determined by single crystal measurements. This is not an excitation problem as straight and composite pulse sequences gave similar results. The ^{27}Al MAS-NMR spectrum of the same sample gives a broader central component (~20ppm) than can be accounted for by residual second-order quadrupolar broadening, which should be less than 1ppm for e^2qQ/h ~440kHz(2), suggesting incomplete averaging is occurring. For ^{14}N in ammonium alum MAS at 3kHz would require an angular stability of only ±0.2° to cause narrowing into sidebands, if the residual sideband width is determined by angular considerations. If narrowing occurs the initial deadtime should not prevent detection of the later rotational echoes, even though the intense signal just after the pulse is lost, decreasing significantly the sensitivity. Any deadtime introduces the problem that any rotational echoes formed

produce spinning sidebands that are difficult to phase unless transformed from an echo peak. All attempts to produce narrowed spectra from ammonium alum, even an overnight experiment, produced no detectable resonance. This suggests that efficient narrowing of the resonance does not occur, even though internal angle-setting using ^{85}Rb in RbCl (Sec. 3.5.2) was employed.

This makes the observation of the ^{14}N resonance in the ceramics, where the quadrupole interaction strength could well be of the order of MHz unlikely. As the quadrupole interaction increases the required accuracy and stability of the angle to cause narrowing of these resonances also increases. Static NMR experiments employing quadrupolar echoes applied to AlN and BN gave no detectable signal. Even if narrowing occurs with e^2qQ/h ~MHz the signal will be smeared out over this frequency range, so with small sample volumes long accumulations would be necessary for detection. These results are relatively pessimistic for the likely usefulness of ^{14}N MAS-NMR in studying ceramics.

6.2 Magnesium-25

High resolution spectra of ^{25}Mg would clearly be helpful in constraining the cation distribution in spinels. It is a low frequency (~22MHz, B_o=8.45T), non-integer spin (I=5/2), quadrupole nucleus, so has ($\frac{1}{2} \leftrightarrow -\frac{1}{2}$) transition. The central transition will be ~8 times broader than ^{27}Al for the same efg making the resonance observable in a much more limited range of compounds. The ^{14}N homebuilt probe, with additional tuning capacitance was used. Probe operation was set up on a dilute aqueous solution of magnesium sulphate ($MgSO_4$) which is also used as the reference point for the chemical shift scale. MgO has a cubic NaCl-type structure and was initially run static. It gives a relatively narrow resonance

(FWHM~270Hz) which narrows on spinning (FWHM~100Hz, (Fig. 6.1(d)). It is shifted from the standard at (28±2)ppm. Stoichiometric mineral spinel gives a narrow MAS spectrum (FWHM ~150Hz) which peaks at (52±1)ppm (Fig. 6.1(e)). None of the non-stoichiometric spinels nor reagent grade $MgSO_4$ gave any observable resonance from MAS experiments but no echo sequence was attempted for magnesium.

The increased difficulty of observation of ^{25}Mg compared with ^{27}Al is illustrated by the spinel series. The ^{27}Al resonance from these spinels (Sec. 5.5) shows a slight decrease in intensity for the non-stoichiometric cases over $MgAl_2O_4$, indicative of an increase in the local distortion. It appears that the ^{25}Mg resonance in $MgAl_2O_4$ is on the limit of detection and increasing the local distortion makes it unobservable. In MgO magnesium is octahedrally coordinated (MgO_6) while in a normal spinel it is tetrahedrally coordinated (MgO_4). The single resonance from $MgAl_2O_4$ confirms that it is essentially normal with no sign of inversion. The positive shift of MgO_4 relative to MgO_6 follows the decrease in the electrostatic bond strength with increasing coordination. The expected trend of a decrease in chemical shift ranges of the elements across a row of the Periodic Table towards the alkali metals occurs. This is exemplified by the relative chemical shifts between tetrahedral units and octahedral units which decreases ^{29}Si(~100ppm) → ^{27}Al(~50ppm) → ^{25}Mg (~24ppm). Magnesium-25 NMR will be useful for determining the magnesium coordination in a similar way to ^{27}Al, especially when higher magnetic fields and spinning speeds are employed.

6.3 Scandium-45

High resolution NMR may provide information about the scandium coordination in these materials. It is a spin-$\frac{7}{2}$ nucleus and the high

spin factor (5/588) (Table 2.2) should aid observation of the central transition in materials with quite large efg's. A quadrupole echo sequence on Sc_2O_3 with a 50μs pulse delay (τ) gives a resonance which has a recognisable quadrupolar form (Fig. 6.1(f)). On rotation a complex manifold of narrow sidebands (FWHM~1.5kHz) is obtained which is difficult to phase. A possible isotropic shift is tentatively assigned at 12ppm. Broad resonances are obtained from the scandium silicate specimens with no quadrupole structure obvious. The multiphase nature of the silicate specimens result in the spectra being made up of overlapping scandium resonances from the different phases.

The Sc_2O_3 spectrum indicates the quadrupole interaction (e^2qQ/h) is larger than 12MHz and the presence of a shoulder corresponds to $\eta>0$. A subsequent powder study obtained e^2qQ/h ~(15±1)MHz with η~0.6±0.2 by simulating the static spectrum[3]. There is reasonable agreement with the chemical shift quoted in that work (0±200)ppm, considering the relative uncertainty in the measurements. No useful high resolution spectra were obtained from these samples.

6.4 Lanthanum-139

In view of the broad ^{45}Sc resonances the lower resonance frequency of ^{139}La will make its observation more difficult unless it occurs in a symmetric environment. Previous solid-state experiments on ^{139}La were performed on static samples in an applied magnetic field of 2.1T with only LaB_6 giving an observable resonance and no observable signal from $LaCl_3$, $La(NO_3)_3$ and La_2O_3.[4]

The system was set-up using a dilute aqueous solution of lanthanum nitrate which also provides the zero of the chemical shift scale. La_2O_3 contains lanthanum in a distorted seven-coordinate environment[5] and a quadrupolar-echo sequence produced a very short

echo (a few μs) which corresponds to a very broad spectral line and no distinct resonance was observed. Only single-phase sintered specimens were run in the spectrometer to reduce confusion from overlapping lines. Materials were chosen with lanthanum bonded to one species only since mixed coordinations (i.e. oxygen and nitrogen) are expected to give very broad resonances. Lanthanum β-alumina gives a very short lived echo which can be explained by a large efg at the lanthanum site, which agrees with lanthanum being twelve-coordinated by oxygen with two distinct La-O bondlengths[6]. Lanthanum nitrate also gives a broad resonance (Fig. 6.1(g)) but with a distinct quadrupole lineshape with the chemical shift ~0ppm. A static experiment using an echo sequence on LaN produces 2 relatively narrow resonances (FWHM~5kHz) with large shifts from the reference at ~1520ppm and ~2360ppm. These large shifts were initially treated sceptically but they appear to behave as expected when spectrometer conditions are changed (i.e. offset frequency) and they are absent from other lanthanum spectra. On spinning both resonances narrowed (FWHM ~1.5kHz for 2360ppm peak) with spinning sidebands apparent (Fig. 6.1(h)). $LaAlO_3$ gives a distinct quadrupole lineshape from a static spectrum, with no need to employ an echo sequence (Fig. 6.1(j)). On spinning a narrowed quadrupole lineshape was obtained. (Fig. 6.1(i)).

The ^{139}La resonance from $La(NO_3)_3nH_2O$ has shoulders at high and low frequency corresponding to a high asymmetry parameter with $\eta \sim 0.8$ from a spectral simulation. A similar powder study by Thompson and Oldfield[3] obtained a value for the shift of (-100±100) and for the quadrupole interaction (e^2qQ/h ~21.5±0.1MHz, η=0.85±0.05) from $La(NO_3)_3\ 6H_2O$. From figure 6.1(h) the efg is estimated to be of the order of 16MHz, but comparison between studies is difficult because different states of hydration can change the efg. LaN has a cubic NaCl-type structure so a narrow resonance is not unexpected but the

source of the two resonances remains unexplained at the moment. It should be remembered LaN reacts readily with moisture in the atmosphere to probably form La_2O_3 and/or $La(OH)_3$. Although the shift is very large it is in the correct sense for the reduction in lanthanum's coordination number to 6 in LaN from the twelve in $LaAlO_3$ and the shift range for heavy elements can be large. The isotropic shift of (375±5)ppm from $LaAlO_3$ corresponds to an LaO_{12} unit. The near cubic crystal structure is reflected in the local symmetry with a small efg at the aluminium site (Sec. 5.4) and even the lanthanum site has a manageable efg (e^2qQ/h ~6MHz). The lack of any shoulders and the narrowing factor (static → spinning) ~3.7 suggest $\eta \sim 0$. These first high resolution ^{139}La NMR spectra from the solid state do give some useful information about the local environment but only in a limited number of cases.

References. Chapter 6

1. Bailey, W.C. and Storey, H.S., J. Chem. Phys. 60, 1974, 1952-1953.
2. Zax, D.B., Bielecki, A., Pines, A. and Sinton, S.W., Nature 312, 1984, 351-352.
3. Thompson, A.R. and Oldfield, E., J. Chem. Soc. Chem. Commun. 1987, 27-28.
4. Lutz, O. and Oehler, H., J. Magn. Reson. 37, 1980, 261-267.
5. Wells, A.F., "Structural Inorganic Chemistry" (Fourth Edition) Clarendon Press, 1975.
6. Iyi, N., Inoue, Z., Takekawa, S. and Kimura, A., J. Sol. St. Chem. 54, 1984, 70-77.

CHAPTER 7. GENERAL CONCLUSIONS

7.1 The Application of MAS-NMR to Materials Science

As yet calculation of the chemical shift of a nucleus in a particular bonding arrangement is not possible, so deduction of the local environment of a nucleus based on the isotropic chemical shift can only be done by comparison with resonances from materials whose structure is known. The ^{29}Si NMR spectra from the complete range of tetrahedra SiO_xN_{4-x} ($0 \leq x \leq 4$) collected here show the expected trend to more paramagnetic shifts as the nitrogen level is increased, reflecting the increasing covalency of the bonds. However, the many influences on the isotropic chemical shift have been shown to cause an extensive overlap of the shift ranges from different units. In particular the negative shift of ^{29}Si in the lanthanum silicon oxynitrides compared with the yttrium analogues, making unambiguous interpretation based purely on the isotropic chemical shift difficult. The ability to distinguish structural differences appears quite variable, as in some materials small differences in the average bond length about silicon can be detected (e.g. α-Si_3N_4,δ-$Y_2Si_2O_7$) whereas in other materials different Q-types (e.g. $Y_2Si_3O_3N_4$) or even distinct nearest neighbour tetrahedra (e.g. $La_5Si_3O_{12}N$) cannot be clearly resolved. The very long spin-lattice relaxation times for ^{29}Si in some materials does not prevent the isotropic chemical shift being obtained, although quantitative data on the relative amounts of each phase present is usually lost. The principle of a scheme for collecting fully-relaxed spectra from such specimens and improving spectrometer efficiency has been demonstrated, which could become a routine operation.

The chemical shift ranges for ^{27}Al in the different environments AlO_6, AlO_4 and AlN_4 have now been more extensively investigated. For tetrahedral units the AlO_4 peak positions occur between 50ppm and 85ppm while AlN_4 units have peak positions between 100ppm and 115ppm. The ability to clearly distinguish these units is helped by the absence from high resolution ^{27}Al spectra of mixed nearest neighbour units (i.e. AlO_xN_{4-x},x=1,2,3) from all samples where they were expected to be present. This is one manifestation of the quadrupolar interaction at the ^{27}Al nucleus causing a loss of signal intensity from the NMR spectrum. In cases where the quadrupolar interaction is large extensive broadening results, so that the spectrum is incompletely excited making the resonance difficult to detect. The quadrupolar interaction makes quantitative interpretation of ^{27}Al spectra doubtful and some check on the relative fraction of the aluminium content of the sample represented by the spectra should be made. It is probable that all ^{27}Al solid-state spectra have "missing" signal intensity to some extent and uncertainty about the absolute level of aluminium represented by these spectra still remains.

The other nuclei investigated in this study do have some limited potential in the characterisation of ceramics. ^{14}N appears to be the least useful simply because the extensive first-order quadrupolar broadening of the ($1 \leftrightarrow 0$, $0 \leftrightarrow -1$) transitions in these materials. The useful structural information is probably present in the size of the quadrupole coupling constant if it can be obtained, rather than any high resolution chemical shift information. ^{25}Mg would appear to be more useful with MgO_6 and MgO_4 units having distinguishable chemical shifts from the limited data collected here. ^{45}Sc and ^{139}La also appear to be of limited applicability as the quadrupole interaction of ^{45}Sc and ^{139}La is exacerbated by their larger coordination numbers (cf ^{27}Al) making larger efg's more likely

and increased Sternheimer antishielding effects (especially for lanthanum). Obtaining useful chemical shift information from these nuclei, for an extensive range of materials at the present magnetic field is unlikely.

By compilation of a catalogue of isotropic chemical shifts and linewidths from phases allows the identification of phases in complex mixtures by simply matching the resonances. This "finger-printing" is a similar technique to XRD, that is a particular pattern corresponds to a particular phase. The use of MAS-NMR to aid phase characterisation has been demonstrated by the phase development in a number of ceramic systems (e.g. ^{29}Si for $Y_2Si_3O_3N_4$ and ^{27}Al for the yttrium aluminates) with some phases being more readily observed by MAS-NMR than XRD. For the yttrium aluminates very low levels of secondary phases could be identified by MAS-NMR that were absent from XRD. In addition to phase identification the NMR spectra can provide a more quantitative measure of the phase distribution once relaxation (e.g. ^{29}Si) and excitation (e.g. ^{27}Al) problems have been removed.

Another major advantage of MAS-NMR is its ability to probe the local structure of materials made up of elements of similar scattering factors. The ^{29}Si and ^{27}Al resonances from β'-sialon showed that strict partitioning of Si-N and Al-O bonds occurred. This allowed a layered structural model for β'-sialon to be formulated. NMR has to be combined with a technique such as XRD which can provide the overall, long-range crystal structure, which the resonance position alone is unable to give. Undoubtedly high resolution NMR will become increasingly used as a probe of materials to complement existing techniques. As MAS-NMR can monitor structural changes, particularly in amorphous materials applications to this field will expand.

7.2 Suggestions for Further NMR Studies of Ceramics

The limited range of materials consisting only of SiN_4 units studied here, has already demonstrated the extensive variation of the ^{29}Si chemical shift. In the materials of this study the Si-N bond lengths where known show only a limited range of values, close to the 0.174nm in β-Si_3N_4. A number of other nitrides exist (eg. $BeSiN_2$, Be_7SiN_6,Ca_4SiN_4) with the Si-N bond lengths having an extended range of values up to 0.187nm in $MgSiN_2$. An MAS-NMR investigation of the isotropic chemical shifts from these materials would aid understanding of how sensitive the chemical shift in SiN_4 tetrahedra is to connectivity, cation-type and bond length variations, in addition to the effect of the change of nitrogen hybridisation from sp^2 to sp^3. A number of alternative M-Si-Al-O-N systems exist which have phases made-up of $(Si,Al)(O,N)_4$ tetrahedra, with some phases having the same structure as the oxynitride phases studied here, while others have different crystal structures which would further extend the range of connectivities of $Si(O,N)_4$ units. For magnesium and calcium sialons a number of novel compounds exist with largely undefined crystal structures (e.g. $Ca_2Si_3O_5N_2$, $CaSi_2O_2N_2$) which MAS-NMR could make a contribution towards solving. Lutetium (which is diamagnetic) silicon oxynitrides could also be studied to gain a better understanding of cation effects on the ^{29}Si resonance.

To more completely define the structures in this study other nuclei could be examined. For the existing materials ^{89}Y could be investigated, with the spin-$\frac{1}{2}$ nucleus expected to produce relatively narrow lines, although long relaxation times may be a problem. A wide variety of yttrium coordinations exist with the coordination number varying from 6 to 12 in combination with both oxygen and nitrogen nearest neighbours. Magnesium MAS-NMR could provide useful

information about the magnesium coordination once a more thorough investigation of the chemical shift ranges of MgO_4 and MgO_6 units has been completed. However, probably the most fascinating study would be of ^{15}N and ^{17}O in enriched samples of the base compounds and the sialons. It could be that in these materials (e.g. the β'-sialon solid solution) the most structurally significant changes occur at the nitrogen and oxygen sites, with the silicon and aluminium being relatively insensitive to them. The ^{17}O and ^{15}N shift differences expected from different Si, Al coordinations of oxygen and nitrogen would clearly help to confirm the structural models proposed here. The effect on the chemical shift of nitrogen in nitride materials of changing its hybridisation from sp^3 (eg. $MgSiN_2$, $LiSi_2N_3$) to sp^2(eg. Si_3N_4,β'-sialon) has not been investigated. Also in phases such as $LaSi_3N_5$ it is of interest to examine the chemical shift difference between N(3Si) and N(2Si,2La) which should be similar to the hybridisation effect. This would obviously aid building structural models for the Y-Si-N phases.

For quadrupolar nuclei (especially ^{27}Al) the actual isotropic shifts and more importantly the quantitative interpretation of spectra should be further investigated. It would be extremely informative to repeat parts of this study, particularly on the yttrium aluminates, $Y_4Si_2O_7N_2$ and β'-sialon at much higher magnetic fields, for example 11.7T or 14T. Coupling these much higher fields with fast spinning (~20kHz) would make high resolution NMR of quadrupolar nuclei more attractive, since with pulse techniques at the present magnetic field quantitative information of the spectra from quadrupolar nuclei remains uncertain. The understanding of intensity problems encountered with extremely broad lines may be aided by performing some continuous wave experiments, where excitation problems are largely removed. The two-dimensional quadrupole nutation technique (Sec. 2.4)

is becoming increasingly used and it appears to offer an attractive option for the investigation of the quadrupole interaction of a nucleus without the need to extract the lineshape or perform experiments at several different magnetic fields.

As the catalogue of known chemical shifts is expanded and the range of nuclei routinely observed in the solid-state is increased the applicability of MAS-NMR will be enhanced. Once a more complete understanding of the information content of MAS-NMR spectra and its relationship to structure is gained MAS-NMR will become a standard technique in the investigation of the solid-state.

Appendix A. Angular Functions for Theoretical Expressions

The angular functions for the time-dependent part of the laboratory Hamiltonian [Eq 2.12], with the Euler angles (ϕ,θ,ψ) bringing the rotor axes into coincidence with the PAS of a particular crystallite are

$$C_1 = \tfrac{1}{2}\sin 2\beta\,\sin\theta[\cos\theta(\eta\cos 2\psi - 3)\cos\phi - \eta\sin 2\psi\sin\phi] \qquad [A.1]$$

$$S_1 = \tfrac{1}{2}\sin 2\beta\,\sin\theta[\cos\theta(3 - \eta\cos 2\psi)\sin\phi - \eta\sin 2\psi\cos\phi] \qquad [A.2]$$

$$C_2 = \tfrac{1}{2}\sin^2\beta\,\{[\tfrac{3}{2}\sin^2\theta + \tfrac{\eta}{2}(\cos 2\psi(1+\cos^2\theta)]\cos 2\phi - \eta\cos\theta\,\sin 2\psi\sin 2\phi\} \qquad [A.3]$$

$$S_2 = \tfrac{1}{2}\sin^2\beta(-[\tfrac{1}{2}\sin^2\theta + \tfrac{\eta}{2}(\cos 2\psi\,(1+\cos^2\theta)]\sin 2\phi - \eta\,\cos\theta\sin 2\psi\,\cos 2\phi\} \qquad [A.4]$$

(After Maricq, M. and Waugh, J.S., J. Chem. Phys. 70, 1979, 3300-3316).

The angular functions for the second-order quadrupolar perturbed frequency ν_m of the $(m\leftrightarrow -1)$ transition [Eq 2.21], for a sample under MAS-averaging, where ϕ and θ are the polar angles which rotate the rotor axes into the PAS of a particular crystallite are

$$B = \frac{1}{4}(3\sin^2\theta + \eta(1+\cos^2\theta)\cos 2\phi] \qquad [A.5]$$

$$C = \frac{1}{2}\eta\cos\theta\sin 2\phi \qquad [A.6]$$

$$D = \frac{1}{4}\sin 2\theta(3 - \eta\cos 2\phi) \qquad [A.7]$$

$$F = \frac{1}{2}\eta\sin\theta\sin 2\phi \qquad [A.8]$$

(After Kundla, E., Samoson, A., and Lippmaa, E., Chem. Phys. Lett. 83, 1981, 229-232).

TITLE A HIGH RESOLUTION MULTINUCLEAR MAGNETIC RESONANCE STUDY OF CERAMIC PHASES

AUTHOR Mark Edmund Smith

INSTITUTION and DATE University of Warwick for 1987